ABSTRACT

DEPARTMENT OF CHEMISTRY

GUNASINGHE, ROSI N.

B.SC. RAJARATA UNIVERSITY, 2004

M.SC. UNIVERSITY OF PERADENIYA, 2007

M.S. CLARK ATLANTA UNIVERSITY, 2012

ELECTRONIC AND MAGNETIC PROPERTIES OF CARBON-BASED AND BORON-BASED NANO MATERIALS

Committee Chair: Xiao-Qian Wang, Ph.D.

Dissertation dated May 2017

The structural and electronic properties of covalently and non-covalently functionalized graphene are investigated by means of first-principles density-functional-theory. The electronic characteristics of non-covalently functionalized graphene by a planar covalent organic framework (COF) are investigated. The aromatic central molecule of the COF acts as an electron donor while the linker of the COF acts as an electron acceptor. The concerted interaction of donor acceptor promotes the formation of planar COF networks on graphene. The distinctive electronic properties of covalently functionalized fluorinated epitaxial graphene are attributed to the polar covalent C–F bond. The partial ionic character of the C–F bond results in the hyperconjugation of C–F σ-bonds with an sp^2 network of graphene. The implications of resonant-orbital-induced

doping for the electronic and magnetic properties of fluorinated epitaxial graphene are discussed.

Isolation of single-walled carbon nanotubes (SWNTs) with specific chirality and diameters is critical. Water-soluble poly [(m- phenyleneethynylene)- alt- (p-phenyleneethynylene)], 3, is found to exhibit high selectivity in dispersing SWNT (6,5). The polymer's ability to sort out SWNT (6,5) appears to be related to the carbon–carbon triple bond, whose free rotation allows a unique assembly. We have also demonstrated the important role of dispersion forces on the structural and electronic stability of parallel displaced and Y-shaped benzene dimer conformations. Long-range dispersive forces play a significant role in determining the relative stability of benzene dimer. The effective dispersion of SWNT depends on the helical pitch length associated with the conformations of linkages as well as π-π stacking configurations.

We have revisited the constructing schemes for a large family of stable hollow boron fullerenes with 80 + 8n (n = 0,2,3,...) atoms. In contrast to the hollow pentagon boron fullerenes the stable structures constitute 12 filled pentagons and 12 additional hollow hexagons. Based on results from density-functional calculations, an empirical rule for filled pentagons is proposed along with a revised electron counting scheme. We have also studied the relative stability of various boron fullerene structures and structural and electronic properties of B_{80} bucky ball and boron nanotubes. Our results reveal that the energy order of fullerenes strongly depends on the exchange-correlation functional employed in the calculation. A systematic study elucidates the importance of incorporating dispersion forces to account for the intricate interplay of two and three centered bonding in boron nanostructures.

ELECTRONIC AND MAGNETIC PROPERTIES OF CARBON-BASED AND BORON-BASED NANO MATERIALS

A DISSERTATION

SUBMITTED TO THE FACULTY OF CLARK ATLANTA UNIVERSITY

IN PARTIAL FULFILLMENT OF THE REQUIREMENTS FOR

THE DEGREE OF DOCTOR OF PHILOSOPHY

BY

ROSI GUNASINGHE

DEPARTMENT OF CHEMISTRY

ATLANTA, GEORGIA

MAY 2017

ACKNOWLEDGEMENTS

The work presented here would not have been possible without the support and guidance of several people. A sincere thank you goes to my parents, my daughter, my soul mate and my family for their tireless belief in me. I would like to express my appreciation to my advisor, Dr. Xiao-Qian Wang, for his invaluable guidance, direction and supervision throughout the tenure of my study. I also acknowledge the support given by the faculty and staff of the Clark Atlanta University Department of Chemistry and Physics. Last but not least, I wish to thank all my colleagues whose assistance, perception and advice influenced production and made the office an interesting place to work.

TABLE OF CONTENTS

CHAPTER

CHAPTER

LIST OF FIGURES

Figure

Figure

Figure

Figure

LIST OF TABLES

Table

LIST OF ABBREVIATIONS

BLYP	Becke-Lee-Yang-Parr
B3LYP	Becke-3-Lee-Yang-Parr
BSSE	Basis set superposition error
CBM	Conduction Band Minimum
CCSD(T)	Coupled-Cluster Computations with Perturbative Triples
CNTs	Carbon Nanotubes
COF	Covalent Organic Framework
DFT	Density Functional Theory
DN	Double Numerical
DNP	Double Numerical Plus Polarization
DOS	Density of State
FEG	Fluorinated Epitaxial Graphene
GGA	Generalized Gradient Approximation
HHTP-PBBA	hexahydroxytriphenylene-1,4- henylenebis(boronic acid)
HOMO	Highest Occupied Molecular Orbital
LUMO	Lowest Unoccupied Molecular Orbital
MD	Molecular Dynamics
m PE p PE	Poly[(m- phenyleneethynylene)- alt- (p- phenyleneethynylene)]
MP2	Second Order Moller Plesset

MWNT	Multi-Walled Carbon Nanotube
NiPc- PBBA	Ni phthalocyanine-1,4- henylenebis(boronic acid)
PBE	Perdew-Burke-Ernzerhof
PD	Parallel Displaced
PmPV	poly[(m-phenylenevinylene)-alt-(p-phenylenevinylene)]
RPA	Random Phase Approximation
SLG	Single-Layer Graphene
SWNTs	Single Walled Carbon Nanotubes
TNP	Triple Numerical Polarized
TS	Tkatchenko−Scheffler
VBM	Valence Band Minimum
vdW	van der Waals
XC	Exchange-Correlation

CHAPTER 1

INTRODUCTION

1.0 Graphene

Graphene is a single layer of carbon arranged in a hexagonal lattice [1-5] is being explored as a viable candidate for next-generation nanoscale electronics, optoelectronics, sensors, hydrogen storage, and photonics.[1–5] The quantum Hall effect and extremely high electron mobility at room temperature are some of the unique characteristics of graphene. These unique characteristics make graphene a candidate for use in many different potential applications, including transistors, integrated circuits, and biosensors.[4] The high carrier mobility suggests that this material may be a viable successor for copper interconnects in electronic device structures. To realize these technologies, it is necessary to understand and to control its extraordinary properties.[1−5]

1.1 Functionalized Graphene

The functionalization of graphene is a convenient method for enhancing graphene's solubility and processability.[6–9] The tailoring of graphene's structural and electrical properties is crucial for developing graphene-based electronic and photonic nanotechnologies. Varieties of methods have been developed to covalently[10–15] and noncovalently functionalize graphene. For example, the high carrier mobility of graphene

can be tuned and regulated by the covalent attachment of aryl groups by diazonium[16] or azide reactions.[17,18] On the other hand, graphene has been noncovalently functionalized using phthalocyanine[19–24] and pyrene[25] derivatives. These planar π-conjugated organic compounds have the capability to self-organize on graphene surfaces forming supramolecular systems via π–π interactions. Electron transfer upon photoexitation can effectively modify the electronic and photonic properties of graphene.[23]

1.1.1 Non-Covalently Functionalized Graphene

Recently, the noncovalent attachment of a covalent organic framework (COF) on single-layer graphene (SLG) has been reported.[26,27] COFs are typically three-dimensional structures made up of covalently linked planar rigid organic subunits.[28] The long-range ordered structures of COFs with high thermal stability lead to potential applications including gas separation, storage, and catalysis applications.[29–34] Typically, COFs are insoluble powders from solvothermal reactions and can be grown on metal surfaces by sublimation of the associated planar units. The π-conjugated subunits of COFs possess suitable affinity with SLG and can be processed for ordered attachment.

1.1.2 Covalently Functionalized Graphene

Hydrogenated or fluorinated graphene are quasi two-dimensional lattices of carbon atoms ordered into a buckled honeycomb sub-lattice, in which each carbon atom is chemically bonded to either hydrogen or fluorine. For two-sided chemisorption, the adsorption pattern prefers a chair-like arrangement.[14,35,36]

The chemisorption of hydrogen and fluorine atoms results in modification of the chemical bonds of the underlying honeycomb lattice.[37,38] The ensuing sp^3 hybridization transforms the sp^2 C-C partial double bonds into single bonds by the formation of additional single C-H or C-F bonds, respectively. The transformation changes locally the planar shape of graphene into an out-of-plane, nanoscale buckled geometry.[39] Experimentally, it has been shown that the hydrogenated graphene, referred to as graphane, can be synthesized from a pristine epitaxial graphene layer in the presence of atomic hydrogen.[15] Similarly, functionalizing single layer graphene by fluorination leads to transition from metallic to semiconducting owing to the induced changes in hybridization as well.[15,40] Experimental results also demonstrate the possibility of tuning the electronic transport properties of graphene mono-layers and multi-layers by functionalization with fluorine.[41] The fully fluorinated graphene, referred to as fluorographene, is the building block of various novel materials and has increasingly opened up ample possibilities in two-dimensional electronic applications.[42,43]

Grown on a SiC substrate, fluorinated epitaxial graphene (FEG) exhibits coherent transport properties that hold potential for novel carbon-based nanoelectronic intensively,[9] a comprehensive study of the interplay between covalent and semi-ionic C-F bonds remains elusive. applications.[44,45] While the two-sided fluorination of graphene has been investigated intensively,[9] a comprehensive study of the interplay between covalent and semi-ionic C-F bonds remains elusive.

1.2 Carbon Nanotubes

In 1991, the existence of carbon nanotubes was proposed by Iijima [46] who first imaged multi-walled carbon nanotube (MWNT).[46] Two years later, Ijima and his coworker observed single walled carbon nanotubes (SWNTs). Since then, the unique structure and property of carbon nanotubes have attracted researchers around the world. At that time, it was called "carbon fiber" which was based on its chemical component. After several decades' research, with the excellent property and wide application, carbon nanotubes proved to be more than a fiber. Chemical structure of a carbon nanotube has some similarity to its allotropes: diamond, graphene and fullerene. The difference of these carbon materials relies on the hybridized structure of carbon atom. In the diamond structure, the carbon atom is sp^3-hybridized and each carbon is bonded to four other carbon atoms, forming a crystalline structure.[47] Due to this tetrahedral crystalline structure, diamond exhibits a great hardness and heat stability. For the structure of graphite, the carbon atoms are all sp^2-hybridized on a planar sheet, resulting a huge hexagonal network. In this structure, each carbon atom is connected with three other carbon atoms. The electron can move freely on the delocalized π bond network, similar to graphite, the carbon atoms on carbon nanotube are also sp^2-hybridized. The morphology of carbon nanotube can be viewed as a rolling graphite sheet (Figure1.1), capped with fullerene hemisphere. With a large aspect ratio (ratio of length to diameter) carbon nanotube is a perfect nano-wire in nano scale.

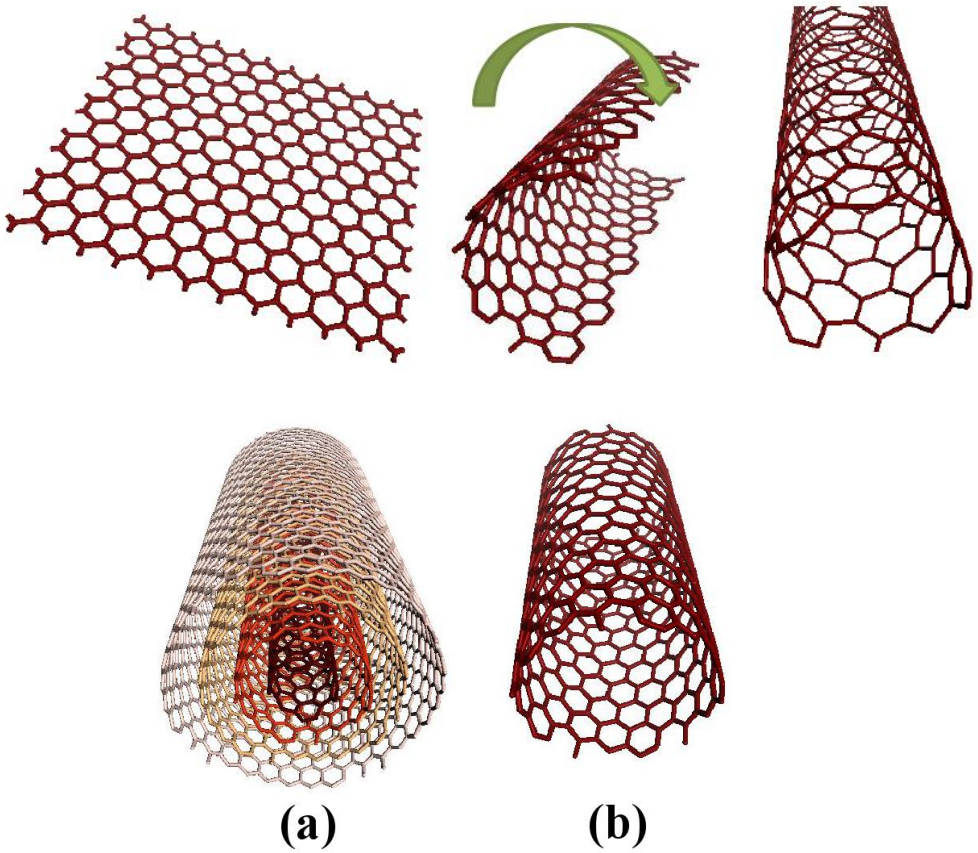

Figure 1.1. Graphene rolled to form carbon nanotubes. (a) multi-walled carbon nanotube, (b) single walled carbon nanotube.

If the tube is formed by rolling up from a single layer of graphene, this tube is called single walled carbon nanotube (SWNT). If the tube is formed by rolling up from multiple layers of graphene, this tube is called multi-walled carbon nanotube (MWNT) (Figure 1.1). Single walled carbon nanotube (SWNT) has a small diameter around 1.0-1.5 nm. Although the length of multi-walled carbon nanotube is similar to that of single walled carbon nanotube, multi-walled carbon nanotube has a much larger diameter, for

example, for a 30 coaxial tubes, the diameter of inner and outer tube is 5 and 100 nm, respectively.

1.2.1 Classification of Single Walled Carbon Nanotubes

Single-walled carbon nanotubes (SWNTs) are among the most promising new materials in the focus of nanoscience and nanotechnology, as they exhibit superior mechanical[48] and electrical properties. [49, 50] Because the structure of single walled carbon nanotube (SWNT) originates from a single graphene layer, each SWNT can be labeled according to the rolling vector of graphene lattice. The robust physical properties of individual SWNT are uniquely dependent on the chiral indices (n, m) which determine the tube's diameters. [51]

1.3 Boron Nano Materials

Since the discovery of C_{60} buckyball about twenty-five years ago, the fascinating properties and promising applications of the synthetic carbon allotropes fullerenes, nanotubes, and graphene overwhelmingly illustrate their unique scientific and technological importance.[52,1] As boron and carbon share abundance of bonding similarities, [53-60] there has been a tremendous amount of interest in the search for nanostructured counterparts of carbon allotropes. Among the efforts to exploit hollow inorganic cage-like structures, the theoretical prediction of a highly stable "magic" B_{80} buckyball found by Szwacki, Sadrzadeh, and Yakobson [53] has received a great deal of attention. [11-20] The boron buckyball B_{80} is structurally analogous to the eminent $C_{60,}$ [1]

with 60 boron atoms placed at the corners of a truncated icosahedron that constitutes 12 pentagons and 20 hexagons, along with extra 20 boron atoms in the center of each hexagon.[53] The 20 capping atoms stabilize the cage of the identical icosahedral (I_h) symmetry as in the C_{60} buckyball.

The novel chemical bonding pattern of B_{80} provides crucial insights into the nature of boron nanomaterials and has prompted considerable efforts in designing associated nanostructures such as endohedral complexes, [59] solids [60,61] and hydrogen storage media. [62] Inspired by the B_{80} buckyball configuration, construction rules for a family of stable boron fullerenes were proposed.[63] Moreover, careful examination of the chemical bonding of the B_{80} buckyball with triangular and hexagonal motifs led to reevaluation of boron sheets and nanotubes composed of purely puckered triangular structures, revealing a more stable α-boron sheet (α-BS).[55]

Although boron fullerenes have not yet been observed experimentally, the I_h-B_{80} buckyball is, nevertheless, a prototype structure for boron nanomaterials owing to the pattern of capping atoms and the peculiar charge transfer. The electronic properties of the I_h-B_{80} buckyball closely resemble those of C_{60} in that each has a total of 240 electrons, and the lowest unoccupied molecular orbital (LUMO) is triply degenerate.[54] Notwithstanding these fascinating properties, the exact location of the capping atoms is a subject of debate. The exact location of the capping atom in the center of the empty hexagon has been investigated by various approaches. While various density-functional theory (DFT) calculations evoked a slightly puckered cage with tetrahedral (T_h) symmetry [58] due to the requirement of the vibrational stability, recent studies using the

dispersion-corrected DFT [64] as well as the computationally intensive *ab*-initio calculations up to MP2 theory [65] reasserted the vibrational stability of the I_h–B_{80} buckyball. The migration between the B_6 (filled-pentagon) and B_7 (filled-hexagon) units can lead to lower energy conformations than for the I_h–B_{80}.[64,66,67] The migration of the capping atom from the center of a hexagon to the center of a pentagon yields a rearrangement of the charge transfer associated with the capping atoms; thereby tailoring the aromaticity or anti-aromaticity of the cage. [64,66-69] Furthermore, the inclusion of a B_{12} cluster into a B_{68} cage leads to improved energy for a core-shell structured B_{80}. [68,69]

The thesis is organized as follows. In Chapter 2, we discuss filled and empty orbital interactions in a planar covalent organic framework on graphene. In Chapter 3, we discuss resonant orbitals in fluorinated epitaxial graphene. In Chapter 4, we discuss highly selective dispersion of carbon nanotubes by using poly (phenyleneethynylene)-guided supermolecular assembly. In Chapter 5 we discuss impact of π-π interaction mode polymer conformations and vinylene bond geometry on helical wrapping of carbon nanotubes. In Chapter 6, we discuss filled pentagons and electron counting rule for boron fullerenes. In Chapter 7, we study the dispersion-correction in the boron buckyball and nanotubes and in Chapter 8 is discussed the relative stability of boron fullerenes using a dispersion-corrected density functional approach.

CHAPTER 2

FILLED AND EMPTY ORBITAL INTERACTIONS IN A PLANAR COVALENT ORGANIC FRAMEWORK ON GRAPHENE

2.0 Introduction

Experimental work shows that [2,3,6,7,10,11] hexahydroxytriphenylene-1,4-henylenebis(boronic acid) (HHTP-PBBA) and Ni phthalocyanine-1,4-henylenebis(boronic acid) (NiPc- PBBA) grown on epitaxial graphene [30] lead to planar self-assembly of hexagonal and square lattices, respectively. The solution-phase-derived hybrids were found to be nonsoluble in general solvents. The integrated π-conjugated components in the supramolecular structures are appropriate for optoelectronic devices. The phthalocyanine and phenylene-derived COFs are macrocyclic compounds that are optically and electrically active. Phthalocyanine can form metal coordination complexes with nickel, which exhibits an intense blue-green color. Ni phthalocyanine hromospheres are active within the visible range. These hybrid materials have potentially improved spectral resolution and thus are promising candidates for organic photovoltaic devices.[70,71] The modular construction and hierarchical assembly of π-conjugated COFs are amendable to rational incorporation into graphene-based nanomaterials.

Experimental advances in the supramolecular self-assembly of covalent organic frame works (COFs) on graphene have motivated our study of the associated charge transfer at the interface between COF and graphene. Herein, we present a dispersion-corrected density functional theory (DFT) investigation of the structural and electronic properties of COF-functionalized single layer graphene (SLGs). Our results reveal that there is a substantial level hybridization in the supramolecular nanostructure. Graphene mediates a complementary donor-acceptor complex of the center molecule and linker. The hybridization-induced charge delocalization of electron-donating and -accepting components upholds a planar pattern of the COF on graphene.

2.1 Method

We have employed first-principles calculations based on dispersion-corrected DFT to describe interactions between the aromatic COF and graphene. Perdew−Burke−Ernzerhof (PBE) parametrization of exchange correlation was used with a double numerical (DN) basis set as implemented in DMol3.[72] The general gradient approximation (GGA) results were subsequently rectified through the inclusion of a dispersion correction effect. Tkatchenko−Scheffler (TS) dispersion correction accounts for the relative variation in dispersion coefficients of differently bonded atoms by weighting values taken from the high-quality ab initio database with atomic volumes derived from partitioning the self-consistent electronic density. The TS scheme exploits the relationship between polarizability and volume. The optimization of the atomic position was performed with convergent forces of less than 0.01 eV/Å. The change in the

energy was less than 3×10^{-4} eV per unit cell. While the empirical corrected functional meets difficulties in describing the noncovalent interaction between aromatic rings and metals,[73,74] the TS dispersion-corrected functional has been shown to be essential in correctly accounting for the van der Waals interactions between aromatic systems.[75−77] It is known that the GGA functional underestimates the gap between the HOMO and LUMO for molecules.[75] However, we are primarily concerned about the binding behavior of the COF on graphene. The dispersion corrected GGA provides an accurate description in this aspect.[75,76]

2.2 Results and Discussion

We considered two COFs on graphene; one is a boronate ester-linked COF referred to as HHTP-PBBA, and the other is NiPc-PBBA. As shown in Figure 2.1a and Figure 2.1b, the COFs are composed of central molecules, HHTP or NiPc, along with the linker molecule PBBA. To model the HHTP-PBBA and NiPc-PBBA COFs on graphene, we examined binding energies of the combined structures. A careful analysis indicated that 13×13 rhombus and 14×14 square graphene unit cells are the optimal commensurate unit cells for HHTP-PBBA and NiPc-PBBA, respectively. The HHTP central molecule has three functional sites to which the PBBA linker molecule can attach. The linker-attached HHTP forms a hexagonal-shaped network on graphene (see Figure 2.1a). The interlayer distance between the SLG sheet and HHTP-PBBA COF is 3.08 Å. The length of one side of the hexagonal-shaped COF is 15.93 Å. As seen in Figure 2.1a, the central ring of the HHTP molecule pursues A−B stacking with respect to the

underlying graphene layer, whereas the three terminal bridging HHTP rings follow A−A stacking. The PBBA bridging rings shows parallel-displaced stacking relative to the underlying graphene. In contrast to HHTP, NiPc has four functional sites in which the PBBA linker molecule can attach.

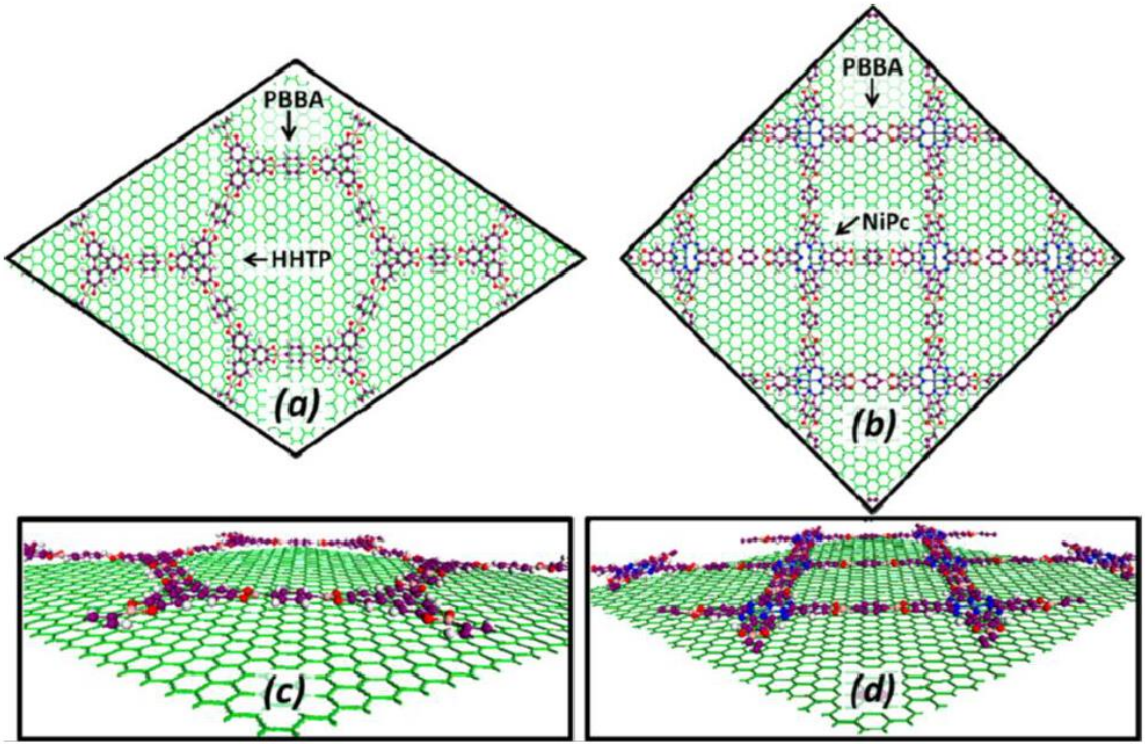

Figure 2.1. Optimized ball-and-stick models of (a) HHTP-PBBA and (b) NiPc-PBBA planar COFs on graphene. Carbon atoms on graphene and on COFs are colored with green and purple, respectively. Hydrogen, oxygen, nitrogen, nickel, and boron atoms are colored in white, red, blue, light blue, and pink, respectively.

The resultant planar COF is of a square shape (see Figure 2.1b). The layer distance between SLG and the NiPc-PBBA COF is 3.24 Å. The length of one side of the

square lattice is 14.32 Å. As seen in Figure 2.1b, the NiPc-PBBA bridging hexagonal rings shows an A−A stacking configuration, while the interior ring shows parallel-displaced stacking relative to the underlying graphene.

We show in the Figure 2.2 the calculated band structure of HHTP and HHTP-COF on graphene in the left and right panels, respectively. As is typical to noncovalent functionalized graphene, there are two types of bands. One type of band refers to flat bands associated with HHTP or PBBA, and the other types of bands are dispersive ones that originated from graphene. In the absence of graphene, electrons in the HOMO and LUMO levels are localized. However, the interaction with graphene yields profound level hybridizations between the dispersed bands and the flat bands, which result in delocalization of the corresponding HOMO- and LUMO derived bands. As seen from Figure 2.2, the linear dispersion characteristic π and π^* bands of graphene are near the K point. The HOMO- and LUMO-derived bands of the HHTP-PBBA COF are located at −1.44 and 1.44 eV, respectively. As seen from the insets of Figure 2.2, the charge density of the HOMO accumulates on the triphenylene molecule in the HHTP-PBBA, while the charge of the LUMO amasses on the PBBA linker.

It is worth noting that in the absence of the PBBA linker, the HOMO-derived band of HTTP is closer to the Fermi level, while the LUMO-derived band is located far above the Fermi level. The latter implies that the HTTP serves as a charge donor to graphene. However, the inclusion of the PBBA linker leads to a donor-acceptor complex, which is mediated by the graphene layer.

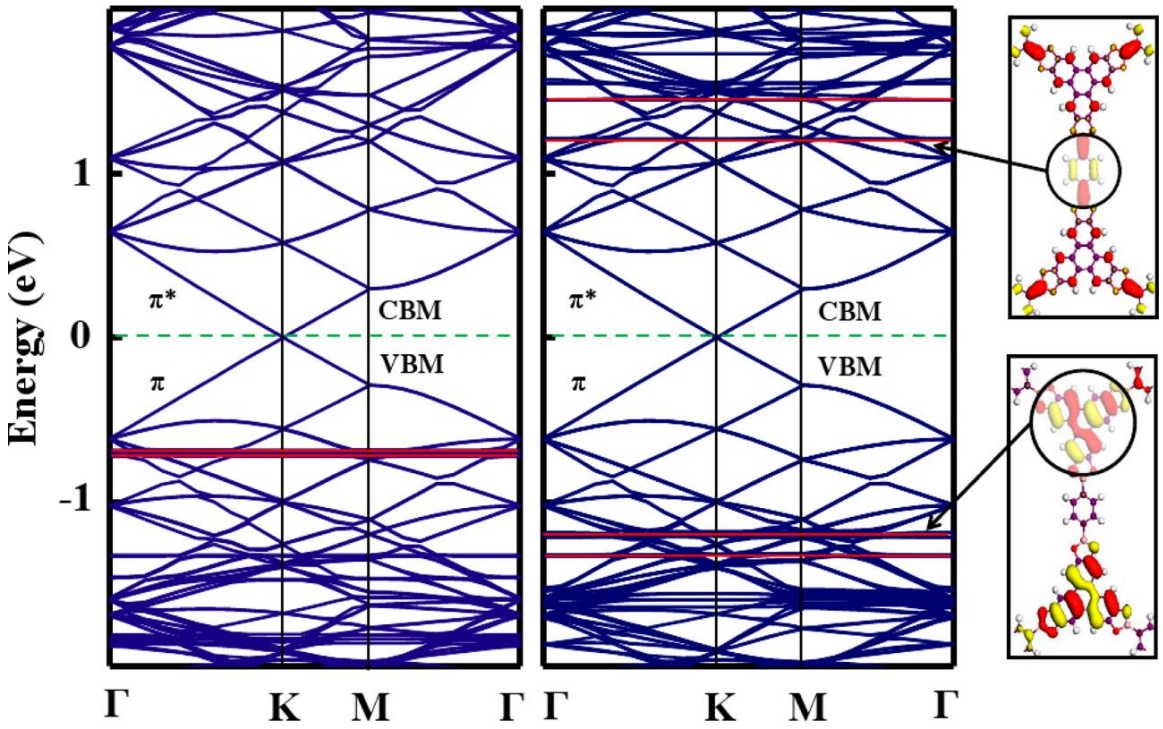

Figure 2.2. Calculated band structures of HHTP and HHTP-PBBA on graphene in the left and right panels, respectively. The HOMO- and LUMO derived bands of HHTP are highlighted in red. (Inset) Extracted charge densities of the HOMO and LUMO of HHTP-PBBA with an isovalue of 0.025 au.

To better understand the level hybridization between the COF and graphene components, we depict in Figure 2.3 the charge density plots of near-gap states for HHTP-PBBA and NiPc-PBBA. HHTP-PBBA and NiPc-PBBA. As seen in Figure 2.3a, the level hybridization manifests itself through the modifications to the uniformly distributed charges of pristine graphene or localized charges on molecule components. Specifically, the unoccupied and occupied states show an attraction and repulsion of the charge density to the HHTP-PBBA COF, respectively. The attraction and repulsion of the local charge density are attributed to the filled and empty orbital interactions.

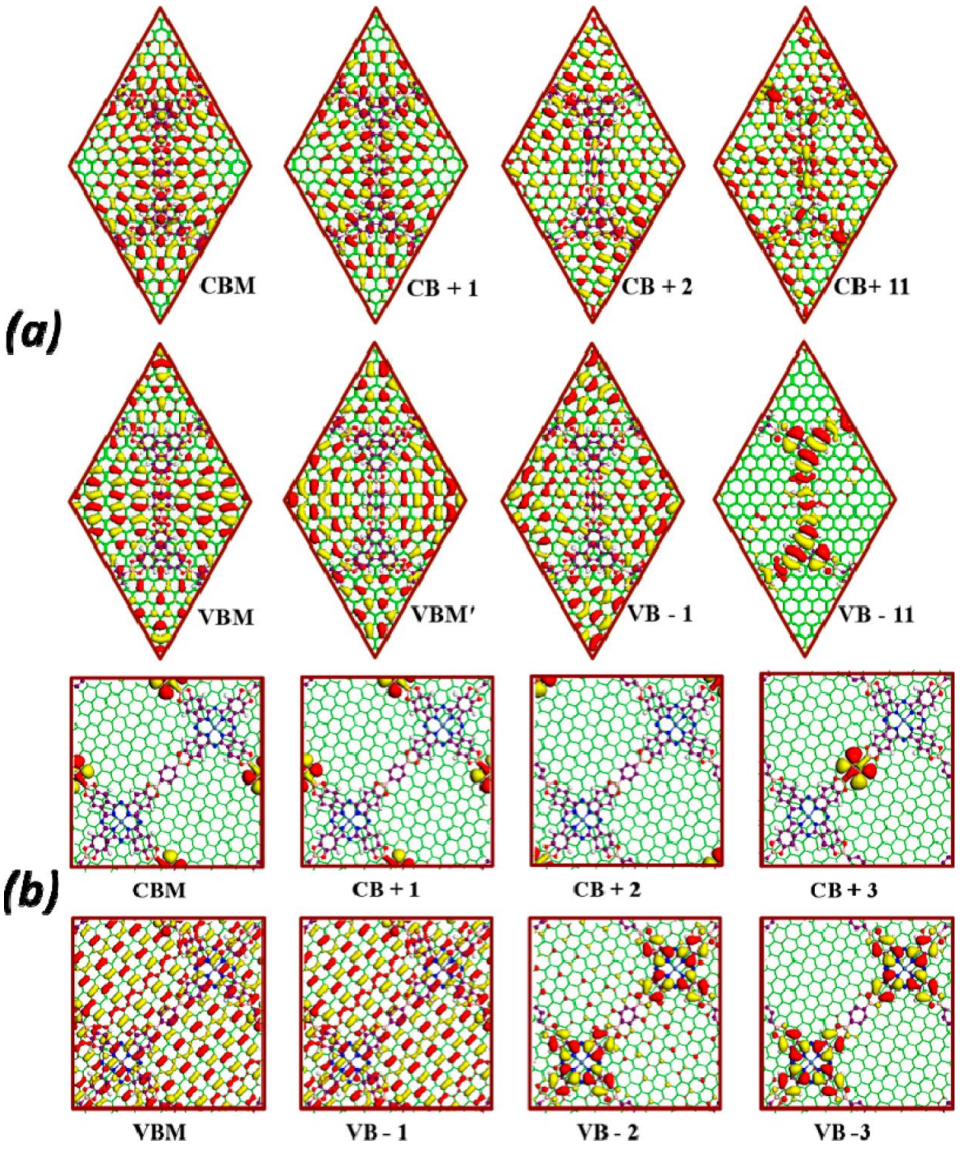

Figure 2.3. Extracted charge densities of the near-gap states of HHTP-PBBA on graphene at the band center. The isovalue is 0.025 au.

Interestingly, for the patterned HHTP-PBBA COF, the HOMO- and LUMO derived bands are far away from the Fermi level, which are located 11 levels below and valence band minimum (VBM) and 11 levels above the conduction band minimum (CBM), respectively. It is worth noting that for isolated HHTP on graphene, a pair of

HHTPs resumes energetically favored patterns with the inter-HHTP distances, in agreement with the HHTP-PBBA hexagonal patterns. This implies that for the formation of the hexagonal HHTP-PBBA pattern, the PBBA linkers favor connecting the preordered HHTPs. The energy extracted for the HHTP-PBBA on graphene is 29.28 eV lower than that for the HHTP on graphene counterpart. As a result, the interactions between the filled orbital and empty orbital play an important role in forming the planar COF. These results strongly suggest that the graphene layer delocalizes electrons in the HOMO- and LUMO-derived bands of HHTP-PBBA. A synergistic interaction between the filled and empty orbitals manifests itself through concerted interaction between the HHTP aromatic central molecule and the PBBA linker. The enhanced orbital interactions between the filled and empty bands give rise to a planar COF network on graphene. These finding are corroborated by binding energy studies. Subsequently, the single-layer planar COF network on graphene allows for the ensuing vertical stacking of linkers and central molecules, leading to highly ordered layered supramolecular architectures.

We show in Figure 2.3b the extracted charge densities for NiPc-PBBA COF. As is readily observable in Figure 2.3b, the uniformly distributed valence states (VBM and VB-1) are primarily characteristic of graphene. For the occupied states, HOMO-derived bands can be identified as VB-2 and VB-3 because the charges for those states are mainly confined at the NiPc components. Analogous to HHTP-PBBA, the NiPc-PBBA also leads to strong binding of 10.67 eV with the PBBA linker. In contrast, for the unoccupied states, the charges are confined primarily on the PBBA components of the COF.

Therefore, the formation of the square-shaped NiPc-PBBA planar conformation is attributed to the filled and empty orbital interactions as well.

In summary, we have studied the electronic characteristics of HHTP-PBBA and NiPc-PBBA on graphene. The noncovalent attachment of these COFs preserves the sp^2 hybridization network of graphene. The planar COF networks self-assemble on graphene via the graphene-mediated complementary orbital interactions between the filled orbital of the center molecule and the empty orbital of the linker. The hybridization-induced charge delocalization of the charge donor and acceptor COF components results in a stable COF−graphene hybrid.

CHAPTER 3

RESONANT ORBITALS IN FLUORINATED EPITAXIAL GRAPHENE

3.0 Introduction

To facilitate a fundamental understanding of fluorinated epitaxial graphene (FEG), herein we investigate FEG using first-principles density functional calculations. In the absence of fluorination, two pristine graphene sheets interact with each other with weak van der Waals forces.[40,78] However, unsaturated C sites in the fluorinated graphene sheet are reactive due to unpaired electrons. As a result, a graphene sheet can bind to fluorinated graphene sheet as semi-fluorinated bilayer epitaxial graphene (EG). We consider various conformations through a bilayer graphene with one-sided adsorption, which serves as a prototype for the fluorination on EG. Among possible conformations of the fluorinated graphene bilayer, we examine the relative stability of both bonded and non-bonded configurations. To this end, we have employed dispersion-corrected first-principles density functional calculations.[72] Previous results have shown that the maximal number of sp^2 carbon atoms increases the stability of the corresponding structure.[11,79] Our present results demonstrate that the orbital resonance arising from the hyperconjugation of the carbon sp^2 orbital with the C–F σ* orbital is attributed to the further stability of the stirrup conformation of FEG. There are two energetically favored prototype conformations of 1,2-difluoroethane (H_2FCCFH_2). One is the gauche-conformation, in

which the fluorine atoms are staggered next to each other; the other is the anti-conformation, in which the fluorine atoms are staggered on the opposite side to each other. The gauche interaction results in the overlap between two atoms whose dihedral angle is more than 01 (i.e., eclipsed), but less than 1201 (i.e., staggered). The gauche interaction obstructs the bond rotations and stabilizes the gauche-conformer. This phenomenon is referred to as the gauche effect.[80]

3.1 Method

The structural and electronic properties were investigated using first-principles density functional calculations. Our first-principles calculations are based on spin polarized dispersion corrected density functional theory with general gradient approximation (GGA) for exchange–correlation potential.[81] We employed the dispersion correction with the GGA using the Tkatchenko–Scheffler (TS) scheme, which exploits the relationship between polarizability and volume.[82] The TS dispersion correction accounts for the relative variation in dispersion coefficients of differently bonded atoms by weighing values taken from the high-quality first principles database with atomic volumes derived from partitioning the self-consistent electronic density.[82]

A kinetic energy change of 3×10^{-4} eV in the orbital basis and appropriate Monkhorst–Pack k-point grids of $6 \times 6 \times 1$ were sufficient to converge with the integration of the charge density.[72] The optimization of the atomic positions proceeds until the change in energy is less than 1×10^{-5} eV per cell. A supercell with a vacuum space of 16 Å normal to the graphene plane was used. The incorporation of the dispersion

correction is considered to be important for accurately describing the interlayer van der Waals interactions. The employed scheme has been tested for various non-covalent functionalized graphene systems.

The quasiparticle corrections to the DFT eigenvalues were evaluated using the G0W0 approximation. The electron self-energy, S, was calculated by summing up ring-polarization diagrams to the lowest order in the screened Coulomb interaction, through a product of the one-electron Green's function G0 and the dynamical screened Coulomb interaction W0. The DFT eigenvalues and eigenfunctions (using a 24 × 24 × 1 k-mesh and a 435 eV kinetic energy cut-off, along with a normconserving pseudo-potential of the Troullier–Martins type. We included 110 bands in the calculation. A 1.06 nm distance in the direction perpendicular to the fluorographene layer) were employed to evaluate the one-electron Green's function G0. The screened Coulomb interaction was calculated within the RPA and the self-energy was evaluated by the plasmon-pole approximation. Based on quasielectron and quasihole states, the absorption spectrum was calculated by solving the Bethe–Salpeter equation as implemented in the YAMBO package.[83] We used an efficient method to cut-off the long-range Coulomb interaction between the supercell replica in order to remove the Coulomb tail, along with a random integration method to improve the numerical stability.

3.2 Results and Discussion

Orbital resonance is the primary cause of the gauche effect in difluoroethane.[84,85] The donation of electrons from the carbon–hydrogen s bonding orbital to the carbon–fluorine σ* anti-bonding orbital is attributed to the stabilization of the gauche-isomer. Due to the difference in electronegativity, the C–H s orbital is a better electron donor than the C–F of fluorine counterpart. On the other hand, the C–F σ* orbital is a better electron acceptor than the C–H σ* orbital. The corresponding gauche-conformation promotes enhanced orbital overlap between the C–H s orbital (donor) and the C–F σ* orbital (acceptor). There is an increased p-orbital character of carbon–fluorine bonds due to the large electronegativity.

A gauche conformation forms a bent bond that partially compensates the orbital overlap. The periodic counterpart of the gauche-conformation stands for the so-called stirrup conformation. [9,79] In the stirrup conformation, fluorine adsorption is along the zigzag direction. Fluorine adsorption results in adjacent zigzag chains moving up and down in an alternative manner. We show in Figure 3.1 the optimized structures of one-sided FEG *rec*-stirrup, *twist*-boat, *rec*-chair, boat, stirrup, and chair conformations.[8,86–90] These patterns were identified to be the low energy configurations for hydrogenated EG in previous studies.[79] The *rec*-chair and variants of chair, stirrup, and boat conformations have bonding between graphene layers. By contrast, the *rec*-stirrup, *twist*-boat, and AA-stacked chair-II conformations have non-covalently bonded layers. The energy order of one-sided FEG conformations was examined.

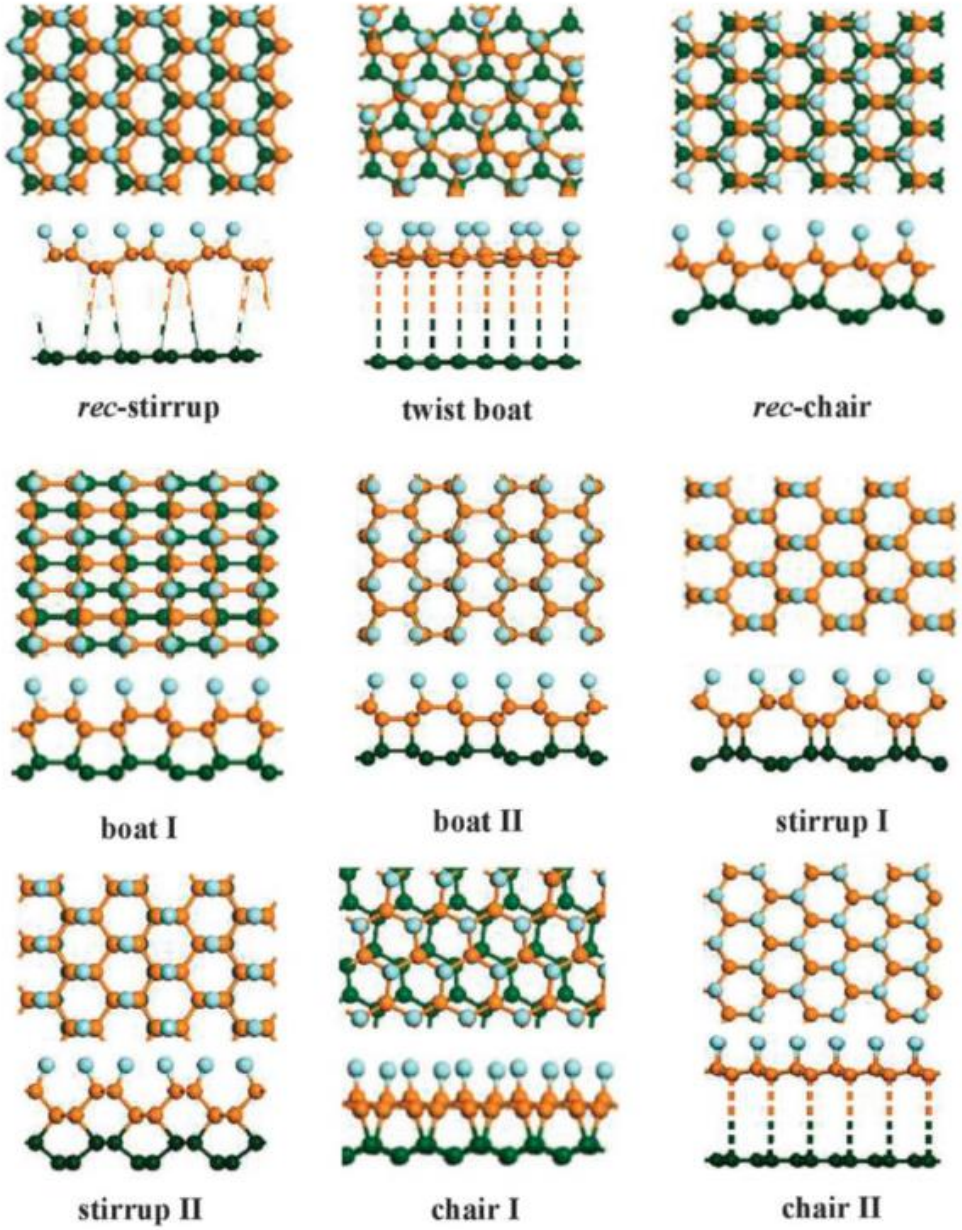

Figure 3.1. Optimized structures of semi-fluorinated bilayer graphene. Carbon and fluorine atoms are colored in orange (top layer), green (bottom layer), and blue, respectively.

Summarized in Table 3.1 are the calculated binding energy per atom (E_b) and the energy gap (E_g) for semi-FEG conformations. As seen from Table 3.1, *rec*-stirrup is

energetically favored over other structures. Among those structures in Table 3.1, *rec*-stirrup, *rec*-chair, stirrup I, and stirrup II conformations show metallic behavior without an energy gap, whereas the boat, *twist*-boat, chair I, and chair II conformations show semiconducting behavior.

Table 3.1. Calculated Binding Energy per Carbon Atom E_b, the Band Gap E_g, and the Cell Dimension a × b for Chair, Stirrup, Boat, and *Twist*-Boat Conformations and their Re-Constructed Counterparts of Semi-Fluorinated Bilayer Graphene

Structure	E_b (eV)	E_g (eV)	a × b (Å × Å)
Rec-stirrup	- 8.02	0	4.25 × 2.48
Twist boat	-7.98	0.013	4.98 × 4.37
Rec-chair	-7.96	0	4.33 × 2.53
Boat I	-7.94	2.011	4.29 × 2.53
Boat II	- 7.92	2.356	4.25 × 2.48
Stirrup I	- 7.90	0	4.27 × 2.53
Stirrup II	- 7.85	0	3.87 × 2.53
Chair I	- 7.83	2.521	4.36 × 2.52
Chair II	- 7.80	0	4.34 × 2.53

Among the 9 configurations considered, *rec*-stirrup, *twist*-boat, *rec*-chair, and boat-I undergo planar shifts relative to the underlying graphene layer. Stirrup-I, stirrup-II, and chair-II are of A-A stacking in that the C atoms in the semi-fluorinated graphene is

on top of the C atoms. Chair-I is the two-layer variant of fluorinated counterpart of previously proposed ferromagnetic conformation of graphene.[91]

The rec-stirrup and rec-chair have alternative sp^2 and sp^3 chain structures, which are preferable from the point of view of structural stability.[17] To describe the electronic structure characteristics of low-energy conformations, we show in Figure 3.2 the calculated band structures for *rec*-stirrup, *twist*-boat, *rec*-chair, and boat conformations of semi-FEG. While the contribution from top and bottom layers to the electronic band structure is clearly distinguishable, the band structure of semi-fluorinated *rec*-stirrup has distinct characteristics compared to that of semi-hydrogenated *rec*-stirrup.[79] To be specific, the crossing in the proximity of the Y–Γ direction is attributed to the graphene layer. On the other hand, the FEG displays a metallic behavior as a result of the π and π* bands overlap at A and Y, 0.6 eV below the Fermi level (highlighted by orange circles in Figure 3.2a). The lowering of the band crossing for FEG is in stark contrast to the hydrogenated EG, in which the crossing is at the Fermi level.

In analogy, the *rec*-chair has the p and π* bands overlap in the point A of the reciprocal space, exactly at the Fermi level. There is another crossing point for bands at Y, where the overlapped π and π* bands cross about 0.4 eV below the Fermi level. The dispersion along A–Y is attributed to contributions from alternative sp^2 and sp^3 chains since the edge point Y corresponds to the zig-zag chain direction in real space.

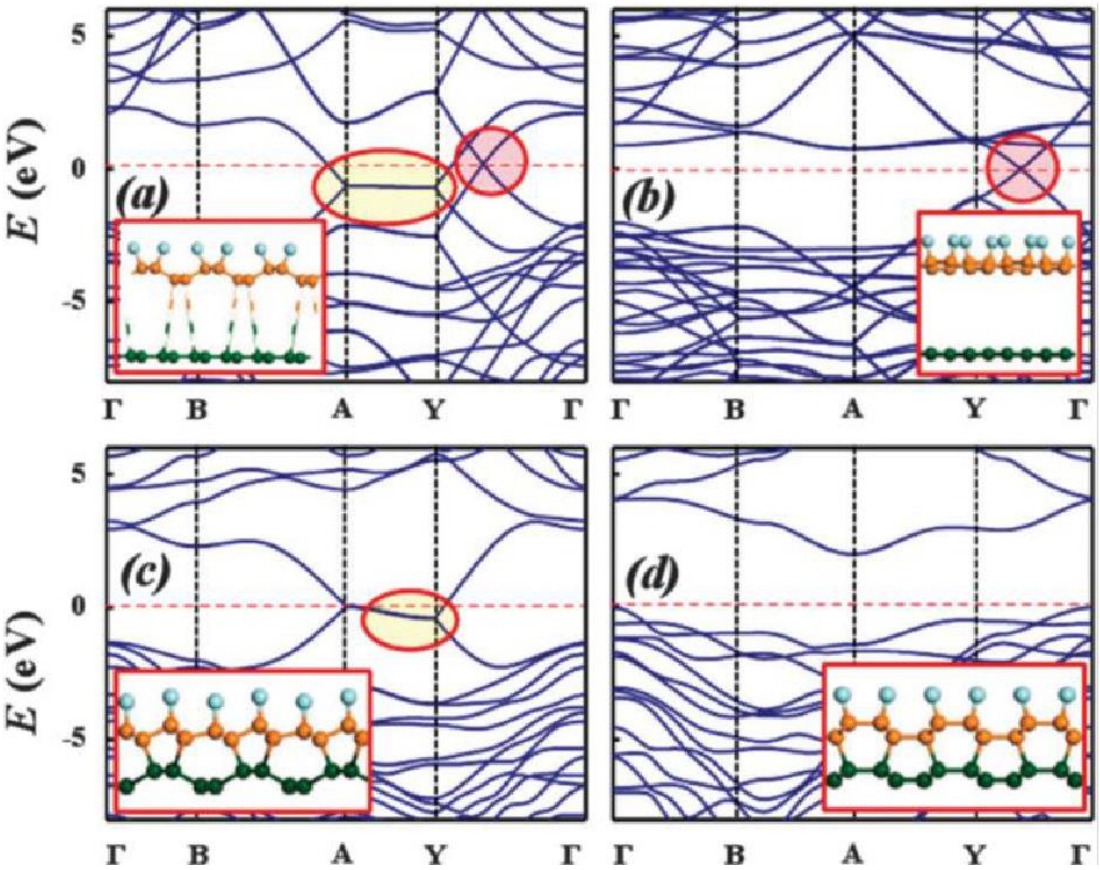

Figure 3.2. Calculated band structures of (a) *rec*-stirrup, (b) *twist*-boat, (c) *rec*-chair, and (d) boat conformations of semi-fluorinated bilayer graphene. For *rec*-stirrup Y = (0, p/2b), Γ = (0, 0), B = (_p/2a, 0),where a=4.25 Å, b=2.48 Å. For *twist*-boat Y = (0, p/2b_1), Γ = (0, 0), B = (p/2a_1, 0), where a_1 = 4.98 Å, b_1 = 4.37 Å. For *rec*-chair Y = (0, p/2b_2), Γ = (0, 0), B = (_p/2a_2, 0),where a_2 = 4.33 Å, b_2 = 2.53 Å. For boat Y = (0, p/2b_3), Γ = (0, 0), B = (_p/2a_3, 0), where a_3 = 4.29 Å, b_3 = 2.53 Å. The valence band maximum is set to be 0 eV.

For hydrogenated EG, the linear sp^2 chains are little disturbed by the nearly sp^3 chains in that semi-metallic behavior leads to crossing at the Fermi level at the Y point. In contrast, for FEG, the sp^2 and sp^3 chains undergo substantial overlap, leading to mutual doping along with the lowering of the crossing point.[11,79] The twist-boat and boat conformations of semi-fluorinated bilayer graphene have qualitatively similar band

structures compared to its hydrogenated counterparts. Similar characteristics in band structures are due to the absence of sp^2 chain configurations in those structures.

Orbital resonance stands for the overlap of σ-bonds with a p network. Hyperconjugation leads to an extended molecular orbital that increases the stability of the system.[92–94] The polar covalent C–F bond is the strongest single bond in organic chemistry. Confinement of the charge density around the fluorine leaves the carbon relatively electron poor, along with introducing ionic character into the bond through partial charges ($C^{\delta+}$–$F^{\delta-}$). Electron cloud is more likely to be on fluorine in the C–F bond in semi-fluorinated conformation. By contrast, the electron cloud of semi-hydrogenated conformation tends to be uniformly distributed around the C–H bond. In this regard, fluorinated *rec*-stirrup conformation with alternating sp^2 and sp^3 chains presents an interesting example of hyperconjugation in a periodic structure.

As shown in Figure 3.3, the hyperconjugation is reminiscent of p-orbitals of sp^2 chains interacting with the C–F σ* orbitals of sp^3 carbon chains. Hyperconjugation manifests the formation of a cross-linked path throughout the FEG. As seen in Figure 3.3, strong hybridization of carbon and fluorine orbitals leads to the cross-linked charge density distribution, which is in contrast to the charge confinement of sp^2 chains in hydrogenated EG. These interconnected charge densities delocalize the electrons and result in a metallic conformation.

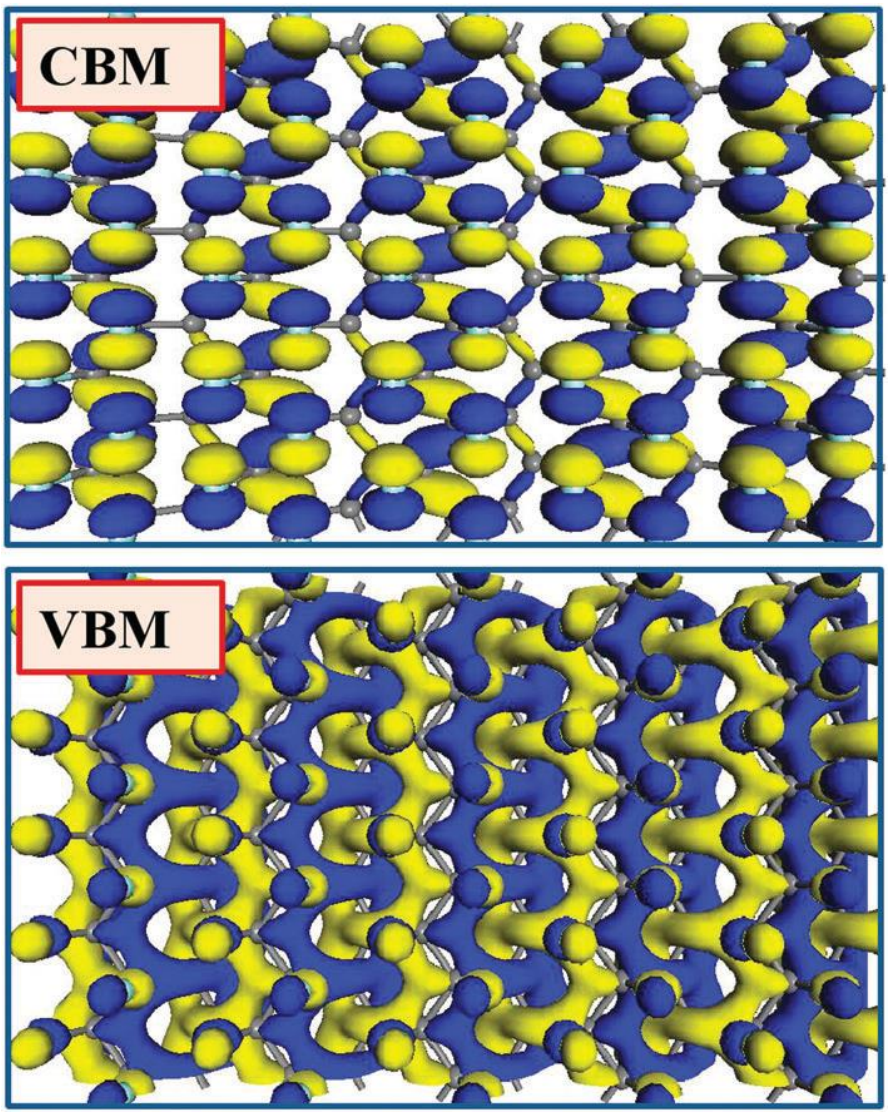

Figure 3.3. Extracted charge density for the stirrup conformation of semifluorinated bilayer graphene, for the conduction band minimum (CBM) and valence band maximum (VBM) in top and bottom panels, respectively. The isovalue of charge density is 0.05 a.u.

The overlap of charge density is attributed to doping from fluorine to carbon. Band lowering with respect to the Fermi level along A–Y is directly correlated with the hybridization of carbon and fluorine, which signifies in both rec-stirrup and *rec*-chair conformations. An interesting question concerns the magnetic properties of FEG. It is

worth noting that the chair conformation of FEG has an intrinsic ferromagnetic behavior. However, the conformation is energetically less favorable as compared to other conformations, notably the *rec*-stirrup, *twist*-boat, and *rec*-chair configurations.

The generalized gradient approximation (GGA) of the density functional theory (DFT) is known to fail in describing electron-hole (e-h) and electron-electron (e-e) interactions. These interactions are responsible for the formation of excitons and the quasiparticle excitations. In this regard, the GW-Bethe–Salpeter equation (GW-BSE) approach represents one of the state-of-the art theories beyond DFT.[83] While random phase approximation (RPA) can be equivalent to the results of the DFT level, GW-RPA Includes e-e interactions, and GW-BSE goes beyond RPA by including e-e and e-h interactions.

The low energy excitations are dormant in the calculated spectra (Figure 3.4). The first RPA peak is located at 3.8 eV, which is markedly higher than the 3.1 eV for the two-sided fluorographene counterpart. The next RPA peak is around 5.2 eV, which corresponds to the transition from the nearly valance band to the nearly flat conduction band, in the proximity of the band center. As seen from Figure 3.4, the e-e interactions lead to a substantial blue-shift. The first RPA peak at around 3.8 eV is shifted to 7.5 eV under GW-RPA. The inclusion of e-h interactions largely compensates the effect of e-e interactions. The onset value of the first major GW-BSE peak is around 3.8 eV. This result is in good conformity with the experimentally measured value of 3.8 eV.[9]

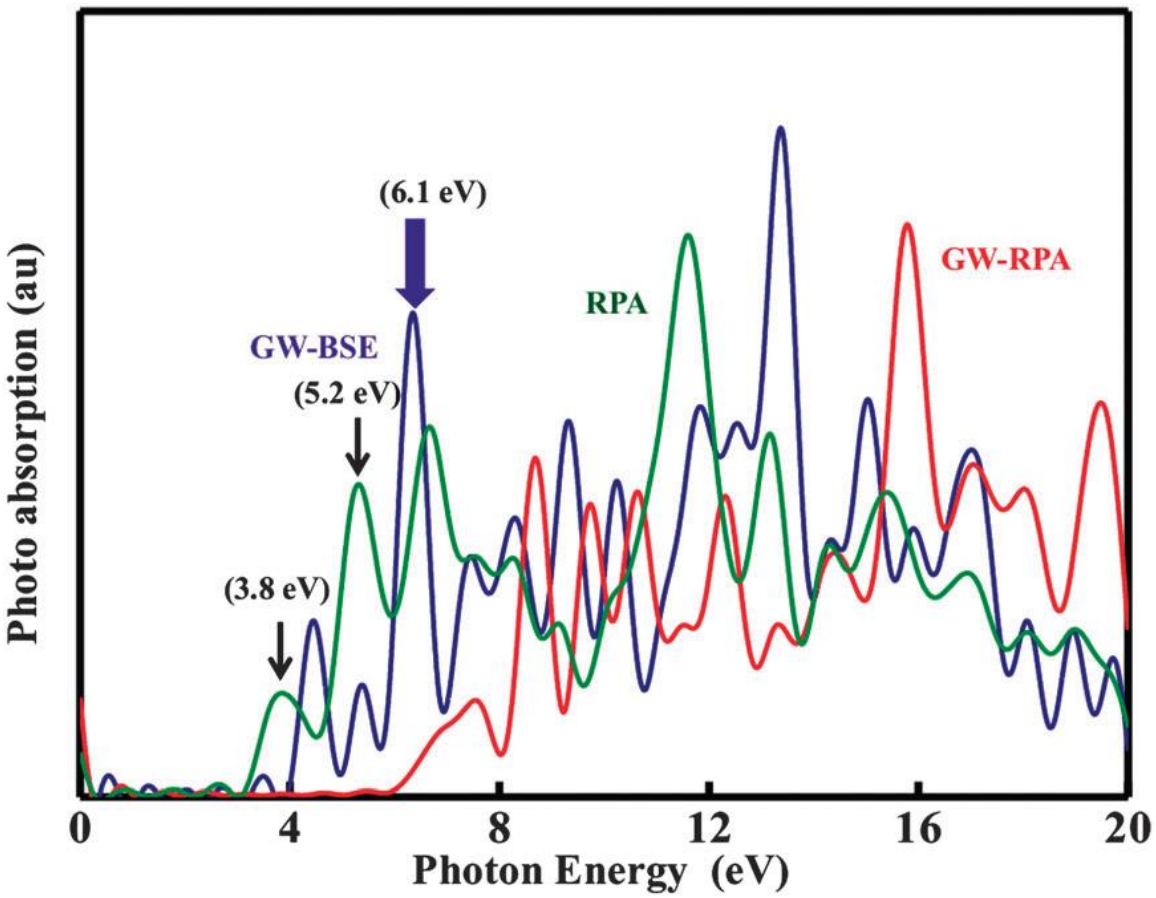

Figure 3.4. Calculated photo absorption spectra using RPA (green line), GW-RPA (red line), and GW-BSE (blue line) for semi-fluorinated epitaxial graphene.

It is noteworthy that the inclusion of e-e and e-h interactions leads to notable enhancement of the second excitation at around 6.1 eV. The enhancement of the peak is reminiscent of the enhanced excitonic excitations in the two-sided fluorographene.[9] For the other transitions, it is typically observable that GW-RPA provides blue-shifts of about 1–3 eV, while the GW-BSE compensates the blue-shift with a smaller red shift. As a result, the GW-BSE results are close to the RPA ones. However, the excitonic feature around 6.1 eV is much weaker in the RPA spectra, indicating that the incorporation of e-h interactions is pivotal to the description of the excitation effect. To explore the ordered

ferromagnetic networks, we constructed the trigonal patterns on FEG (Figure 3.5), which corresponds to the experimentally observed network structure in hydrogenated graphene.[11,79]

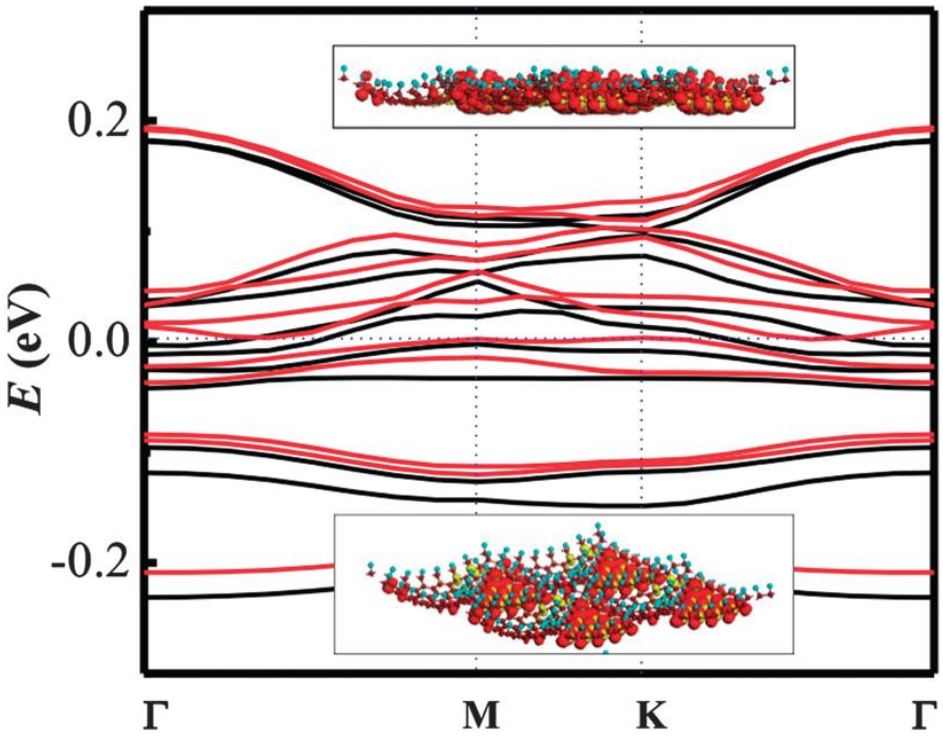

Figure 3.5. Calculated band structures for the trigonal conformation of semi-fluorinated graphene. Y = (0, p/2b), Γ = (0, 0), B = (_p/2a, 0), where a = 4.25 Å, b = 2.48 Å. For *twist*-boat Y = (0, p/2b_1), Γ = (0, 0), B = (p/2a_1, 0), where a_1 = 4.98 Å, b_1 = 4.37 Å. For *rec*-chair Y = (0, p/2b_2), Γ = (0, 0), B = (_p/2a_2, 0), where a_2 = 4.33 Å, b_2 = 2.53 Å. For boat Y = (0, p/2b_3), Γ = (0, 0), B = (_p/2a_3, 0), where a_3 = 4.29 Å, b_3 = 2.53 Å. The valence band maximum is set to 0 eV. Insets: side and perspective views of the spin density of the trigonal network.

The extracted band structure shows that the network preserves the ferromagnetic feature, owing to the breaking of AB symmetry. However, in contrast to the semiconducting behavior in the trigonal patterns of hydrogenated graphene, for FEG the corresponding network is metallic. Orbital resonance leads doping from the patterned

network to the neighboring sp^2 regions as well. As a result, the corresponding bands in hydrogenated EG shift downward, leading to the metallic behavior. An important ramification is that the magnetic states of FEG are more sensible to the adsorption patterns in connection with the orbital resonance. It is noteworthy that the spin density distribution has mixing of the spin components in contrast to the hydrogenated EG network.[79]

In summary, we have investigated the structural and electronic characteristics of semi-fluorinated graphene conformations. While the relative stability of various patterns follows the same energy order as the corresponding hydrogenated graphene counterparts, the partial ionic character of the C–F bond results in the orbital resonance of C–F s-bonds with an sp^2 network of graphene. Orbital resonance stabilizes the stirrup conformation via the gauche effect. Orbital resonance leads to additional delocalized electrons in the FEG. As a result, effective tailoring of electronic and ferromagnetic properties of FEG needs an improved understanding of the associated orbital resonance effect.

CHAPTER 4

HIGHLY SELECTIVE DISPERSION OF CARBON NANOTUBES BY USING POLY (PHENYLENEETHYNYLENE)-GUIDED SUPERMOLECULAR ASSEMBLY

4.0 Introduction

Unfortunately, single walled carbon nanotubes in the prepared sample are generally grown as a mixture of different SWNTs. In order to access SWNT of single (n,m) chirality, a post-synthesis process becomes necessary to separate different SWNTs. Individualization of a specific chiral SWNT from their mixture remains a major challenge, due to their structural similarity between SWNT species.[95]

SWNTs can be sorted on the basis of their diameters, where a sample of a narrow diameter range contains fewer (n, m) tubes. Thus far, the enrichment of small diameter nanotube, such as (6,5), can be achieved by using DNA, [96] densitygradient ultracentrifugation, [97,98] dextran-based size-exclusion gel, [99] and polymer.[100–102] While polymers can be used to enrich SWNTs on the basis of tubes' diameters [100 , 101] and electronic type, [100 , 103] the separation mechanism is unclear in most cases. Few studies have been reported in selective chirality sorting for (6,5) SWNT. Wei et al. described a multistep extraction to enrich (6,5) and (8,3) SWNTs using the surfactant of sodium dodecyl sulfate and sodium cholate. [104]

As we mentioned earlier, isolation of single-walled carbon nanotubes (SWNTs) with specific chirality and diameters is critical for achieving optimum performance of SWNTs in various applications. Recently a water-soluble π -conjugated polymer, poly[(m- phenyleneethynylene)- alt- (p- phenyleneethynylene)] (m PE p PE), 3 , as shown in Figure 4.1 is experimentally found to exhibit high selectivity in dispersing SWNT (6,5).

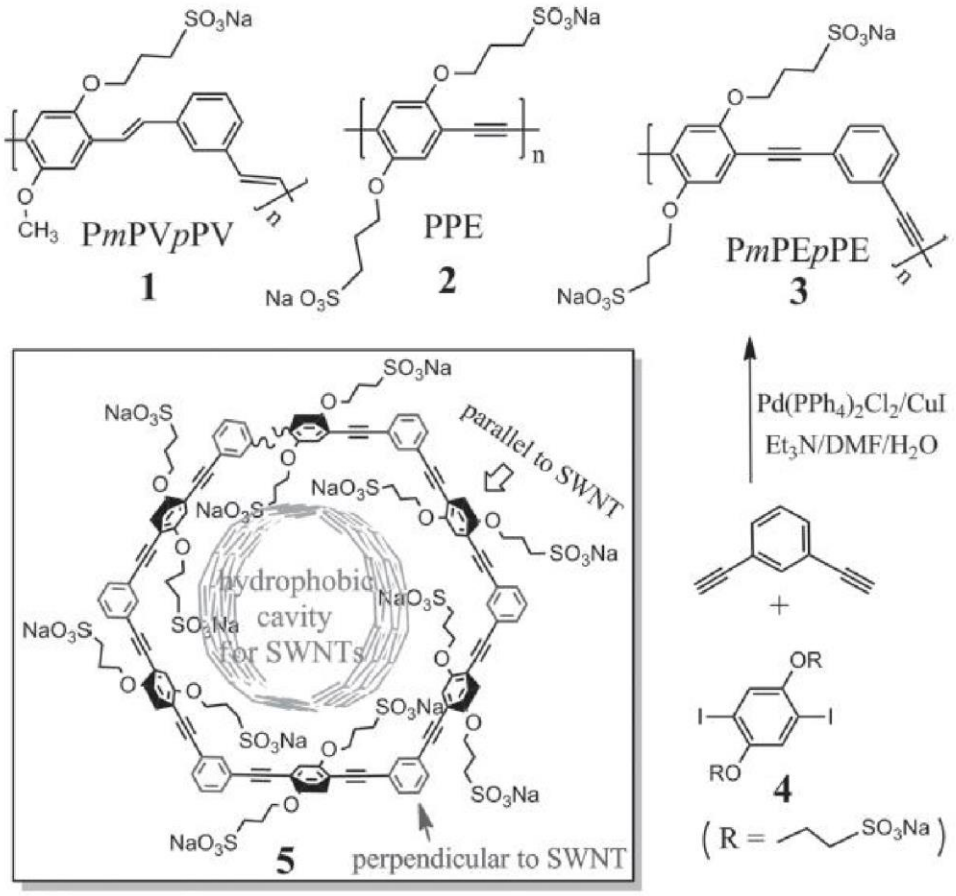

Figure 4.1. Polymer structures of, poly[(mphenylenevinylene)-alt-(p-phenylenevinylene)] (P m PV p PV) 1 and poly(p- phenyleneethylene) (PPE) 2 , and synthesis of polymer poly[(m- phenyleneethynylene)-alt-(p- phenyleneethynylene)] (P m PE p PE) 3 . The inset illustrates the helical wrapping of 3 on an SWNT.[105]

The polymer's ability to sort out SWNT (6,5) as shown in the Figure 4.2,[105] 2D photoluminescence (PL) map of SWNTs, appears to be related to the carbon-carbon triple bond, whose free rotation allows a unique assembly of chromophores in a helical conformation.

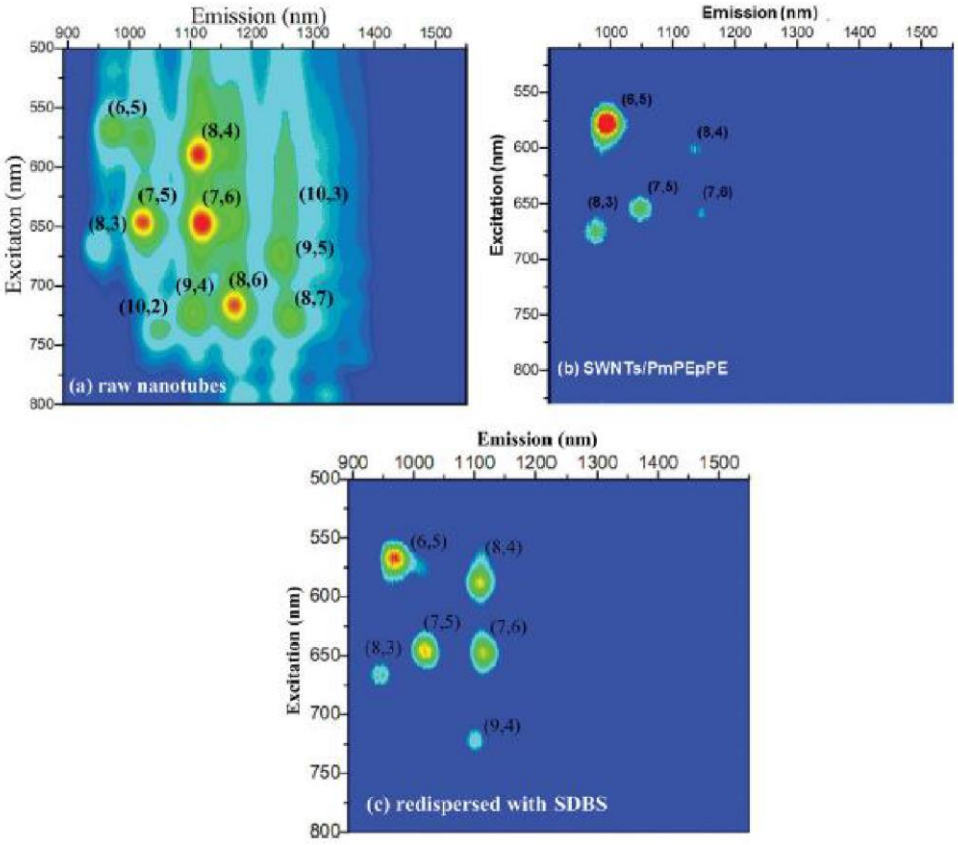

Figure 4.2. 2D photoluminescence (PL) map of SWNTs, where each SWNT is indicated by its chiral indices (n,m). (a) Raw SWNTs were dispersed with sodium dodecylbenzenesulfonate (SDBS) surfactant in D_2O. (b) SWNTs were dispersed by using P m PE p PE in D_2O. Chiral indices (n,m) of each SWNTs are shown. (c) the P m PE p PE-dispersed sample was redispersed with SDBS to replace the polymer.[105]

The intriguing selectivity of polymer 3 to SWNT (6,5), however, is not observed for the vinylene analogue polymer 1, showing that the carbon-carbon triple bond could

play a unique role in sorting out a specific SWNT. The observed selectivity from polymer 3 could be attributed to a combination of the helical cavity size restrain and electronic interaction associated with the local chromophore arrangement. In order to shed light on the intriguing selectivity process, the polymer-SWNT interaction was investigated by using empirical force-field based molecular dynamics and dispersion-corrected density-functional calculations.

4.1 Method

The SWNTs involved in the present study are constructed based on sp^2 hybridization model. In order to study intrinsic properties, the ends of the nanotube were passivated by hydrogen atoms, resulting in a neutral bond-saturated SWNT segment. The initial value of b = 0.142 nm was used. The geometric structures of the SWNTs were fully relaxed in the MD simulations.

To facilitate an in-depth understanding of the electronic properties of methane intercalated graphene, herein we report on a theoretical study of the band structures based on a dispersion-corrected density-functional theory (DFT) approach. Our first-principles calculations are based on general gradient approximation (GGA) with the exchange correlation of Perdew–Burke–Ernzerhof (PBE) parametrization.[81] We employed the dispersion correction using the Tkatchenko-Scheffler (TS) scheme, which exploits the relationship between polarizability and volume.[81,82]

The TS dispersion correction takes into account the relative variation in dispersion coefficients of various atomic bonding by weighting values extracted from the

high-quality ab initio database with atomic volumes derived from partitioning of the self-consistent electronic density.[72, 82] A kinetic energy change of 3×10^{-4} eV in the orbital basis was sufficient to converge with the integration of the charge density.[72] The optimization of the atomic positions proceeds until the change in energy is less than 1×10^{-5} eV per cell.

4.3 Results and Discussion

The geometric structures of the SWNTs were fully relaxed in the MD simulations. A systematic evaluation of the available empirical force fields[106] showed that the MM3 and CHARMM force fields provide consistent results for both carbon nanotubes and polymer 3. The dynamic behavior of the polymer wrapping can be illustrated by tracking the energy optimization of the SWNT-Polymer 3 composite. Figure 4.3 illustrates the assembly process of polymer 3 wrapping on a (6,5) nanotube studied with MM3 force-field based molecular mechanics. To accelerate the evolution, it is efficient to keep bringing the carbon nanotube closer to the backbone of polymer 3. The subsequent geometry optimization of the whole nanomolecule is found to be one to two orders of magnitude faster than the conventional simulated annealing, without the necessity of resorting to approximations involved in confinement approach.[50]

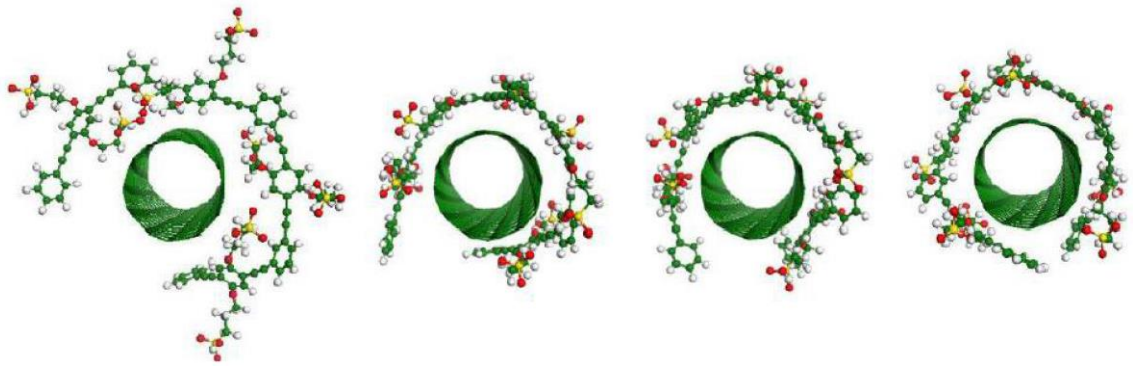

Figure 4.3. The frames generated from molecular mechanics optimization of polymer 3 wrapping around a (6,5) nanotube using MM3 force-field-based model.

Closer scrutiny of the local stable configurations displayed in Figure 4.3 reveals that the phenylenevinylene (PV) fragments are arranged either perpendicular or parallel to the SWNT surface in the assembly process to facilitate π-π interactions. The PE fragments, however, prefer a parallel arrangement after the optimization. In particular, the polymer forms a hexagonal shaped structure around the SWNT with a fixed distance between the nanotube surface and the polymer shell about twice the van der Waals (vdW) radius of a carbon atom.[106]

We plot a representative case in Figure 4.4 the optimized structure of an armchair (6,6) tube wrapped with polymer 3 in aqueous solution. The water molecules are able to go through inside the tube but are excluded from the interface. The exclusion of water leads to an enhancement of the hydrophobic interaction, and thus is helpful for the polymer wrapping. However, our present modeling results indicate that there is little geometry change of the wrapped tube in aqueous solution. In particular, the interfacial distance between polymer 3 and the nanotube remains intact. A detailed molecular

dynamics simulation study confirmed that the polymer 3 readily wraps around the SWNTs (Figure 4.3). The helical conformation of 3 provides a natural helical cavity that hosts the SWNT of a suitable diameter for intimate orbital interaction (Figure 4.3).

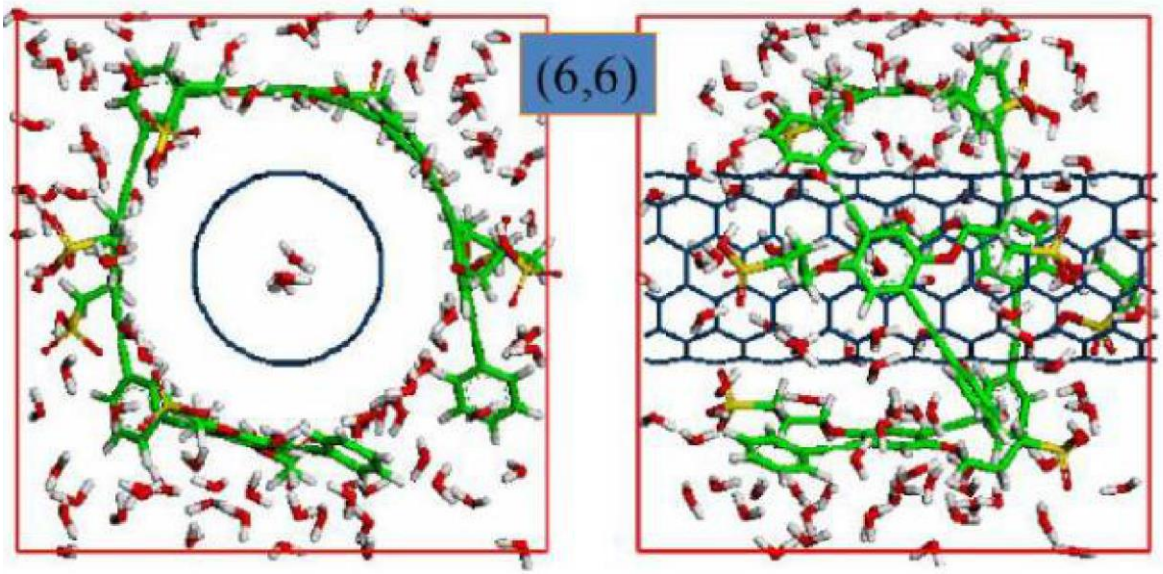

Figure 4.4. Top and side views of an armchair (6,6) tube wrapped with polymer 3 in aqueous solution. The calculation was performed using molecular mechanics simulation with MM3 force field.

In an effort to understand the electronic properties in this selective process, we have performed first-principles calculations for three representative SWNTs wrapped with polymer 3. The calculation was based on dispersion-corrected density functional method using double numerical basis set. The computational demanding first-principles calculation provides important information on the electronic structure. The structures obtained from force-field based molecular mechanics calculations were further fully optimized using the dispersion-corrected density-functional method.

The characteristic features of the electronic structure of the polymer 3 interacting with SWNTs can be illustrated by considering polymer 3 on graphene. As illustrated by the electronic band structure in Figure 4.5. The electronic band structure retains the semi-metallic feature of graphene, as the corresponding electronic density-of-states remains the characteristic linear behavior near the Fermi level.

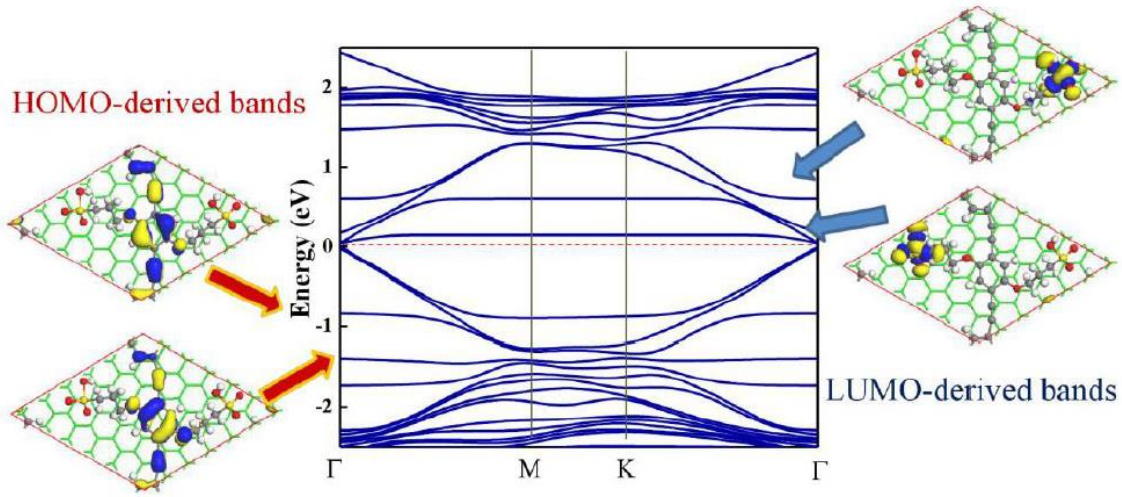

Figure 4.5. Calculated the band structure of polymer 3 on graphene, along with the charge density plots of the corresponding HOMO- and LUMO-derived bands of polymer 3. Blue and yellow colors characterize the positive and negative components of the wave function, respectively.

The effect of polymer 3 non-covalent functionalization is manifested in the presence of flat bands near the Fermi level, which are hybridized with the bands with dispersion that are attributed to the pristine graphene. In the absence of graphene, the highest occupied molecular orbital (HOMO) and the lowest unoccupied molecular orbital

(LUMO) have charges confined at 1-4 benzene and the sulfonyl group of the side chain, respectively.

The co-existence of electron donating and accepting components in polymer 3 leads to enhanced interactions associated with the electronic charge transfer. In this regard, the existence of water soluble side chain plays a pivotal role in efficient dispersion. An emerging question arises as to what happens to polymer 2, which possesses the same terminal groups.

As shown in Figure 4.6, the corresponding HOMO- and LUMO-derived bands have similar charge confinements for on 1-4 benzene and the sulfonyl group, respectively. However, the lack of charge confinement at *meta*-phenylene unit in polymer 2 indicates that polymer 2 is capable of helical wrapping and enhanced sectional charge transfer. The calculated interaction between polymer 3 and graphene reveals that the PPE backbone acts as charge donor, while the side chain sulfonyl group acts as charge acceptor.

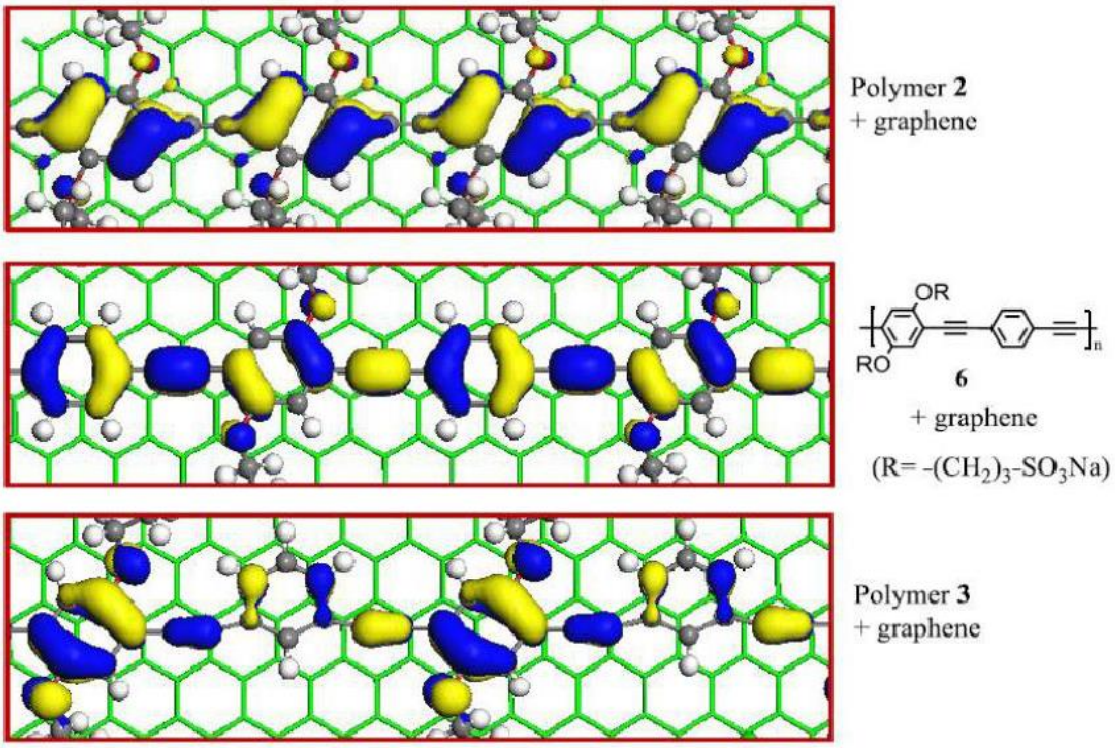

Figure 4.6. Charge density plots of HOMO- derived bands of polymers 2, 3, and 6 on graphene. The wave-function components are distinguished with blue and yellow colors, respectively.

To examine the polymer's affinity to different SWNTs, dispersion-corrected density-functional theory was employed to gain further insight into the polymer-nanotube interaction mechanism. The helical conformation of polymer 3 provides a natural helical cavity that hosts the SWNT of a suitable diameter for intimate orbital interaction (Figure 4.3 and Figure 4.7).

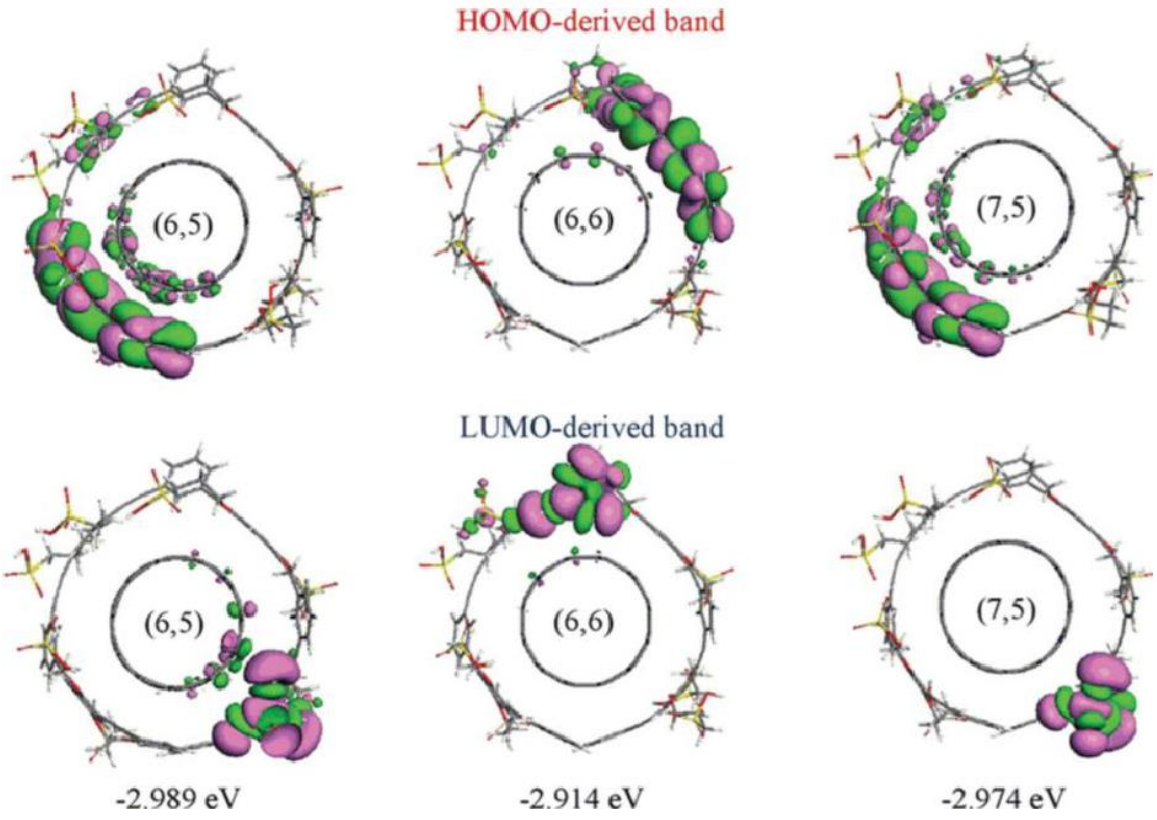

Figure 4.7. Extracted charge density of HOMO- and LUMO-derived bands of polymer 3 helically wrapped on (6,5), (6,6), and (7,5) SWNTs, respectively. The pink and green colors represent the positive and negative components of the wave function, respectively.

The binding energy was calculated from the first principles calculations for optimized composite and separate structures of nanotube and polymer 3 : $E = \frac{E_3}{SWNT} - E_{SWNT} - E_3$ where $\frac{E_3}{SWNT}$ is the total energy of the composite, E_{SWNT} is the energy of the nanotube without polymer wrapping, and E_3 is the energy of the polymer 3 without the nanotube. In other words, the binding energy can be calculated as the difference between the energy of optimized composite structure and the energy of separated nanotube and polymer 3. The result shows that the polymer-nanotube complex 3 /(6,5) has a binding

energy of − 2.989 eV, which is stronger than the nanotube complexes 3 /(6,6) and 3 /(7,5) (binding energies − 2.914 and − 2.974 eV respectively).

The extracted charge density of HOMO-and LUMO-derived bands is shown in Figure 4.7, revealing the enhanced interaction between polymer 3 and (6.5) SWNT. The extracted binding energy for (6,5), (6,6), and (7,5) demonstrates that (i) the smaller diameter (6,5) is energetically preferred over the slightly larger semiconducting (7,5) tube (by 0.015 eV per phenyleneethynylene (PE) unit), and (ii) for metallic (6,6) and semiconducting (7,5) tubes with virtually the same diameter, the semiconducting tube is energetically preferred (by 0.060 eV per PE unit). These results support the experimental findings that the metallic tubes are deselected as compared to the semiconducting tubes, while the smaller semiconducting (6,5) tube is favored over other semiconducting tubes.

The observed selectivity of semiconducting tubes over the metallic ones is attributed to the differences in the hybridization of HOMO and LUMO-derived bands of polymer 3 .[107–109] As seen from Figure 4.6, the HOMO-derived band from semiconducting tubes displays much stronger hybridization than that from the metallic counterpart. On the other hand, for the LUMO-derived bands, (6,5) shows stronger hybridization than (7,5), which is attributed to a quantum registry effect in that the band gap of nanotube (6,5) matches better with the HOMO-LUMO gap of about 1 eV for polymer 3.[107, 108]

In comparison with 3, the polymer 2 also forms the donor-acceptor complex resulting in enhanced interactions with graphene or carbon nanotubes.[109] However, the charge density distributions reveals distinctive electron donating behavior between

polymers 2 and 3. Specifically, the charge density of the highest-occupied molecular orbitals (HOMO) is confined at the 1-4 benzene rings of polymer 3 , in sharp contrast to the uniformly distributed electron donating contributions in polymer 2 Figures 4.6. Polymer 3 thus exhibits a distinct advantage in selective dispersion of SWNTs, because the presence of *meta* -phenylene unit provides not only a desirable bent angle for the flexible helical wrapping, but also a segmented charge transfer for ensuing donor-acceptor interactions.

In conclusion, a water soluble polymer P m PE p PE has been synthesized, in which the *meta*- phenylene unit introduces a bent angle along the polymer backbone to facilitate the helical conformation. In aqueous, the polymer is found to disperse SWNTs with good selectivity toward the (6,5) and some selectivity toward (8,3) SWNTs (see Figure 4.2 and Figure 4.7), which have the small diameters (d = 0.757 and 0.782 nm, respectively). The intriguing selectivity is partly due to the helical conformation of polymer backbone, whose cavity size could act as pre-sort mechanism to select the tubes of small diameters (Figure 4.5). The SWNTs of similar diameters are further differentiated by interaction with the local phenyleneethynylene (PE) chromophores, whose assembly is guided by the helical conformation and assisted by the low rotational barrier of C≡C bonds. Selective dispersion of small diameter (6,5) SWNT illustrates that the synergistic effect of the quantum registry and the helical conformation cavity can be an effective tool to aid the SWNTs sorting. Clearly, the P m PE p PE 3 is superior to its vinylene analogue polymer 1 in terms of selective SWNT dispersion,[110] as the paraphenylenevinylene unit in polymer 1 does not align parallel to SWNT surface for π –

π interaction. Integration of a size control mechanism (via polymer conformation here) with a suitable molecular interaction, therefore, could offer a promising strategy to achieve the isolation of a specific SWNT.

CHAPTER 5

IMPACT OF Π-Π INTERACTION MODE POLYMER CONFORMATIONS AND VINYLENE BOND GEOMETRY ON HELICAL WRAPPING OF CARBON NANOTUBES

5.0 Introduction

Carbon nanotubes (CNTs) represent an intriguing class of materials currently being utilized for the exploration of nanostructured composites as well as applications in nanoerlectronics.[111,112] Undoped single-walled carbon nanotubes (SWCNTs) ae unique among solid-state materials because of their unmatched characteristics arising from both metallic and semiconducting SWNTs.[113] However, as-synthesized samples inevitably yield mixed bundles of metallic and semiconducting tubes.[114, 115] It is necessary to develop proper dispersion methods to obtain pure SWCNTs for fabrication of nanoelectronic devices. The solubilization of SWCNTs can be achieved via covalent sidewall functionalization, which involves the destruction of C-C bonds on tubes and may lead to deterioration of both mechanical and electronic properties.[114] On the other hand, non-covalent supramolecular modifications involve polymer wrapping on the surfaces of SWCNTs, preserving desired properties. [114] Chiral-selective reactivity and redox chemistry of CNTs are promising methods for the development of techniques that isolate CNTs into pure samples of a single electronic type and promote reversible doping

of CNTs for electronic applications. [96,108,116-119] Since π-conjugated polymer wrapping around the nanotube provides a useful means for individualizations, an in-depth understanding the π-π interaction between conjugated polymers and the nanotube is of great importance in nanoelectronic applications. Noncovalent attractive π-π interactions between the π–electrons of unsaturated organic systems play a key role in many aspects of modern chemistry, materials science, and biochemistry. [111,112] When these interactions occur between parallel oriented π–systems, the term "π-π stacking" is typically used. The simplest prototype system with π-π stacking is the benzene dimer, and thus considerable attention has been dedicated to exploring the structural and electronic properties as a preliminary investigation.

As a soluble π-conjugated polymer, poly[(m-phenylenevinylene)-alt-(p-phenylenevinylene)] (PmPV) is a prototype polymer for dispersing SWCNTs. [110,120-132] Several experimental studies of wrapping SWCNTs with PmPV derivatives have been reported, which show selective interactions with SWNTs by diameter and chirality.[114, 129] However, the nature of this selectivity due to the non-covalent interaction between PmPV and SWCNTs is not fully understood. [114] To understand interfacial chemistry and the dispersion mechanism, we have employed force- field-based molecular dynamics (MD) and first-principles density-functional calculations to study the optimum geometry and electronic interaction between a pair of benzene molecules, which is essential in PmPV wrapped SWNTs. Force-field-based MD was used to investigate the wrapping process and the binding properties, and first-principles calculations were employed to determine the electronic structure.

Our results demonstrate that the semi-rigid π-conjugated polymer backbone is flexible enough to adjust its conformation during successive helical wrapping. The helical-wrapping induced effective dispersion is critical for enabling the development of nanodevices with optimized properties, and developing multifunctional nanocomposites capable of bearing structural loads and functioning as sensors.

5.1 Method

All our calculations have been performed using the Gaussian 03, [133] Materials Studio 5.5, [72] and TeraChem 1.0 [134,135] packages. The structures of isolated benzene monomers and various geometrical conformations of the benzene dimers were optimized using B3LYP method [136,137] with 6-311G and 6-311++G basis sets, second order Møller–Plesset perturbation (MP2) [138] with 6-31G(d,p) polarized valence basis set or aug-cc-pVDZ polarized valence basis set with augmented diffuse functions. The energy minimum for all optimized structures was confirmed from vibrational frequency analysis. All geometry optimizations and single-point calculations utilized the frozen core approximation. The conformations were optimized at the MP2/6-31G(d,p) level that were subsequently used for the calculations of dimmers interaction energies. The single-point energy calculations, including calculations of the interaction energies for all dimmers, have been performed in the framework MP2/aug-cc-pVDZ approach. Basis set superposition error (BSSE) correction has been taken in to account by the counterpoise method (CP). Moreover, three-body electron correlations, described by triple excitations relative to the reference configuration, are also significant. Hence, coupled-cluster

computations with perturbative triples [CCSD(T)] have also been performed and combined with the Hartree-Fock and MP2- R12/A values to estimate complete basis CCSD(T) binding energies for benzene dimer, which should be accurate to a few tenths of a kilocalorie per mole. In addition, calculations were performed within DMol3 approach[72] with triple numerical polarized (TNP) basis functions and empirical dispersion corrected density-functional approaches.

The structure and electronic properties of different conformations were investigated using dispersion-corrected first-principles density-functional theory calculations. [132,139,140,141] We used the Perdew-Burke-Ernzerhof (PBE) parameterization of the generalized gradient approximation (GGA). The generalized-gradient-approximation (GGA) results were subsequently rectified through the inclusion of dispersion correction. [110,129] Tkatchenko-Scheffler (TS) dispersion correction accounts for the relative variation in dispersion coefficients of differently bonded atoms by weighting values taken from the high-quality ab-initio database with atomic volumes derived from partitioning the self-consistent electronic density. The TS scheme exploits the relationship between polarizability and volume. The inclusion of dispersion-correction is essential to describe the non-covalent interactions between PmPV and SWNTs correctly.

A kinetic energy cutoff of 280 eV in the plane-wave basis and a kinetic energy tolerance less than 3×10^{-4} eV in the orbital basis, and appropriate Monchorst-Pack k -points (1×1×10) were sufficient to converge the grid integration of the charge density. The initial search for stable structures was carried out through force-field based molecular dynamics.[142] The resultant structures were further optimized through first-

principles calculations with forces less than 0.01 eV/Å with plane wave basis. We used force-field based molecular dynamics for geometry optimization. Geometry optimization calculations were employed using conjugated gradient.

5.2 Results and Discussion

We have investigated the structures of the benzene dimer using different level of the theory, including accurate MP2 method with extended basis set and less expensive dispersion-corrected first-principles density-functional calculations.[132, 142] We have used the Perdew-Burke-Ernzerhof (PBE) parameterization of the generalized gradient approximation (GGA) double numerical (DN) basis set. For geometry optimization, the starting geometries of the dimer were built up taking into account the well-known sandwich S (D_{6h}), parallel displaced PD (C_{2h}), T-shaped (C_{2v}), and Y-shaped (C_{2v}) structures (see Figure 5.1 top panel). After initial optimization, the imposed symmetry constraint was released. Coupled with intensive simulated annealing, three low-energy structures PD-A (C1), PD-B (C1), and Y-displaced YD (C1) were obtained (Figure 5. 2).

We show in Figure 5. 1 the optimized structures of a benzene pair. In the simple model of aromatic π-π interactions, two interacting benzene rings can be aligned in parallel displaced, P (Figure 5.1b) or perpendicular geometry (edge-to-surface interaction). As seen from Figure 5.1, in the conformation S and PD, the planes of the two benzene rings are virtually parallel to each other while one of the rings in structure PD is displaced in the *ortho* direction.

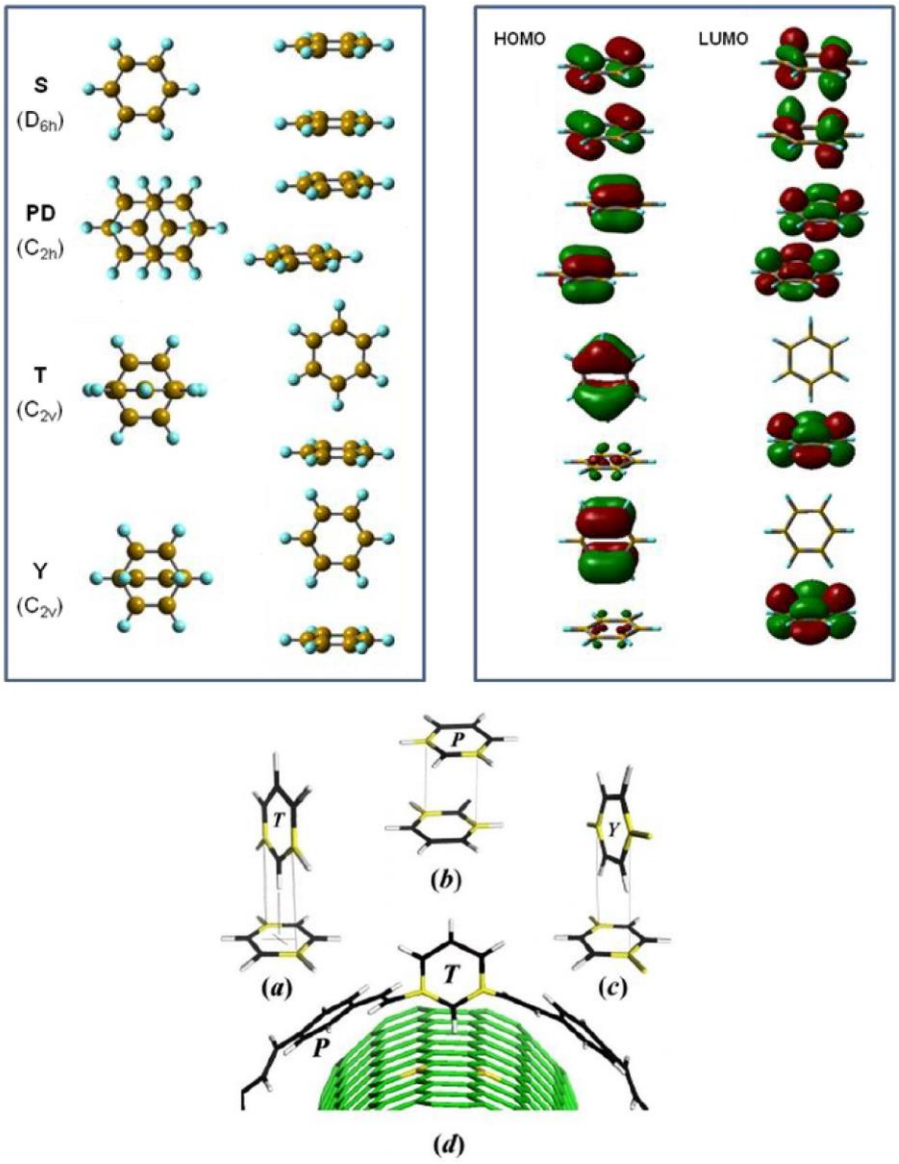

Figure 5.1. (Top panel) Optimized structure of sandwich S (D_{6h}), parallel displaced PD (C_{2h}), T (C_{2v}) and Y-shaped Y (C_{2v}) structures along with the charge density of each shape for highest occupied molecular orbital (HOMO) and lowest unoccupied molecular orbital (LUMO). (Bottom panel) Optimized structures of T-shaped (a), Y-shaped(c), parallel-displaced (b) benzene pair and a phenylene (of PmPV) on SWNT (d).

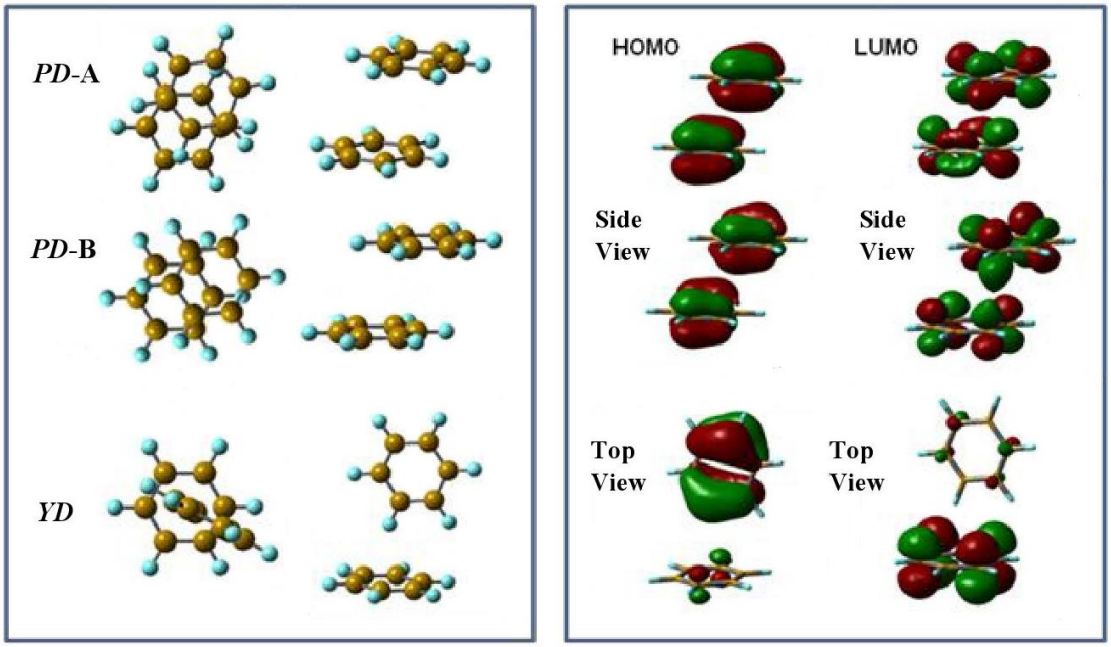

Figure 5.2. Optimized structures and charge density plots of lowest energy conformations (parallel displaced (*ortho* direction) PD-A, parallel displaced (*meta* direction) PD-B and Y-shaped).

The parallel arrangement of the electronic charges favors the π-π stacking interaction between the benzene monomers. The same is true for PD-A and PD-B as well (see Figure 5.2), which can be obtained from S by in-plane shifting of one of the monomers in two different directions, followed by a small rotation of the displaced benzene ring. The difference between these two conformations is that one of the benzene monomers in PD-A and PD-B is displaced along *ortho* and *meta* directions, respectively. The edge-to-surface interaction can be further classified into the T-shaped (Figure 5.1a) or Y-shaped conformations (Figure 5.1c). In T-shaped structure, a hydrogen atom on a benzene ring is pointing towards the center of another ring. In the Y-shaped

conformation, two of the hydrogen atoms on a benzene ring are pointing to the two carbon atoms of another ring.

Recent studies in π-π interactions of aromatic liquids reveal that benzene-benzene interaction geometry depends on separation distance.[143-145] At small molecular separations (< 5 Å) there is a preference for parallel π-π contacts (P-shaped) in which the molecules are offset to mimic the interlayer structure of graphite. At larger separations (>5 Å) the adjacent aromatic rings are predominantly perpendicular (Y-shaped), with two H atoms per molecule directed toward the acceptors π- orbitals. It is worth noting that so-called anti-hydrogen-bond configuration (T-shaped), which was proposed theoretically as the global minimum for the benzene dimer, occurs only as a saddle point in the experimental study. [143-145] Quantum chemistry calculation results suggest that the off-centered parallel displaced, and T-shaped structures are nearly degenerated.[146-150] Molecular dynamic studies confirm that off-centered parallel-displaced or T-shaped structures are favorable depending on the magnitude of the partial charges used in the electrostatic model.[151] Small charges stabilize parallel displaced geometries while the large partial charges favor T-shaped structures.[151]

Illustrated in Figure 5.3 are extracted energies from various levels of theory. Initially, we have performed geometry optimizations for the ground states of the conformers using Hartree-Fock method (HF) with the basis set 6-311++G. The finding confirms that HF underestimate the π-π stacking interaction. The analysis of the results obtained at MP2/aug-cc-pVDZ+BSSEC39 level show that the most stable conformations

are non-symmetrical parallel displaced structure PD-A, and PD-B. The interaction energies for these dimers are -4.3, and -4.2 kcal/mol, respectively.

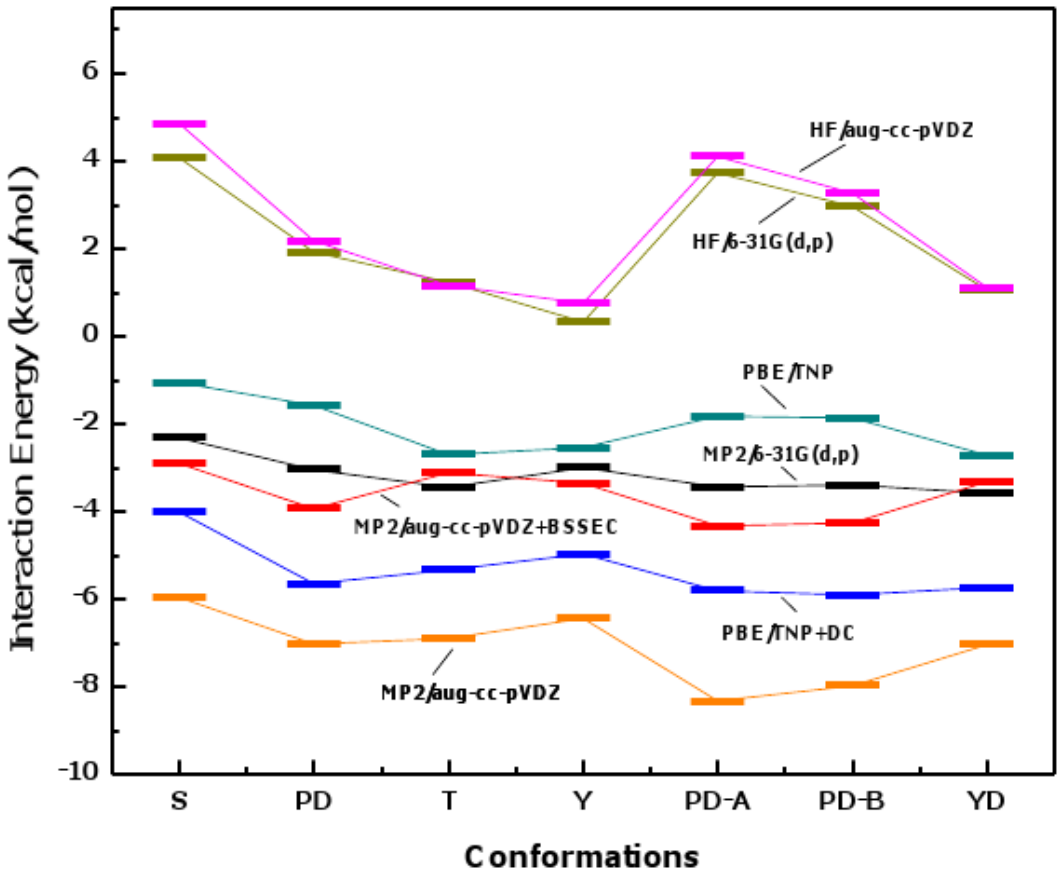

Figure 5.3. Interaction energies of sandwich (S), parallel displaced(PD), T-shaped(T), Y-shaped(Y), Parallel Displaced (*ortho* direction) (PD-A), parallel displaced (*meta* direction) PD-B and Y-displaced (YD) structures with MP2/aug-cc-pVDZ, PBE/TNP+DC, MP2/aug-cc-pVDZ+BSSEC, MP2/6-31G(d,p), PBE/TNP, HF/6-31G(d,p) and HF/aug-cc-PVDZ methods.

Slightly higher in energy is the parallel displaced structure PD, with interaction energy of -3.9 kcal/mol. The T-shaped and Y-shaped structures are almost isoenergetic (-3.1, -3.4 kcal/mol) with the YD structure (-3.3 kcal/mol) and significantly higher in

energy than PD conformations. The perfectly stacked structure S is much less stable, with an interaction energy of -2.9 kcal/ mol. The analysis of the obtained result shows that the relative energies of these 7 configurations are similar, indicating a very flat potential energy surface. The lowest energy structures are PD-A and PD-B. The S configuration is the least favorable of the seven geometries examined. It is remarkable to see from Figure 5.3 that computationally much less expensive PBE/TNP method with dispersion correction show results qualitatively similar to that obtained using time-consuming MP2/aug-cc-pVDZ+BSSEC approach. Closer scrutiny of the locally stable configurations displays in Figure 5.1d reveal that the phenylene fragments are arranged either perpendicularly or parallel to the SWNT surface. Parallel or perpendicular assembly facilitates the π-π interactions. As seen from Figure 5.1d, the *meta*-linked benzene ring tends to adopt T-shaped or its slanted variant. The *para*-linked benzene ring can adopt either P- or Y-shaped configurations, depending on the chirality of the nanotube, as well as the wrapping pattern. Specifically, the stereoisomers, *cis* and *trans*, play an important role in the wrapping pattern and also contribute to the availability of T-shaped, P-shaped or Y-shaped configurations in the hybrid.

Experimental results indicate that the benzene rings in *cis*-PmPV prefer perpendicular orientations to the SWNTs, as predicted from the extended π-conjugation along the polymer chain.[152] It is assumed that the *meta*-linked phenylene ring adopts the perpendicular orientation (to SWNT surface), as the bent angle at the *meta*-phenylene provides necessary curvature to wrap SWNT. Benzene rings that are connected at their '*para*' positions (i.e. *para*-phenylene), however, can adopt either perpendicular or parallel

orientation to SWNT surface. The ratio of *para*-phenylene in perpendicular and parallel orientation is dependent on the local polymer-SWNT interaction. The *cis*- and *trans*-vinylene bond geometry may also affect the ratio of perpendicular and parallel orientation of *para*-phenylene. Repeating unit of *trans*- and *cis*-vinylene stereoisomers of a PmPV are shown in Figure 5.4 right panel.

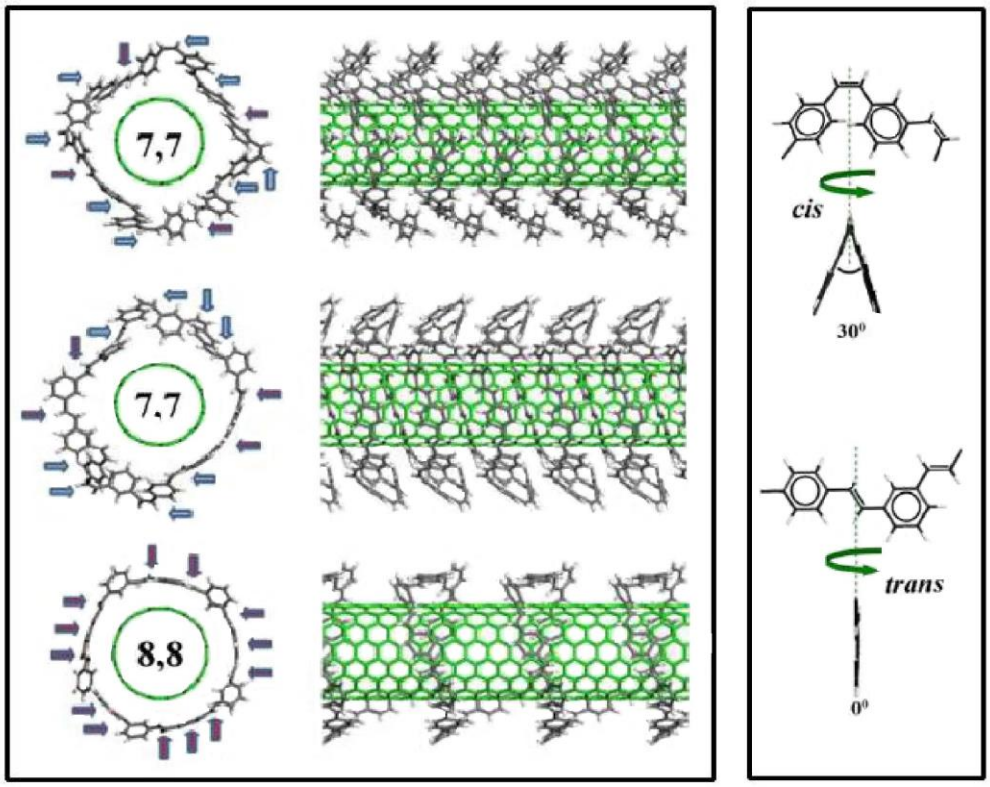

Figure 5.4. Left panel: Optimized structures of wrapped *cis*-PmPV (*trans*: *cis* ratio 1:2; left panel top figure), *cis*-PmPV (*trans*: *cis* ratio 2:4), and *trans*-PmPV around SWCNT (left panel bottom figure). Right panel: *cis* and *trans* monomers of PmPV.

In the *trans* isomer, two benzene rings are in the same plane. Two benzene rings in the *cis* isomer, however, are rotated away from each other by 30^{o} angle, due to the

steric hindrance. In other words, the two phenylene rings in the cis isomer are forced to rotate away significantly from the co-planarity. The dihedral angle between the two phenylene planes remains unchanged after wrapping around the SWNTs (Figure 5.4 left panel). In one aspect, polymer chain rigidity, as a consequence of the extended π-conjugation, prevents the parallel positioning of the benzene rings.

We have investigated two types of polymer chains according to their concentration of cis and trans isomers linkages by considering two monomer units shown in Figure 5.4. The polymer chain, referred to as *cis*-PmPV, has a 1:2 ratios between *trans* and *cis* monomer units. The polymer chain, referred to as *trans*-PmPV, has a trans configuration throughout the polymer chain. Furthermore, we have examined configurations with different *trans* and *cis* units for *cis*-PmPV, specifically 1:2 and 2:4 ratios, to assess the stability of the nanohybrids. The self-assembled polymer chains, which are wrapped helically around the nanotube, result in a very short pitch for *cis*-PmPV (Figure 5.4 top).

In other words, *cis*-PmPV is wrapping SWNT more tightly than *trans*-PmPV. The shorter the pitch of the polymer wrapped around SWCNTs, the more efficient is the dispersion. Our calculation results indicate that *trans*-PmPV (Figure 5.4 bottom) has a 2.5 nm pitch, in good agreement with experimental observations.[152] On the other hand, we have found that *cis*-PmPV has a 1.5 nm pitch length. The difference in pitch length is in agreement with experimental findings that the *trans*:*cis* isomer ratio 1:2 yields stronger interactions between the polymer and the tube. The wrapping pattern is rigid in *cis*-PmPV due to the fixed angle between the two benzene rings in the monomer unit.

In general, the wrapped structure assumes an n-fold polygonal shape where the number of polymer units wrapped around the nanotube is related to the tube diameter and the side-chain length. The *trans*-PmPV isomer prefers the SWNTs with large diameters because larger tubes have bigger contact area. Hence, the *trans*-PmPV isomer with higher chain rigidity shows better selectivity in comparison to the more flexible *cis*-PmPV wrapping. Therefore, the orientation order plays a nonessential role in the selectivity of the SWNTs. The PmPV conformation as shown in Figure 5.4 has 13 and 14 *meta* and *para* linkages, respectively. It was observed that para linkages prefer to be parallel to the surface of the tube while the meta linkages are slanted to the surface of the nanotube. Side chains play a significant role in the wrapping of PmPV along the SWCNT, for connectivity in between the side chains affects the bonding to the polymer chain. Side chains with donor-acceptor interactions lead to the successful selectivity of SWCNTs. There is a great chance for para-linked benzene rings to adopt Y-shaped over P-shaped configurations after wrapping around SWCNTs, following the behavior of pairs of aromatic rings. The side chains are attached to the para-linked benzene rings in their meta and ortho positions. The interactions of side chains limited the rotations of the para-linked benzene rings in the *trans*-PmPV polymer and thus lower the available Y-shaped configurations.

In Figure 5.5, we present the calculated electronic band structure for *cis*-PmPV, interacting with metallic (8,8) and semiconducting (14,0) SWCNTs, respectively. The charge density plots indicate that the charges are localized in the polymer chain of the *cis*-PmPV/(8,8)-SWCNT hybrid. This observation is supported by the degree of

dispersion in the HOMO-derived band (highlighted red arrows in Figure 5.5). For the *cis*-PmPV/(14,0)-SWCNT hybrid, charge densities are predominantly concentrated on the tube.

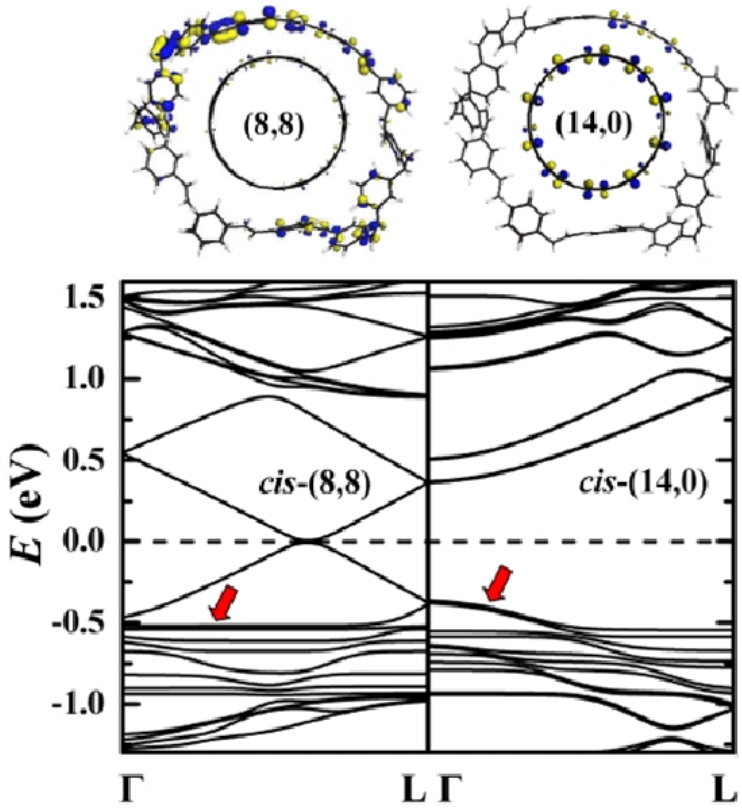

Figure 5.5. Top panel: charge density plots of *cis*-PmPV around the metallic (8,8) and semiconducting (14,0) SWCNTs. Bottom panel: Calculated electronic band structure for *cis*-PmPV, with metallic (8,8) and semiconducting (14,0) SWCNTs.

These findings indicate that the *cis*-PmPV polymer primarily shows a preference for metallic tubes. The hypothesis is also supported by the calculated binding energies shown in Table 5.1.

Table 5.1. Calculated Binding Energy Differences in eV with Respect to the Lowest Energy Conformation by Using LDA (E_{LDA}) and GGA (E_{GGA}) Parametrization, Energy Gap Between HOMO and LUMO (E_g), Length of the SWCNT (L) and Diameter of the SWCNT (*d*). (Dash (-) Represents the Lowest Energy Conformation in Each Calculation)

Structure	E_{LDA} (eV)	E_{GGA} (eV)	E_g	*L* (Å)	*d* (Å)
H-*trans* (8,8)	-	0.63	0	12.3	3.4 – 3.9
P-*trans* (8,8)	1.07	-	0	12.3	3.3 – 3.7
H-*trans* (8,8)	3.32	5.85	0	12.3	3.8 – 5.4
H-*trans* (14,0)	-	0.18	0.75	12.8	3.3 – 3.7
P-*trans* (14,0)	0.37	-	0.75	12.8	3.2 – 3.5
H-*trans* (14,0)	3.35	4.96	0.76	12.8	3.6 – 5.1
cis (8,8)	-	-	0	6.6	3.0 – 6.3
cis (14,0)	1.22	4.64	0.75	6.9	2.9 – 6.0

Another important aspect of this study is to clarify the relative stability of T-shape, slanted T-shape, or parallel dispersed benzene dimer configurations. For this reason, we have studied three different conformations of *trans*-PmPV polymer wrapped SWCNTs. These conformations include all-vertical-T (the polymer conformation with all of the benzene rings are vertical to the SWCNT surface), conformation with half of the benzene rings are vertical to the SWCNT surface), and the parallel-P(the polymer (the polymer conformation with all the benzene rings are parallel to the SWCNT) conformations.

Summarized in Table 5.1 are the calculated diameters, along with the band gap values for various conformations of the π-conjugated *trans*-PmPV polymer chains

interacting with the SWCNTs. The total energy order for each structure conforms to force-field-based MD calculation results. We compared the pitch of the helically wrapped polymer chains and the van der Waal distances between the polymer and the nanotube. We also show in Table 5.1 the binding energies of the different conformation with respect to the corresponding lowest energy conformation for each tube. As seen from Table 5.1, the relative stability of half (H) and all-vertical (T) conformations depends on the calculation methods.

Specifically, with the use of GGA exchange-correlation, the parallel conformations are preferred. By contrast, with the use of LDA as the exchange-correlation then the half-vertical conformations are preferred. The polymer conformation with all the benzene rings perpendicular to the SWCNT (T-*trans*) is not a low energy conformation. Calculations reveal the all vertical is not preferred, although it is more tightly wrapped around. The smaller helical pitch of *cis*-PmPV is nearly half that of the *trans*-PmPV conformation. The tight wrapping pattern is in agreement with the experimentally observed high dispersion of the tubes onto the polymer.

Band structure of *cis*-PmPV polymer wrapped metallic-SWCNTs contains both dispersed bands and flat bands (Figure 5.5). Flat bands originate from the PmPV and dispersed bands originate from SWCNTs. Valence bands are affected due to the hybridization of SWCNTs bands with the *trans*-PmPV polymer flat bands, which allow for the observation of the highest occupied molecular orbital (HOMO)-derived bands. These findings imply that the PmPV polymer acts primarily as an electron donor to SWCNTs. We have plotted the charge density together with band structures and found

that hybridization is strong when the parallel conformation conjugated with the metallic tubes, followed by the vertical, half vertical conformations, respectively. We illustrate in Figure 5.6 the characteristic features of the electronic structures of the semiconducting-SWCNT wrapped with a *trans*-PmPV polymer. The distribution of the HOMO-derived band, in the occupied states, continuously increases starting from half-vertical, parallel, and then to all-vertical conformations after interacting with the semiconducting SWCNT (Figure 5.6). For the case of semiconducting SWCNTs, calculated charge densities for the homo-derived bands indicate that the hybridization is higher in the half-parallel and parallel conformations of PmPV compared to that of the all vertical conformations.

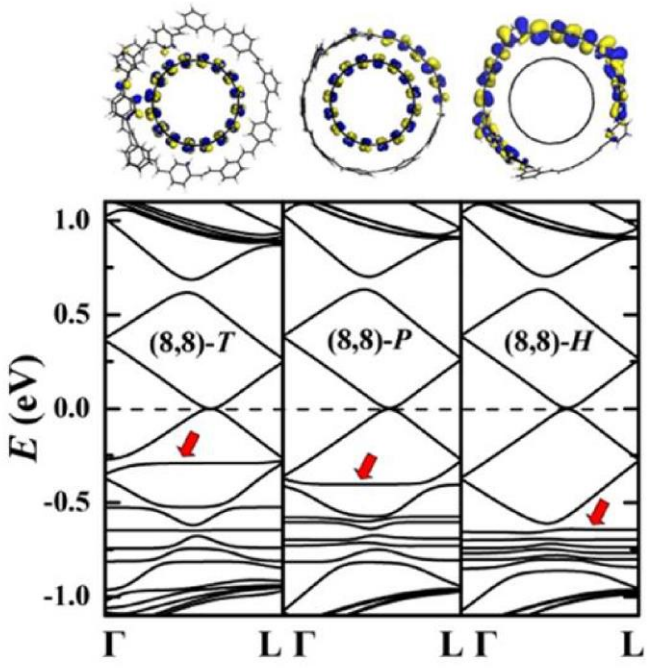

Figure 5.6. Top panel: charge density plots of *trans*-PmPV with all vertical benzene rings (T), parallel benzene rings (P) and half vertical benzene rigs (H) around the metallic (8,8) SWNT. Bottom panel: Calculated electronic band structure for *trans*-PmPV, with metallic (8,8) SWCNT.

In summary, we performed a systematic modeling study that provides crucial insights into the selective interactions between SWCNTs and π-conjugated polymers. Since the diameter and chirality of the nanotubes dictate their mechanical properties as well as electrical conductivity, an in-depth understanding of the interactions between conjugated polymers and carbon nanotubes is of great importance. The study reveals that the *cis*- and *trans*-vinylene bond geometry plays an important role to influence the orientation of the polymer's phenyl rings toward SWCNT. When PmPV is wrapping around an SWCNT, the optimum polymer-SWCNT interaction appears to be dependent on the molecular ability to adjust the orientation of phenyl ring, which is essential for achieving optimum interaction via adopting Y- or PD-interactions (listed in Figure 5.1). The approach thus shed light on the details of intermolecular interaction between PmPV and SWCNT, which can be employed to the novel π-conjugated polymers. Investigation of relevant structural and electronic properties is important for the development of nanotube based nanoelectronics and nanostructured composite.

CHAPTER 6

FILLED PENTAGONS AND ELECTRON COUNTING RULE FOR BORON FULLERENES

6.0 Introduction

In accordance to the "Aufbau principle" [67] stable boron conformations can be constructed from two basic building blocks: the pentagonal pyramid B_6 and the hexagonal pyramid B_7. The hexagonal B_7 is the precursor for convex and quasi-planar boron clusters, and thus closely correlates to the α-BS and the associated boron nanotubes.[55] The pentagonal B_6 unit is an aromatic component that has attracted interest in planar boron clusters, such as B_{19}. [54] In this regard, we have studied a volleyball-shaped B_{80} fullerene that is lower in energy than the previously assumed B_{80} buckyball.[66] Contrary to the core-shell structured $B_{12}@B_{68}$, it preserves the desired electronic properties as the boron counterpart of C_{60}.[66]

A natural question arises as to whether there exists a "magic" boron fullerene in lieu of the latest developments.[66,68,69,153] An important consequence of the stability for the B_{80} volleyball is that in addition to the hollow pentagon, hollow hexagon, and filled hexagon, [63] it is necessary to add the pentagon pyramid in the building blocks. [66] Herein we present a revised constructing scheme and demonstrate that the migration of capping atoms from hexagonal pyramids to pentagonal rings leads to highly stable boron

fullerenes. Consequently, the electron counting rule is revisited by taking into account the effect of enhanced stability related to the B_6 pentagonal pyramids.

6.1 Method

We have employed first-principles calculations based on local and semi-local density-functional approaches. For selecting structural conformations and geometry optimizations, gradient-corrected Becke-Lee-Yang-Parr (BLYP) parametrization [136,137] of the exchange−correlation was used along with double numerical (DN) basis set as implemented in the DMol3 package.[72] The local density-functional calculation results were subsequently rectified through semi-local approach using Becke-3-Lee-Yang-Parr (B3LYP) for exchange−correlation functional,[136,137] with 6-311G basis set as mplemented in the TeraChem package.[154] The optimization of atomic positions was performed for local and semi-local calculations, which proceeded until the forces were less than 0.01 eV/Å and the change in energy was less than 5×10^{-4}eV.

6.2 Results and Discussion

It is instructive to examine the buckyball and volleyball structures of B_{80} as shown in Figure 6.1. The structure of the vibrational stable T_h-B_{80}(T_h-A) [155] consists of 20 filled hexagons and 12 empty pentagons.[53] The filled hexagons are arranged in a snowdrop-like pattern as highlighted in Figure 6.1.[53] The snow-drop constitutes a central hexagonal pyramid surrounded by three hexagonal pyramids and three “hollows” (hollow pentagons or hexagons). By contrast, the B_{80} volleyball can be viewed as the 12 outward

capping atoms migrating from hexagonal pyramids to the centers of 12 empty pentagons.[66] We illustrate in Figure 6.1 the transition state between the buckyball and volleyball of B_{80} with an energy barrier ~ 39 eV and the 12 capping atoms are highlighted. A transition state search employing a combination of LST/QST algorithms (implemented in DMol3 package) facilitates the evaluation of energy barriers. For transition state calculations, we started with the T_h-A conformation of the buckyball B_{80} and ended with the volleyball B_{80}.

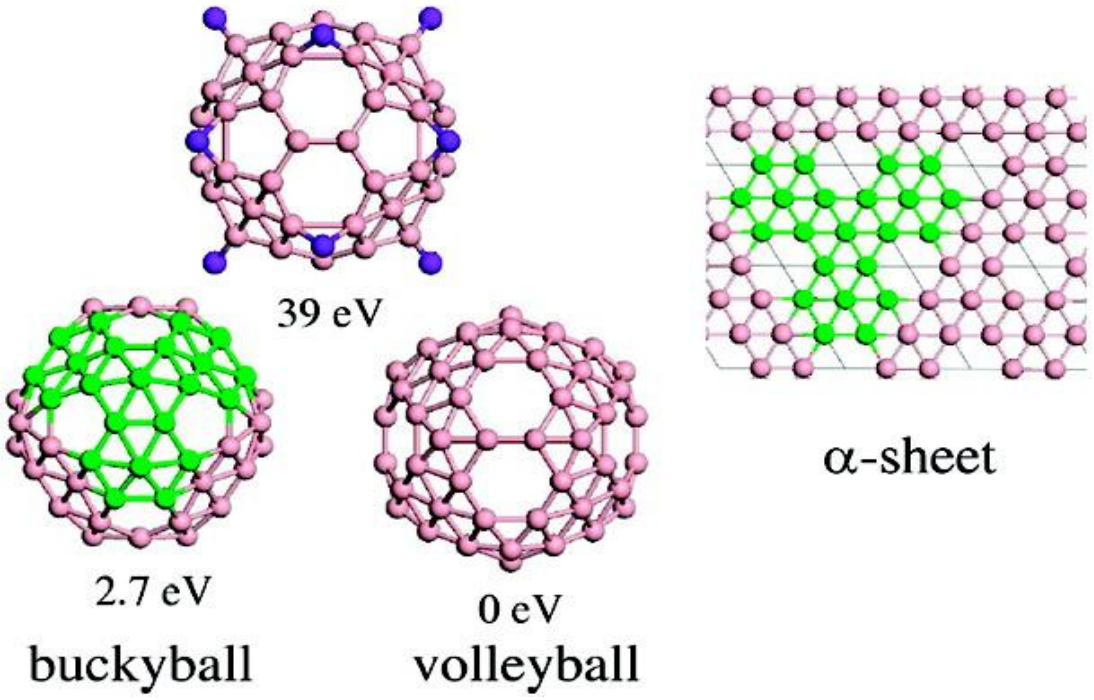

Figure 6.1. Ball-and-stick representation of the optimized T_h-A B_{80} buckyball and volleyball, along with the transition state between the two conformations and the α-boron sheet. Highlighted with green and purple are the snow-drop pattern and the migrating capping atoms, respectively.

It is worth noting that both ending configurations are (locally) stable as all the vibrational frequencies are real. An extrapolation of the two conformations with 10 intermediate images constitutes the initial pathway. The energy barrier is calculated to be the energy difference between the transition state and the volleyball. The exchange between B_6 and B_7 pyramids leads to yet another route of generating a family of boron fullerenes.

Carbon fullerenes consist of hexagons and 12 pentagons in conformity with Euler's formula $F - E + V = 2$, where F, E, and V stand for the number of faces, edges, and vertices of the fullerene, respectively. The exactness of 12 pentagons is attributed to the fact that each edge is shared by two faces, each pentagon (hexagon) has 5 (6) edges, and each vertex is adjacent to three polygons. Let nP (nH) denote the number of pentagons (hexagons), so that $F = nP + nH$, $E = (5nP + 6nH)/2$, and $V = (5nP + 6nH)/3$. Therefore $nP = 12$.

The isoelectronic requirement for carbon and boron fullerenes implies that the addition of more than 60 carbon atoms needs to be a multiple of 6 for the even number of carbon fullerenes and the trivalent boron, respectively. As a result, the counterpart of C_{60+6n} isolated-pentagon fullerenes is B_{80+8n}. The isoelectronic requirement is important for a closed-shelled electronic structure in that typical high-symmetry boron fullerenes are open-shelled in the absence of such a constraint. For snow-drop B_{80+8n} fullerenes that constitute hexagonal pyramids in additional to pentagonal and hexagonal rings, it is straightforward to conclude that $nP = 12$, $nH = n$, and the number of filled hexagons (FHs) $nFH = 20 + 2n$, since each filled hexagon has 12 edges and 6 triangular faces. For snow-

drop generated boron nanostructures, the total number of valence electrons, 240+24n, is twice the 120+12n triangles.[63] It is worth noting that the snow- drop electron counting rule is applicable to α-BS as well.

Encouraged by the improved stability of the B_{80} volleyball over the B_{80} buckyball,[66] herein we propose a filled pentagon model for boron fullerenes. Specifically, the filled-pentagon (FP) scheme amounts to moving 12 capping atoms from filled hexagons to pentagons, resulting in nP = 0, nH= 12 + n, nFH= 8 + 2n, and nFP = 12. Consequently, the revised electron counting rule yields more than 2 electrons per triangle, which is dependent on n but still converging to an α-BS value of 2 as $n \rightarrow \infty$.

Following the nomenclature, hereafter we refer to the filled-hexagon fullerenes as snow-drop fullerenes. [63,156] In contrast to the snow-drop model where the constructed boron fullerenes are of the same symmetry as the carbon fullerenes counterparts, the filled-pentagon fullerenes typically have lower symmetry. The lack of a unique migration path adds another wrinkle to the search for global minimum conformations of boron fullerenes. Owing to the large number of boron atoms involved and the complicated two- and three-center bonding patterns, the associated first-principles density-functional theory calculations are computationally demanding. Furthermore, owing to the extremely sensitive dependence upon the basis set and the exchange-correlation functional employed, it is necessary to carefully evaluate the local and non-local effects in ab- initio calculations.

Shown in Figure 6.2 are the optimized structures of B_{96}, B_{104}, and B_{112}, which are the isoelectronic counterparts of C_{72}, C_{78}, and C_{84}, respectively. The snow-drop B_{96}

fullerene has a round pillow shape with two hexagonal rings located at the D_{6d} axis. The filled-pentagon B_{96} structure is formed by moving 12 of the 24 capping atoms to fill the 12 pentagons, leaving 14 hollow hexagons. On the equator of D_{6d}-B_{96}, three alternating pairs of hexagons move the capping atoms to the centers of nearest-neighbor pentagons, while the two snow-drop structures near the D_{6d} axis rotate to fill three empty pentagons each. The B_{104} counterpart of C_{78} has five isomers,[156] and the snow-drop B_{104} is of D_{3h} symmetry. Among various ways of migrating 12 capping atoms, we show in Figure 2.2 two low-energy C_{2v} conformations: one has empty hexagons around the equator, while the other has more isolated hexagonal rings. The construction of both conformations involves rotating two snow-drops and hexagonal pair migrations.

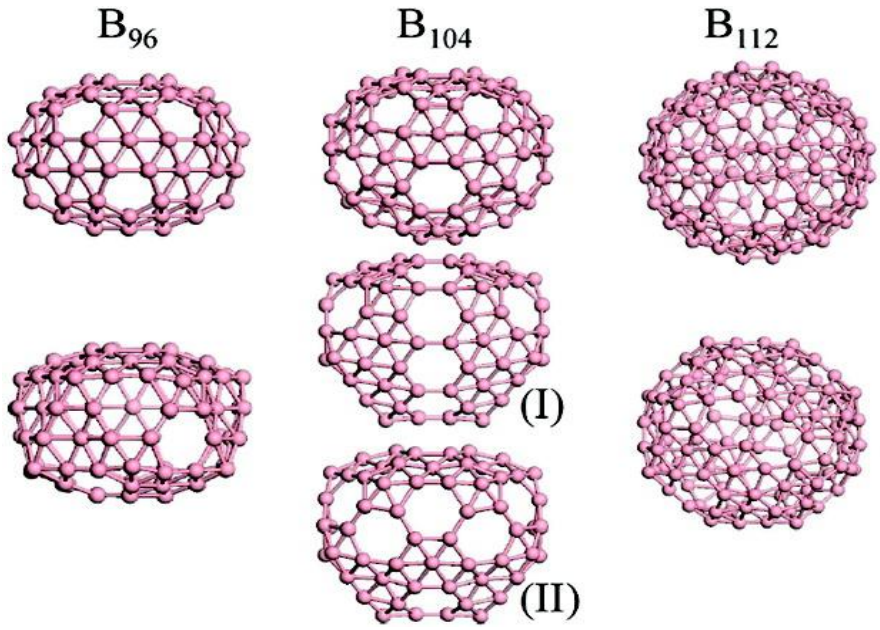

Figure 6.2. Optimized structures of snow-drop (top panel) and filled-pentagon (bottom panel) fullerenes of B_{96}, B_{104} (structure (I) and (II) 12 filled pentagon B_{104} isomers) , and B_{112}, respectively.

The B_{112} fullerene consists of 32 hexagons and 12 pentagons.[156] Among the 24 isomers, we consider the counterpart of the C_{84} ground-state structure with D_2 symmetry and an elliptical pillow shape.[156] The D_2 snow-drop B_{112} can be transformed to a C_2 filled-pentagon B_{112} through successful rotation of four snow-drops. An important criterion for structural stability is that the vibrational modes be all real.

We have performed vibrational analysis for all the above conformations. While the vibrational stability of the filled-pentagons: B_{80}, B_{96}, and B_{104} is confirmed, there exists two imaginary modes for snow-drop D_{6d}-B_{96}, in analogous to that in I_h-B_{80}.[155] The existence of imaginary frequency modes is attributed to the symmetry constraint of the calculation. A subsequent eigenmode following the analysis leads to a lower energy (~0.03 eV) and lower symmetry C_2-B_{96} conformation that has all real vibrational frequencies. We list in Table 6.1 the calculated binding energies, the gap between the highest-occupied-molecular-orbital (HOMO) and the lowest-unoccupied-molecular-orbital (LUMO), the symmetry of the fullerene, and the energy differences between the snow-drop and filled-pentagon models. As is readily observable from Table 6.1, the filled-pentagon fullerene is systematically lower in energy than the snow-drop counterpart. Furthermore, in contrast to the monotonic decrease of the snow-drop B_{80+8n} with the increase of n, the filled-pentagon B_{80+8n} shows the "magic" number of n = 2, corresponding to a filled-pentagon B_{96}. Closer scrutiny of the structure of the filled-pentagon B_{96} reveals that the enhanced stability of B_{96} correlates to the "isolated" empty hexagons or hexagon-pairs.

Table 6.1. Calculated Binding Energies (E_B^I Binding Energy of Snow-Drop Model, E_B^{II} Binding Energy of Filled-Pentagon Model in eV) Relative to Atomic Boron, HOMO-LUMO Gap (E_g in eV), the Energy Difference (ΔE in eV), and Symmetries (S) of Optimization of B_{80+8n} Fullerene Structures Using Local (BLYP) and Semi-Local (B3LYP) Approaches

n	Method	Structure	*S*	E_B^I(eV)	E_g(eV)	*S*	E_B^{II}(eV)	E_g(eV)	ΔE(eV)
0	BLYP	B_{80}	T_h-*A*	-406.82	0.94	T_h	-409.53	0.18	2.73
2	BLYP	B_{96}	C_2	-490.48	0.64	D_3	-494.86	0.27	4.38
3	BLYP	B_{104}	D_{3h}	-532.83	0.59	C_{2v} *(I)*	-534.44	0.27	1.61
3	BLYP					C_{2v} *(II)*	-536.05	0.20	3.22
0	B3LYP	B_{80}	T_h-*A*	-453.85	1.87	T_h	-458.13	0.86	4.29
2	B3LYP	B_{96}	C_2	-548.08	1.36	D_3	-553.48	0.93	5.40
3	B3LYP	B_{104}	D_{3h}	-595.81	1.22	C_{2v} *(I)*	-598.73	0.79	2.93
3	B3LYP					C_{2v} *(II)*	-598.93	0.91	3.12

Whereas the snow-drop B_{80+8n} gives rise to a large class of stable boron fullerenes, the filled-pentagon B_{80+8n} leads to structures with improved stability. For n = 0, the buckyball and volleyball B_{80} are the first members of the corresponding family. The α-BS is the $n \rightarrow \infty$ analogue for both models. The construction of filled-pentagon cages amounts to transforming a pair of neighboring pentagon rings to filled pentagons, accompanied by the generation of a pair of adjacent hollow hexagons. An optimal arrangement of those building blocks allows the tuning of the charge transfer, which gives rise to an attractive fluxional behavior and improves the stability. In all the cases, the improvement of energy is remarkable, ranging from 3.1 eV for B_{104} to 5.4 eV for B_{96}. The semi-local results are in good accordance with those of local density functional

approach results regarding the binding energy, while the correction to the HOMO-LUMO gap is substantial. As seen in Table 6.1, the rectified gap is about 0.7−0.9 eV for filled-pentagon fullerenes.

In conformity with the donor-acceptor hypothesis on α-BS,[55] electron transfers in the snow-drop B_{80+8n} can be classified as the capping atoms in the center of hexagonal pyramides as electron donors, while other atoms as acceptors.[63] For the filled-pentagon model, the capping atoms of hexagonal and hexagonal pyramids stand for electron donors.[66] Consequently, it is expected that uniformly distributed hollow hexagons are desired.[66] Shown in Figure 6.3 are the extracted charge density distributions of HOMO and LUMO for the snow-drop and filled-pentagon B_{96}, respectively. A distinctive feature of the charge density distribution of HOMO (LUMO) is evident by the increase of the π (π*) bonding in the filled-pentagon B_{96} as compared to that for the snow-drop B_{96}. This is attributed to the redistribution of the bonding and antibonding patterns related to the capping of the pentagon rings.[66] A few remarks are immediately in order. (i) Our results demonstrate that the filled pentagon model yields improvement in energy for a family of boron fullerenes, not limited to B_{80}. The energy improvement is primarily attributed to the migration of the capping atoms from filled hexagons to pentagons and the bonding arrangements associated with the changes in aromaticity. [66,153] (ii) The filled-pentagon fullerenes prefer evenly distributed hollow hexagons with connection to the donor-acceptor charge transfers. (iii) The stability of the filled-pentagon fullerenes is also manifested in the vibrational frequencies.

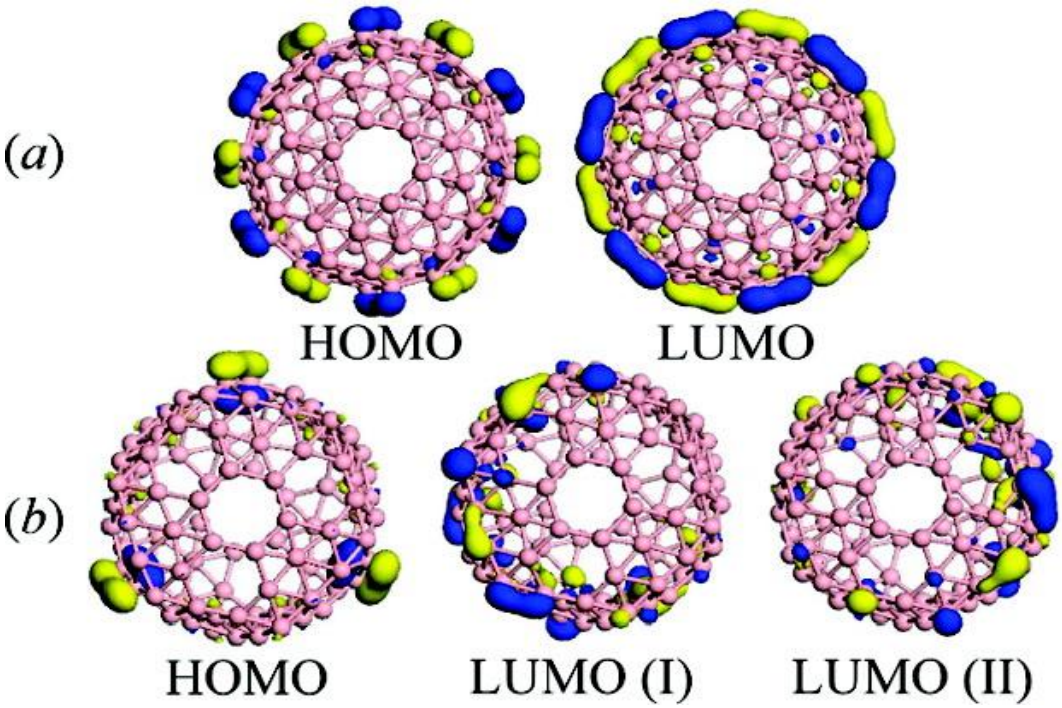

Figure 6.3. Isodensity surfaces (with an isovalue of 0.02 au) of HOMO and LUMO (LUMO(I) is the LUMO in B_{96} and LUMO(II) is the one level above the LUMO in B_{96}) for (a) the snow-drop and (b) filled-pentagon models of B_{96}, respectively. The positive and negative components are colored with blue and yellow, respectively.

We depict in Figure 6.4 the motion of the highest vibrational mode for B_{96}. The lowest vibrational modes are significantly softer than the counterparts of carbon fullerenes. [63,155] (iv) In contrast to the snow-drop building block, for filled-pentagon fullerenes, the basic unit is the adjacent pentagon-hexagon pyramids. (v) The main thrust of the present work is to assert that the filled-pentagon model is energetically preferred. To this end, we have systematically investigated a large set of snow-drop fullerenes and revealed the existence of a "magic" filled-pentagon B_{96}. Notwithstanding this, there are still a variety of boron fullerenes that remain unexplored. Our results, nevertheless, illustrate that the intriguing bonding pattern of boron keeps bringing surprises.

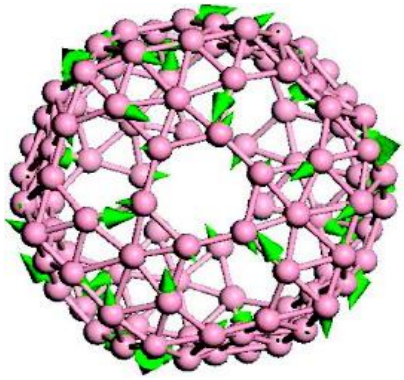

Figure 6.4. The motions of the infrared-active vibrational mode of 1972 $cm.^{-1}$

In summary, we have described a filled-pentagon constructing scheme for a large family of stable boron fullerenes. The improved stability of the filled-pentagon fullerenes over the snow-drop ones is confirmed by intensive first-principles simulations. A revised empirical electron counting rule indicates that a slightly increased electron counting per triangle is energetically preferred, which is useful for seeking out stable boron nanostructures. These results shed important light on the improved stability of boron fullerenes in connection with the aromaticity. We hope that these results can promote experimental synthesis of boron fullerenes along with future applications.

CHAPTER 7

DISPERSION-CORRECTION IN BORON BUCKYBALL AND NANOTUBES

7.0 Introduction

Density-functional theory (DFT) calculations by Barual, Pederson and Zope [155] indicated a vibrational instability of the I_h boron buckyball, and suggested a slightly puckered cage with tetrahedral (T_h) symmetry as shown in Figure 7.1.[155] Subsequent investigations [62,65,157-159] indicated that the atomic buckling is particularly sensitive to the basis set employed and the level of theory used in describing exchange-correlation effects. However, recent investigation by Szwacki and Tymczak [65] with the use of computationally intensive *ab*-initio calculations up to second order Moller-Plesset perturbation (MP2) theory reveals that the I_h boron buckyball is the lowest energy conformation owing to the crucial importance of correlation effects.[65]

A natural question arises as to what is missing in the preceding DFT approach. Because the location of the capping atoms is closely connected to the charge transfer,[65] a related question is whether the location impacts on the electronic properties. In view of the increasing amount of theoretical work devoted to boron nanomaterials, a clarification of this issue becomes timely and important. Herein, we report a dispersion-corrected DFT calculation study of boron buckyballs and the boron nanotubes. The dispersion-correction method, coupled to suitable DFT functional, has been demonstrated to account for

the long-range dispersion forces with remarkable accuracy. Our work shows that the inclusion of dispersion has a significant effect on the energies and geometries of boron fullerenes and nanotubes.

7.1 Method

We have employed first-principles calculations based on density-functional theory (DFT) and dispersion-corrected DFT approaches. For preselecting structural conformations and geometry optimizations, gradient-corrected Becke-Lee-Yang-Parr (BLYP) [136, 137] and Perdew-Burke-Ernzerhof (PBE)[81] parameterizations of the exchange correlation were used along with double numerical plus polarization (DNP) basis set as implemented in the DMol3 package.[72] The local density-functional calculation results were subsequently rectified through the inclusion of dispersion-correction effects.[82] The optimization of atomic positions was performed for all calculations, which proceeded until the forces were less than 0.01 eV/Å and the change in energy was less than 3×10^{-4} eV.

7.2 Results and Discussion

In order to gain insight into the structures of boron fullerenes, it is instructive to examine the B_{80} buckyball with I_h, T_h-A, and T_h-B symmetries as shown in Figure 7.1. All three structures of the B_{80} buckyball consist of 20 filled hexagons and 12 empty pentagons. The capping atoms are at the planar center of the hexagons for I_h-B_{80}. By contrast, for the T_h-A (T_h-B) conformation, there are 8 (12) capping atoms inwards while

the other 12 (8) are directed outwards. It is worth mentioning that there exist theoretical investigations of glassy behavior of the boron fullerenes. [66,160] The glassy behavior is manifested of the fact that the migration between B_6 (filled-pentagon) and B_7 (filled-hexagon) units[67] can lead to low energy conformations. [66,160] The migration of the capping atom from the center of a hexagon to the center of a pentagon, [66,163] along with the inclusion of a B_{12} core structure,[64] has been shown to yield improved structural stability. However, it is important to point out that those structures are separated from the buckyball conformations by large transition barriers.[66] For this reason, along with the fact that there exist no conclusive results available for the corresponding high-level quantum chemistry calculations, we are primarily interested in the correlation effects on the locally stable buckyball conformations.

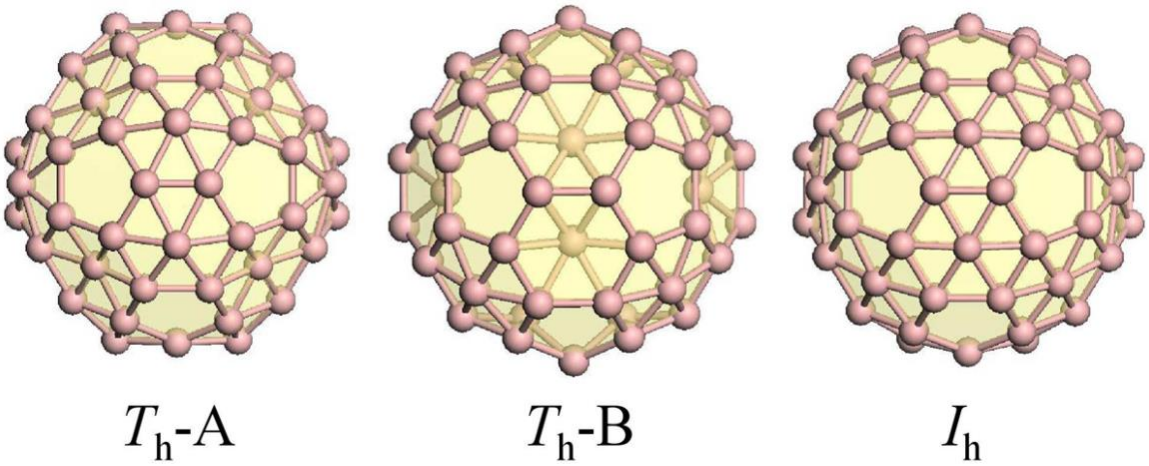

Figure 7.1. Ball-and-stick representations of the three optimized B_{80} structures of T_h-A, T_h-B, and I_h, respectively.

Nevertheless, the stability of the B_{80} buckyball structures can be readily characterized by the vibrational stability analysis and the accurate MP2 results can be used as a standard for validations.[65] Shown in Figure 7.1 are the three optimized buckyball structures (T_h-A and T_h-B using DFT, I_h using dispersion-corrected DFT). Consistent with previous DFT calculated results.[62,65,69,157-159] There exists imaginary vibrational frequencies for I_h-B_{80} using either BLYP or PBE exchange-correlation functions.

We illustrate in Figure 7.2 the corresponding eigenmodes of the two imaginary frequencies -57i and -19i (indicated by arrows in Figure 7.2) obtained from BLYP and PBE calculations, respectively. As can be seen from Figure 7.2, the eigenmode of the imaginary frequencies is predominantly attributed to the capping atoms, which indicates instability of the I_h structure against the lower symmetry ones. Following the imaginary eigenmodes, the slightly puckered T_h-A has a lower energy of 10.3 meV than the I_h counterpart, with all positive vibrational frequencies. T_h-B is also a locally stable conformation in that all the vibrational frequencies are positive, but the energy is slightly higher than that of T_h-A.[14] By way of contrast to the preceding DFT results,[62,65,69,157-159] with the inclusion of dispersion correction, all vibrational frequencies of I_h-B_{80} become positive. The energy order between I_h and T_h conformations is reversed as well: the I_h structure (-483.3381 eV) is 4.4 meV lower in energy than T_h-A (-483.3337 eV).

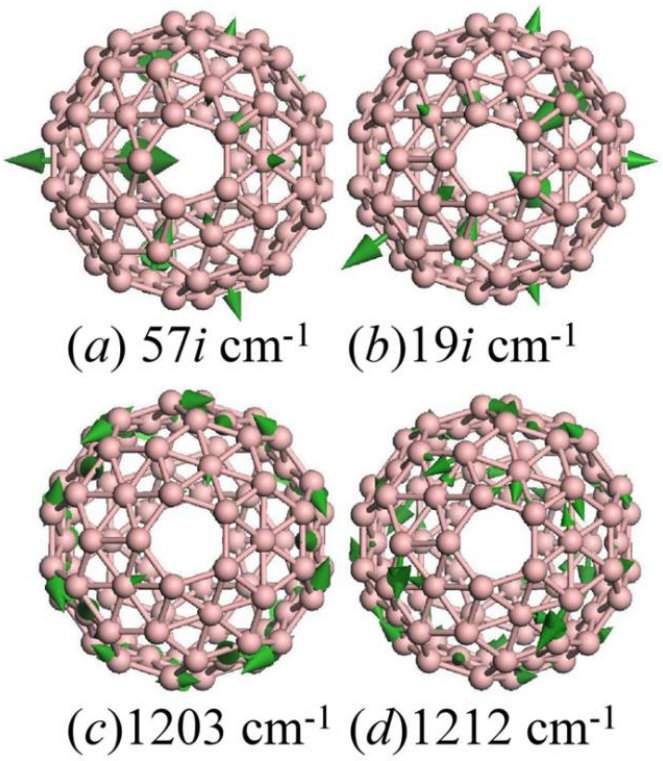

Figure 7.2. The eigenmotion of prototype unstable vibrational modes for B_{80}-I_h using (a) PBE and (b) BLYP, and the highest infrared (c) and Raman-active (d) modes using dispersion-corrected PBE.

Summarized in Figure 7.3 are the calculated vibrational density of state for I_h-B_{80}. The contribution from imaginary modes are indicated by the peaks below 0 (cm^{-1}). As can be readily observable from Figure 7.3, the inclusion of dispersion-correction removes the imaginary mode contributions from the PBE results. On the other hand, the vibrational DOS from BLYP is qualitatively different from those of PBE and dispersion-corrected PBE.

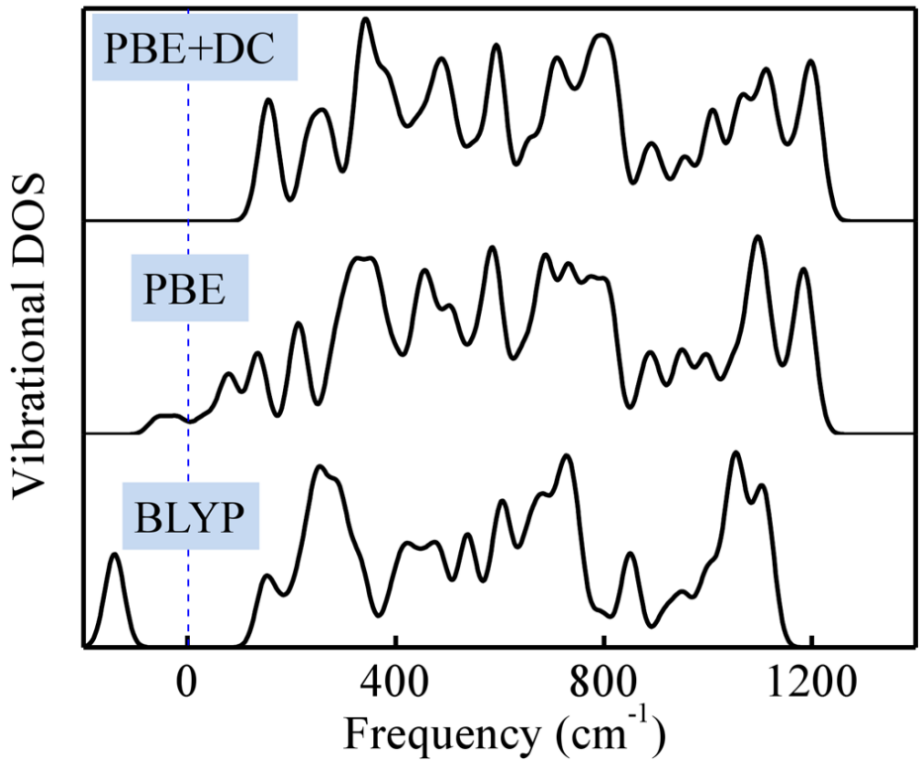

Figure 7.3. Calculated vibrational density of state (DOS) for I_h-B_{80} using BLYP, PBE, and dispersion-corrected PBE, respectively.

Our results are in very good agreement with those obtained from computational intensive MP2 calculations [65] in that the I_h-B_{80} is reinstalled as the lowest energy conformation among the buckyball structures. More importantly, our results clearly indicate that van der Waals (vdW) dispersion forces greatly impact on the geometry of capping atoms. As the attractive interaction between the capping atom and the six-member boron ring is of dipole-dipole character, dispersion correction to the DFT approach is essential to effectively capture the corresponding vdW contributions.

Encouraged by the dispersion-corrected DFT results for B_{80} buckyball, we are now in the position to examine the boron nanotubes.[161] The study of boron nanotubes is

very important in light of the experimental verification for the existence of boron nanotabular structures.[162] We constructed two prototype boron nanotubes (see Figure 7. 4) from wrapping the α-boron sheet following the nomenclature of carbon nanotubes: the zigzag (9,0) and armchair (7,7) boron nanotubes. The constructed tubes are periodic and thus allow one to calculate the band structures. It is worth mentioning that we have examined various two-dimensional sheet conformations using dispersion-corrected PBE and confirmed the lowest energy status of the α-boron sheet.

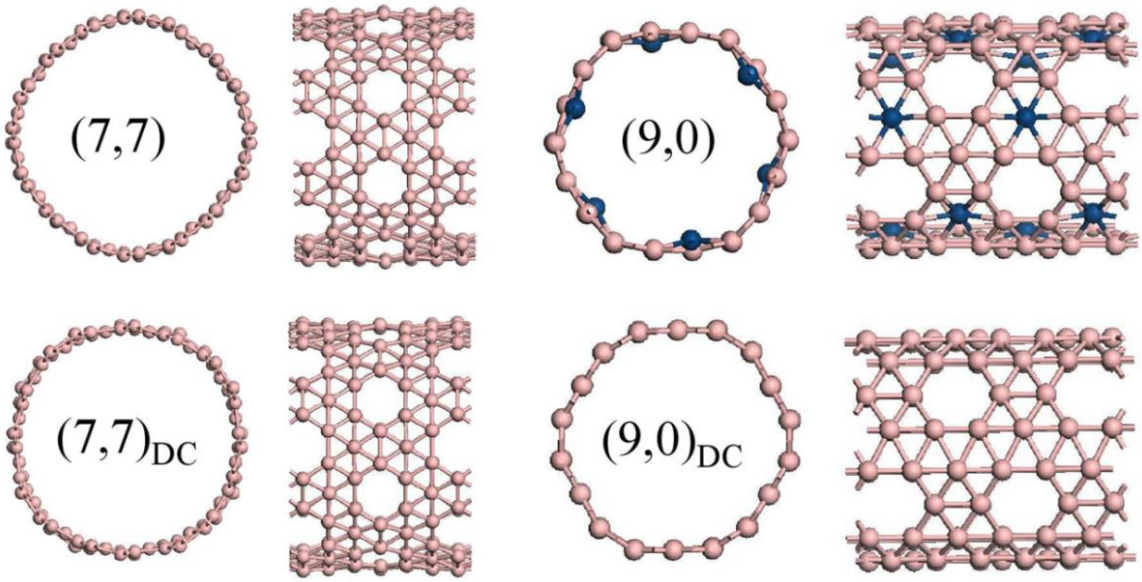

Figure 7.4. Top and side views of the optimized structures of boron nanotubes armchair (7,7) and zigzag (9,0) using DFT and dispersion-corrected DFT calculations.

Depicted in Figure 7. 4 are the optimized structures of the zigzag (9,0) and armchair (7,7) nanotubes using PBE and dispersion-corrected PBE, respectively. As seen from Figure 7.4, for the armchair (7,7) tube, the PBE calculation predicts a little bit elliptical shaped tube, while the dispersion-corrected PBE calculation yields a round

structure. For the zigzag (9,0), however, both types of calculations lead to a hexagonal tube with distinct locations of the capping atoms. The PBE optimized structure has puckered capping atoms (highlighted in Figure 7.4), while the dispersion-corrected PBE reasserts the non-puckered capping atom, which is located exactly in the center of the hexagon. Whereas the armchair boron nanotubes are free from the puckered capping atoms owing to the peculiar building units, the vdW interaction manifests itself in the distinct capping atom allocation for zigzag boron nanotubes with and without dispersion correction.

An important ramification of the dispersion correction is the change of charge-transfer behavior associated with the allocation of capping atoms. To further pursue this point, we show in Figure 7.5 the calculated band structures for the armchair (7,7) and zigzag (9,0) using PBE and dispersion-corrected PBE, respectively. As is readily observable from Figure 7.5 although the PBE and dispersion-corrected PBE optimized structures are quite different, the resultant electronic structures are quite similar. This is attributed to the fact that both conformations have analogous charge transfer behavior. For the zigzag (9,0) tube, the PBE calculation with puckered capping atoms results in a small gap semiconducting tube, which is to be contrasted with the dispersion-corrected PBE result of a metallic tube. This evidently demonstrates that the dispersion correction has a crucial impact on the electronic properties of the boron nanotubes.

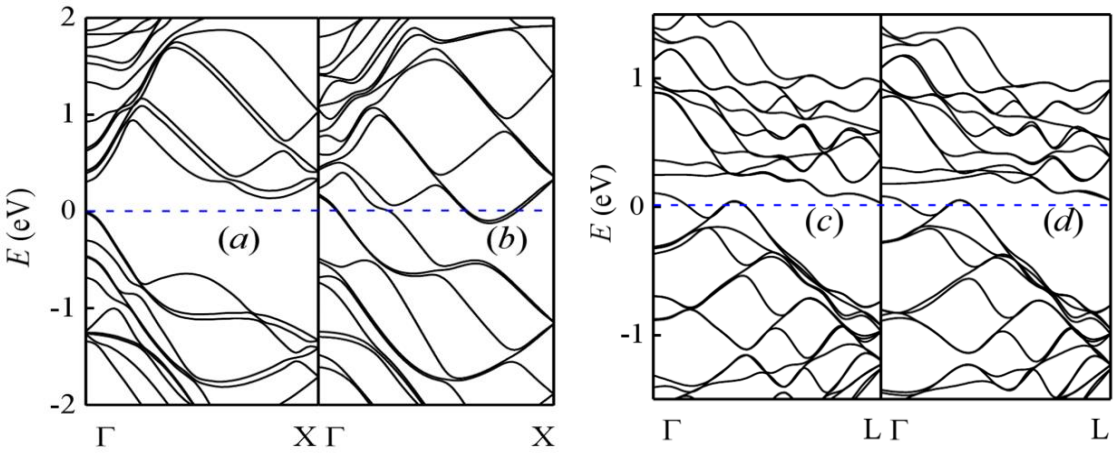

Figure 7.5. Calculated band structures of zigzag (left panel) and armchair (right panel) boron nanotubes using DFT (a and c) and dispersion-corrected DFT (b and d), respectively. X=¼=a and L=¼=b, where a = 5.04 Å and b = 8.37 Å, respectively.

A few remarks are immediately in order. (i) Both dispersion-corrected PBE[82] and B3LYP[154] affirm the vibrational stability of I_h-B_{80}. The dispersion-corrected semi-local B3LYP method[154] provides the rectification of the gap. However, the dispersion-corrected B3LYP for periodic systems is not yet available to us. Consequently, in the present work we focus on the dispersion-corrected PBE only. (ii) The dispersion correction is important in the relative energy order of boron fullerenes [66,160] and core-shell structures as well.[64] However, the energy ordering of the relevant structures depends also on the preceding level of exchange-correlation functions employed. Specifically, it is worth noting that the BLYP and PBE exchange-correlation functions lead to quite different energy ordering predictions, [60,160] which remain unsettled after the inclusion of dispersion corrections. A careful examination of the associated dispersion correction effects will be addressed in the future. (iii) The effect of dispersion correction in planar

structures, such as the α-boron sheet [55] and nanoribbons,[56] is dormant because the planar conformations are not apparently associated with the buckling of capping atoms.

In summary, we have presented calculated results based on long-range dispersion corrected DFT method [82] that is accurate and promising for accounting for the vdW contributions. The dispersion correlation effects are found to be essential for the correct description of the structure of hollow boron nanostructures. Our results validate the use of dispersion-corrected DFT for boron nanostructures, which provides useful means for studying boron nanomaterials.

CHAPTER 8

RELATIVE STABILITY OF BORON FULLERENES: A DISPERSION-CORRECTED DENSITY FUNCTIONAL STUDY

8.0 Introduction

A careful examination of the relative energy ordering of the B_{80} structures, reveals an unexpectedly strong dependence upon the exchange-correlation (XC) functional [57] utilized in the calculations. Specially, with the use of gradient-corrected Becke-Lee-Yang-Parr (BLYP) [72,82] method or the semi-local Becke-3-parameter-Lee-Yang-Parr (B3LYP) functional,[72] a volleyball-structured B_{80} with T_h symmetry is shown to be energetically lower than the core-shell structured B_{80} as well as the I_h-B_{80}.[77] In contrast, the energy ordering is reversed in favor of the core-shell structured B_{80} where employing the Perdew-Burke-Ernzerhof (PBE) functional.[154,163] The reversed energy is about 4-8 eV as large, depending on the basis sets used in the calculations.[68,77,159,162-164] In view of the increasing amount of theoretical works devoted to boron nanomaterials,[68,77,159,162-164] a clarification of this discrepancy becomes timely and important. Herein, we report on the results from a dispersion-corrected DFT calculation study of boron fullerenes. The dispersion-correction method, coupled to a suitable DFT functional, has been demonstrated to account for the long-range dispersion forces with remarkable accuracy.

Our work shows that the inclusion of dispersion has a significant effect on the energies and geometries of boron fullerenes.

8.1 Method

We have employed first-principles calculations based on DFT and dispersion corrected DFT approaches.[56,82] For preselecting structural conformations and geometry optimizations, BLYP and PBE parameterizations of exchange-correlation were used along with double numerical plus polarization (DNP) basis set as implemented in the DMol3 package.[72] The optimization of atomic positions was performed for all calculations, which proceeded until the forces were less than 0.01 eV/Å and the change in energy was less than 3×10^{-4} eV.

8.2 Results and Discussion

Depicted in Figure 8.1 are optimized conformations of various B_{80}, B_{96}, and B_{100} fullerenes.[165] These high symmetry structures represent the characteristic configurations discussed in previous studies.[60] Specifically, in addition to the I_h-B_{80}, the D_{5d}-B_{100} was identified as yet another low energy cage structure. By exploring the migration of capping atoms, [77,162-164] the $^{6P}B_{80}$ and $^{12P}B_{80}$ structures can be constructed, which are of D_{3d} and T_h symmetries, respectively. The former was recognized as the most stable structure for B_{80} fullerenes based on the PBE method[163] whereas the latter was extracted from BLYP and B3LYP optimizations.[77] The stability of the volleyball-shaped $^{12P}B_{80}$ promoted further investigations for larger fullerene sequences. [162,164] Consequently, the

filled-pentagon models of $^{12P}B_{96}$ and $^{12P}B_{100}$ were predicted to be energetically favorable over the empty pentagon counterparts. [162,164]

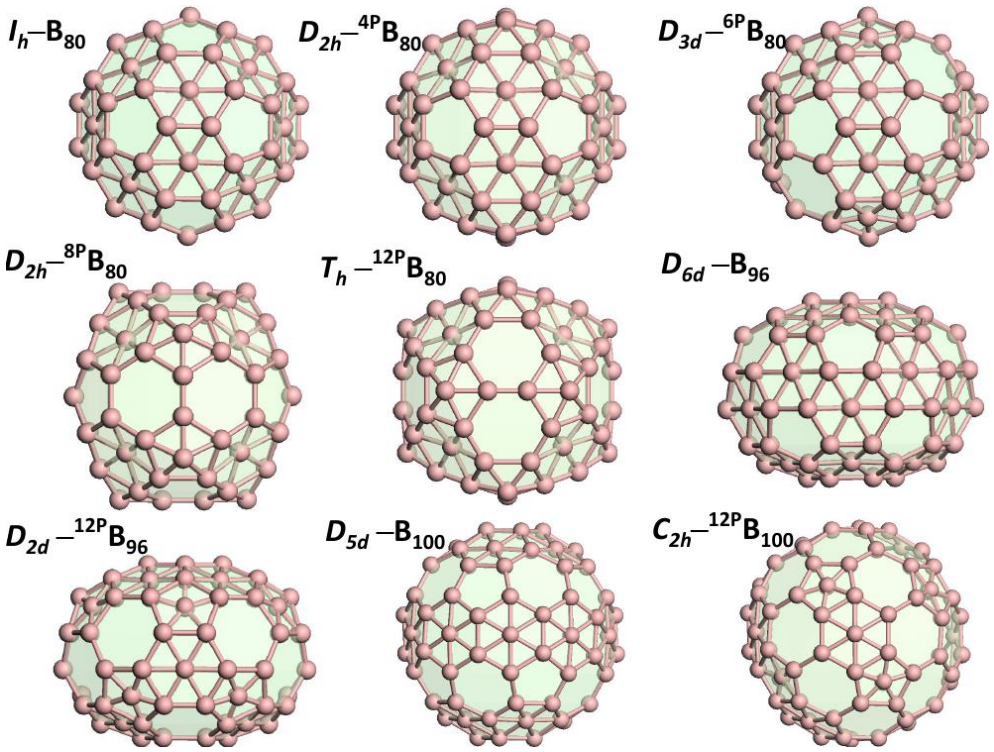

Figure 8.1. Optimized structures of B_{80} fullerenes with 0, 4 (4P), 6 (6P), 8 (8P), 12 (12P) filled pentagons, along with filled-hexagon (snow-drop) and filled-pentagon (12P) of B_{96} and B_{100}, respectively.

The building block for the I_h-B_{80} and the α-boron sheet is the so-called snow-drop pattern[164] that constitutes a central hexagonal pyramid surrounded by three hexagonal pyramids and three “hollows" (hollow pentagons or hexagons). [162,164] The migration of capping atoms from the centers of hexagons to those of pentagons can be facilitated by rotating the snow-drop unit; thereby including the pentagon pyramid in the building blocks. For instance, the $^{4P}B_{80}$, $^{8P}B_{80}$, and $^{12P}B_{80}$ can be constructed by rotating 2, 3, and 4

snow-drop blocks, which have D_{2d}, D_{2h}, and T_h symmetries, respectively. The hollow-pentagon; B_{96} is structurally similar to the C_{72} fullerene with 26 hexagons and 12 pentagons; 24 extra boron atoms are located at the center of 24 hexagons to stabilize the B_{72} cage. The hollow-pentagon B_{96} is of D_{6d} symmetry while the filled-pentagon B_{96} has D_{2d} symmetry. B_{100} is the counterpart of C_{80} with 30 hexagons, 12 pentagons, and 20 extra boron atoms at the center of 20 hexagons. Hollow and completely-filled-pentagon B_{100} has D_{5d} and C_{2h} symmetry, respectively. The resultant cages are locally stable structures in that all the vibrational frequencies are real.[55,59,62,65,155,157,158] However, the potential energy landscape for boron clusters is very complex, which depends on the XC used in various global minimum search approaches. [159,163]

We summarize in Figure 8.2 the relative energy ordering of those fullerenes, along with the core-shell structured B_{80}. [68,159] Energies per boron atom were extracted with the use of BLYP, PBE, and dispersion-corrected PBE. [159] respectively. As seen from Figure 8.2, within the BLYP scheme, the completely-filled-pentagon conformations are lower in energy than the hollow-pentagon counterparts, in conformity with the previous results concerning B_{80}, B_{96}, and B_{100}. [165] It is worth noting that the inclusion of semi-local functional in the B3LYP approach [77,162] rectifies the gap between the LUMO and the highest-occupied molecular orbital (HOMO), while the relative energy order remains unchanged. [162]

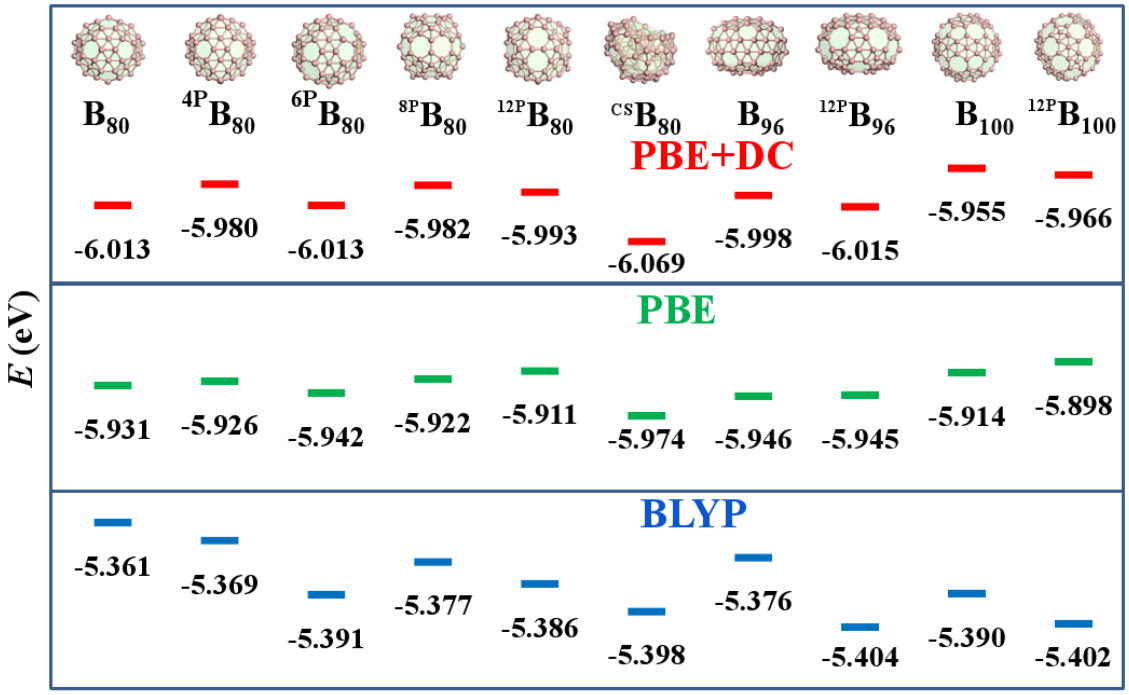

Figure 8.2. Calculated energies per boron atom E(eV) for the B_{80}, B_{96}, and B_{100} isomers using BLYP (bottom panel), PBE (middle panel), and dispersion-corrected PBE (top panel), respectively.

In contrast, within the PBE scheme, the completely filled-pentagon conformations are no longer lower in energy than the hollow-pentagon counterparts. [37] Moreover, the Ih-B_{80} buckyball is energetically favored over B_{100}. With the exception of a partly-filled-pentagon $^{6P}B_{80}$ that represent the lowest energy isomer for the B_{80} fullerenes, the relative energy ordering concerning the core-shell structured B_{80}, completely-filled-pentagon vs. hollow-pentagons, B_{80} vs. B_{100}, is in sharp contrast to BLYP (B3LYP) redictions.[77,162,164,165] For instance, comparing the energy between the core-shell structured B_{80} with respect to the volleyball-shaped $^{12P}B_{80}$, the relative energy difference is -0.44, 4.62, 4.71 eV for BLYP, PBE, and dispersion-corrected PBE, respectively. A careful examination of the extracted energies for optimized conformations listed in

Figure 8.2 reveals that the BLYP (B3LYP) and PBE (PBE0 or revPBE) approaches yield distinct energy orderings, and the differences between the two types of schemes can be as large as ~ 0.6 eV.

Such a discrepancy raises serious concerns on the reliability regarding the predicted stability of boron fullerenes and core-shell structured B_{80}. A natural question arises as to whether one scheme is more trustworthy over the other. In this regard, it is worth noting that there is a strong dependence of the relative energy order on the XC functional. In view of the fact that both BLYP and PBE are GGA based DFT methods, the XC effects on the relative energy ordering are important even in these cases. In this regard, the following remarks are appropriate: (i) If the polarization function is not included in the calculation, the completely-filled-pentagon conformations are still energetically favored over the hollow-pentagon counterparts with the use of PBE functional. This is the case for results extracted from earlier versions of the GPU accelerated quantum chemistry code TeraChem [166] in which the polarization function was not available in the basis sets. However, the energy ordering may be reversed after the inclusion of polarization functions. (ii) There is particular interest with regard to the comparison of the relative stability between the core shell structure and the cage conformations with the same number of boron atoms. [68,77,159,162-164] Within the PBE or dispersion-corrected PBE, the core-shell structured $B_{12}@B_{68}$ becomes the lowest energy conformation for B_{80}. This is in sharp contrast to the BLYP result, which predicts a volleyball structured B_{80}, lower in energy than both the buckyball B_{80} and the core-shell structured $^{CS}B_{80}$ (I). [159] Moreover, a B_{100} is the lowest BLYP (B3LYP) predicted energy

structure among the low-energy conformations. [165] (iii) Although the energy difference between I_h and T_h-A of the B_{80} buckyball is merely about 4.4 meV, the relative stability has been intensively discussed among the quantum chemistry community, particularly with regard to the vibrational stability. [62,162] While the dispersion correction is important in resolving this issue, the large energy switching of about 8 eV among various B_{80} conformations is far more dramatic. This demonstrates the intricate feature of bonding on the exchange-correlation functional used. (iv) A comparison between the BLYP and B3LYP semi-local calculations shows that there is no qualitative change in the energy ordering. In other words, BLYP and B3LYP yield the same energy ordering. PBE and PBE0 also yield the same energy ordering. [162] (v) During preparation of this thesis, we became aware of a related theoretical study by Li and co-workers on boron clusters; [167] they obtained similar trends as ours for discrepancies between the BLYP and PBE XC functional. While the study is validated through the comparison with small boron clusters, our study here is focused on the effect of dispersion corrections.

We are now in a position to discuss the effect of dispersion correction on the relative energy ordering of those boron fullerenes. It is worth pointing out that while there are distinct energy orderings for boron fullerenes, the dispersion-corrected B3LYP and dispersion-corrected PBE results yield the same energy trend. The dispersion correction to the BLYP (or B3LYP) is much larger than the dispersion-corrected PBE (or PBE0) counterparts (see Table 8.1). However, the dispersion correction to PBE is not negligible, as the relative energy differences can be as large as ~0.2 eV with the inclusion of dispersion forces. As seen from Figure 8.2, the dispersion-corrected PBE results

confirm that the core-shell structured B_{80} is lower in energy than the B_{80} fullerenes. Semi-local calculations based on dispersion-corrected B3LYP (B3LYP-D) and PBE0 (PBE-D) using TeraChem [167] also confirms that the two core-shell structured B_{80}, $^{CS}B_{80}$(I)16 and $^{CS}B_{80}$(II),17 are lower in energy than the B_{80} fullerene counterparts. On the other hand, if we focus on the various boron fullerenes, a filled-pentagon $^{12P}B_{96}$ is an energetically preferred structure. [162,164] Since $^{6P}B_{80}$ is the lowest energy B_{80} fullerene confirmation, [163] we have constructed the $^{6P}B_{96}$ counterpart that has C_{6V} symmetry by moving six centered atoms from the hexagons to six empty pentagons. Analogous to $^{6P}B_{80}$ that has 6 isolated empty pentagon-hexagon pairs, $^{6P}B_{96}$ also contains 6 fused empty hexagon-pentagon pairs along with two isolated extra empty hexagons. The extracted binding energy of the optimized $^{6P}B_{96}$ structure with BLYP, PBE and dispersion-corrected PBE is less favorable than either the empty-pentagon $^{0P}B_{96}$ or filled-pentagon $^{12P}B_{96}$, by 1.51 and 3.22 eV, respectively. This implies that the aromaticity for models of B_{80} with empty-pentagon (buckyball),[52] filled-pentagon with fused empty hexagon pairs (volleyball), [158] and the partially filled pentagon with fused empty pentagon-hexagon pairs (baseball),[164,162] changes with the inclusion of empty hexagons for large fullerenes.

Table 8.1. Calculated Binding Energies E_B (Relative to Atomic Boron), HOMO-LUMO Gap (E_g) of Optimized Isomers of B_{80} and B_{96} Fullerenes Using Semi-ocal (B3LYP), Dispersion-Corrected B3LYP (B3LYP-D), and Dispersion Corrected PBE0 (PBE-D) Respectively. The Calculation was Based on TeraChem and 6-311G* Basis Sets

Structure	$\boldsymbol{E_B}$ (eV)			$\boldsymbol{E_g}$ (eV)		
	B3LYP	**B3LYP-D**	**PBE-D**	**B3LYP**	**B3LYP-D**	**PBE-D**
B_{80}	-5.936	-6.091	-6.631	1.83	1.87	1.87
$^{6P}B_{80}$	-5.960	-6.111	-6.635	0.78	0.80	0.76
$^{12P}B_{80}$	-5.956	-6.100	-6.610	0.85	0.86	1.02
$^{CS}B_{80}(I)$[18]	-5.951	-6.145	-6.690	1.08	1.10	1.28
$^{CS}B_{80}(II)$[19]	-5.966	-6.159	-6.702	0.95	0.95	1.11

An important criterion for structural stability is that all vibrational frequencies are all real. [56,168] We have performed vibrational analysis for all the above-discussed conformations. We illustrate in Figure 8.3 the calculated vibrational spectra for the I_h-B_{80}, D_{3d}-$^{6P}B_{80}$, and core-shell structured B_{80} ($^{CS}B_{80}$), respectively. It is readily observed that the core-shell structured B_{80} virtually has no feature as the structure is of low symmetry. By contrast, the high symmetry structures of B_{80} exhibit distinct peaks.

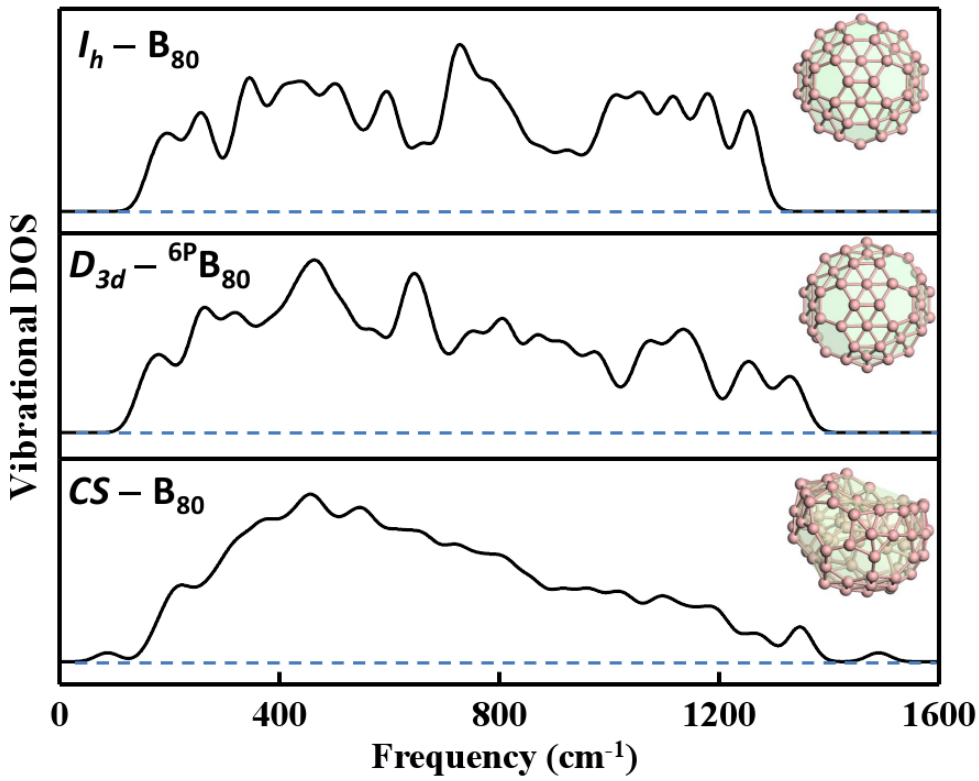

Figure 8.3. Vibrational density of states calculated by means of dispersion-corrected PBE calculations for the I_h-B_{80} (top panel), D_{3d}-$^{6P}B_{80}$ (middle panel), and core-shell structured ^{CS}-B_{80} (bottom panel).

In summary, we have examined various high symmetry cage-structured boron fullerenes and core-shell structured nanoclusters. Our results are in conformity with previous studies with regard to the relative stability, but reveal a strong dependence on the XC functional employed in the calculations. A detailed comparison with and without the inclusion of dispersion corrections indicates that the dispersion correction becomes crucial, particularly for BLYP or B3LYP type of XC functional.[167] It is worth remarking that although for PBE or PBE0 the inclusion of dispersion correction yields nearly the same energy ordering (with only a few exceptions) as that obtained with the

preceding DFT calculation, the dispersion correction plays an important role in the quantitative energy ordering as well as in the vibrational stability. Our systematic investigation of the relative stability of boron fullerene confirmations demonstrates that the dispersion-correction forces are particularly important for highly aromatic or anti-aromatic systems. [56,167,168]

CHAPTER 9

CONCLUSION

In this dissertation, we have studied the structural and electronic properties of carbon-based and boron-based nano materials. We have studied the electronic characteristics of non-covalently functionalized graphene with HHTP-PBBA and NiPc-PBBA. The noncovalent attachment of these COFs preserves the sp^2 hybridization network of graphene. The planar COF networks self-assemble on graphene via the graphene-mediated complementary orbital interactions between the filled orbital of the center molecule and the empty orbital of the linker. The hybridization-induced charge delocalization of the charge donor and acceptor COF components results in a stable COF−graphene hybrid.

Structural and electronic characteristics of covalently functionalized semi-fluorinated graphene conformations were investigated. While the relative stability of various patterns follows the same energy order as the corresponding hydrogenated graphene counterparts, the partial ionic character of the C–F bond results in the orbital resonance of C–F σ-bonds with an sp^2 network of graphene. Orbital resonance stabilizes the stirrup conformation via the gauche effect. Orbital resonance leads to additional delocalized electrons in the FEG. As a result, effective tailoring of electronic and ferromagnetic properties of FEG needs an improved understanding of the associated orbital resonance effect.

Water soluble polymer P m PE p PE in which the *meta*- phenylene unit introduces a bent angle along the polymer backbone to facilitate the helical conformation. In aqueous, the polymer is found to disperse SWNTs with good selectivity toward the (6,5) and some selectivity toward (8,3) SWNTs which have the small diameters (d = 0.757 and 0.782 nm, respectively). The intriguing selectivity is partly due to the helical conformation of polymer backbone, whose cavity size could act as pre-sort mechanism to select the tubes of small diameters. The SWNTs of similar diameters are further differentiated by interaction with the local phenyleneethynylene (PE) chromophores, whose assembly is guided by the helical conformation and assisted by the low rotational barrier of C≡C bonds. Selective dispersion of small diameter (6,5) SWNT illustrates that the synergistic effect of the quantum registry and the helical conformation cavity can be an effective tool to aid the SWNTs sorting. Clearly, the P m PE p PE 3 is superior to its vinylene analogue polymer 1 in terms of selective SWNT dispersion, as the paraphenylenevinylene unit in polymer 1 does not align parallel to SWNT surface for π – π interaction. Integration of a size control mechanism (via polymer conformation here) with a suitable molecular interaction, therefore, could offer a promising strategy to achieve the isolation of a specific SWNT.

We performed a systematic modeling study that provides crucial insights into the selective interactions between SWCNTs and π-conjugated polymers. Since the diameter and chirality of the nanotubes dictate their mechanical properties as well as electrical conductivity, an in-depth understanding of the interactions between conjugated polymers and carbon nanotubes is of great importance. The study reveals that the *cis*- and *trans*-

vinylene bond geometry plays an important role to influence the orientation of the polymer's phenyl rings toward SWCNT. When PmPV is wrapping around an SWCNT, the optimum polymer-SWCNT interaction appears to be dependent on the molecular ability to adjust the orientation of phenyl ring, which is essential for achieving optimum interaction via adopting Y- or PD-interactions. The approach thus shed light on the details of intermolecular interaction between PmPV and SWCNT, which can be employed to the novel π-conjugated polymers. Investigation of relevant structural and electronic properties is important for the development of nanotube based nanoelectronics and nanostructured composites.

The boron fullerenes counterparts of carbon nanotubes and fullerenes are under intensive experimental exploration. On the other hand, as we discussed in this thesis, an accurate characterization of the relative stability of this type of nano systems depends crucially on the inclusion of dispersive forces in the calculations. To achieve this goal, a semi-empirical method to incorporate dispersion correction was employed. Our results based on intensive search of pentagon-filled or hexagon-filled models along with the mixtures provide important insight into the intriguing nature of chemical bonding in boron fullerenes.

A careful examination of the dispersion correction effect leads to the conclusion that the semi-empirical inclusion of long range van der Waals interactions is efficient in reproducing results based on highly accurate but computationally very demanding methods. As the boron nanomaterials are relevant to hydrogen storage novel structures, our investigation provides useful guidelines for future experimental studies.

REFERENCES

1. Geim, A. K.; Novoselov, K. S. The Rise of Graphene. *Nat. Mater*. **2007**, *6*, 183.

2. Rao, C. N. R.; Sood, A. K.; Subrahmanyam, K. S.; Govindaraj, A. Graphene: The New Two-Dimensional Nanomaterial. *Angew. Chem., Int. Ed.* **2009**, *48*, 7752.

3. Castro Neto, A. H.; Guinea, F.; Peres, N. M. R.; Novoselov, K. S.; Geim, A. K. The Electronic Properties of Graphene. *Rev. Mod. Phys.* **2009**, *81*, 109.

4. Allen, M. J.; Tung, V. C.; Kaner, R. B. Honeycomb Carbon: A Review of Graphene. *Chem. Rev.* **2009**, *110*, 132.

5. Oostinga, J. B.; Heersche, H. B.; Liu, X.; Morpurgo, A. F.; Vandersypen, L. M. K. Gate-Induced Insulating State in Bilayer Graphene Devices. *Nat. Mater.* **2008**, *7*, 151.

6. Reuven, D.; Li, H.; Harruna, I.; Wang, X.-Q. Self-Assembly of Metallopolymer Guided by Graphene Nanoribbons. *J. Mater. Chem.* **2012**, *22*, 15689.

7. Reuven, D. G.; Suggs, K.; Williams, M. D.; Wang, X.-Q. Self-Assembly of Biofunctional Polymer on Graphene Nanoribbons. *ACS Nano* **2012**, *6*, 1011.

8. Samarakoon, D. K.; Wang, X.-Q. Twist-Boat Conformation in Graphene Oxides. *Nanoscale* **2011**, *3*, 192.

9. Samarakoon, D. K.; Chen, Z.; Nicolas, C.; Wang, X.-Q. Structural and Electronic Properties of Fluorographene. *Small* **2011**, *7*, 965.

10. Zboril, R.; Karlicky, F.; Bourlinos, A. B.; Steriotis, T. A.; Stubos, A. K.; Georgakilas, V.; Safarova, K.; Jancik, D.; Trapalis, C.; Otyepka, M. Graphene Fluoride: A Stable Stoichiometric Graphene Derivative and its Chemical Conversion to Graphene. *Small* **2010**, *6*, 2885.

11. Leenaerts, O.; Peelaers, H.; Hernández-Nieves, A. D.; Partoens, B.; Peeters, F. M. First-Principles Investigation of Graphene Fluoride and Graphane. *Phys. Rev. B* **2010**, *82*, 195436.

12. Liu, L.-H.; Lerner, M. M.; Yan, M. Derivitization of Pristine Graphene with Well-Defined Chemical Functionalities. *Nano Lett.* **2010**, *10*, 3754.

13. Liu, L.-H.; Yan, M. Simple Method for the Covalent Immobilization of Graphene. *Nano Lett.* **2009**, *9*, 3375.

14. Sofo, J. O.; Chaudhari, A. S.; Barber, G. D. Graphane: A TwoDimensional Hydrocarbon. *Phys. Rev. B* **2007**, *75*, 153401.

15. Elias, D. C.; Nair, R. R.; Mohiuddin, T. M. G.; Morozov, S. V.; Blake, P.; Halsall, M. P.; Ferrari, A. C.; Boukhvalov, D. W.; Katsnelson, M. I.; Geim, A. K.; et al. Control of Graphene's Properties by Reversible Hydrogenation: Evidence for Graphane. *Science* **2009**, *323*, 610.

16. Xu, H.; Suslick, K. S. Sonochemical Preparation of Functionalized Graphenes. *J. Am. Chem. Soc.* **2011**, *33*, 9148.

17. Zhang, J.; Jiang, J.; Zhao, X. S. Synthesis and Capacitive Properties of Manganese Oxide Nanosheets Dispersed on Functionalized Graphene Sheets. *J. Phys. Chem. C* **2011**, *115*, 6448.

18. Ogunro, O. O.; Karunwi, K.; Khan, I. M.; Wang, X.-Q. Chiral Asymmetry of Helical Polymer Nanowires. *J. Phys. Chem. Lett.* **2010**, *1*, 704.

19. Sun, Z.; Kohama, S.-I.; Zhang, Z.; Lomeda, J. R.; Tour, J. M. Soluble Graphene through Edge-Selective Functionalization. *Nano Res.* **2010**, *3*, 117.

20. Liu, L.-H.; Yan, M. Functionalization of Pristine Graphene with Perfluorophenyl Azides. *J. Mater. Chem.* **2011**, *21*, 3273.

21. Suggs, K.; Reuven, D.; Wang, X.-Q. Electronic Properties of Cycloaddition Functionalized Graphene. *J. Phys. Chem.* **2011**, *115*, 3313.

22. Cardenas-Jiron, G. I.; Leon-Plata, P.; Cortes-Arriagada, D.; Seminario, J. M. Electrical Characteristics of Cobalt Phthalocyanine Complexes Adsorbed on Graphene. *J. Phys. Chem. C* **2011**, *115*, 16052.

23. Malig, J.; Jux, N.; Kiessling, D.; Cid, J.-J.; Vázquez, P.; Torres, T.; Guldi, D. M. Towards Tunable Graphene/Phthalocyanine−PPV Hybrid Systems. *Angew. Chem., Int. Ed.* **2011**, *50*, 3561.

24. Li, N.; Zhu, M.; Qu, M.; Gao, X.; Li, X.; Zhang, W.; Zhang, J.; Ye, J. Iron-Tetrasulfophthalocyanine Functionalized Graphene Nanosheets: Attractive Hybrid Nanomaterials for Electrocatalysis and Electroanalysis. *J. Electroanal. Chem.* **2010**, *651*, 12.

25. Sandanayaka, A. S. D.; Subbaiyan, N. K.; Das, S. K.; Chitta, R.; Maligaspe, E.; Hasobe, T.; Ito, O.; D'Souza, F. Diameter-Sorted SWCNT−Porphyrin and SWCNT−Phthalocyanine Conjugates for Light-Energy Harvesting. *Chem. Phys. Chem.* **2011**, *12*, 2266.

26. An, X.; Simmons, T.; Shah, R.; Wolfe, C.; Lewis, K. M.; Washington, M.; Nayak, S. K.; Talapatra, S.; Kar, S. Stable Aqueous Dispersions of Noncovalently Functionalized Graphene from Graphite and Their Multifunctional High-Performance Applications. *Nano Lett.* **2010**, *10*, 4295.

27. Kodali, V. K.; Scrimgeour, J.; Kim, S.; Hankinson, J. H.; Carroll, K. M.; de Heer, W. A.; Berger, C.; Curtis, J. E. Nonperturbative Chemical Modification of Graphene for Protein Micropatterning. *Langmuir* **2011**, *27*, 863.

28. Liu, J.; Tao, L.; Yang, W.; Li, D.; Boyer, C.; Wuhrer, R.; Braet, F.; Davis, T. P. Synthesis, Characterization, and Multilayer Assembly of pH Sensitive Graphene Polymer Nanocomposites. *Langmuir* **2010**, *26*, 10068.

29. Bottari, G.; Suanzes, J. A.; Trukhina, O.; Torres, T. Phthalocyanine−Carbon Nanostructure Materials Assembled through Supramolecular Interactions. *J. Phys. Chem. Lett.* **2011**, *2*, 905.

30. Colson, J. W.; Woll, A. R.; Mukherjee, A.; Levendorf, M. P.; Spitler, E. L.; Shields, V. B.; Spencer, M. G.; Park, J.; Dichtel, W. R. Oriented 2D Covalent Organic Framework Thin Films on SingleLayer Graphene. *Science* **2011**, *332*, 228.

31. Côté, A. P.; Benin, A. I.; Ockwig, N. W.; O'Keeffe, M.; Matzger, A. J.; Yaghi, O. M. Porous, Crystalline, Covalent Organic Frameworks. *Science* **2005**, *310*, 1166.

32. Han, S. S.; Furukawa, H.; Yaghi, O. M.; Goddard, W. A. Covalent Organic Frameworks as Exceptional Hydrogen Storage Materials. *J. Am. Chem. Soc.* **2008**, *130*, 11580.

33. Lanni, L. M.; Tilford, R. W.; Bharathy, M.; Lavigne, J. J. Enhanced Hydrolytic Stability of Self-Assembling Alkylated TwoDimensional Covalent Organic Frameworks. *J. Am. Chem. Soc.* **2011**, *133*, 13975.

34. Uribe-Romo, F. J.; Doonan, C. J.; Furukawa, H.; Oisaki, K.; Yaghi, O. M. Crystalline Covalent Organic Frameworks with Hydrazone Linkages. *J. Am. Chem. Soc.* **2011**, *133*, 11478.

35. Sluiter, M. H. F.; Kawazoe, Y. Cluster expansion method for adsorption: Application to hydrogen chemisorption on grapheme. *Phys. Rev. B* **2003**, 68, 085410.

36. Nair, R.; Ren, W.; Jalil, R.; Riaz, I.; Kravets, V.; Britnell, L.; Blake, P.; Schedin, F.; Mayorov, A.; Yuan, S.; Katsnelson, M.; Cheng, H.; Strupinski, W.; Bulusheva, L.; Okotrub, A.; Grigorieva, I.; Grigorenko, A.; Novoselov, K.; Geim, A.K. Fluorographene: A Two-Dimensional Counterpart of Teflon. *Small* **2010**, 6, 2877.

37. Neek-Amal, M.; Peeters, F. M. Lattice thermal properties of graphane: Thermal contraction, roughness, and heat capacity. *Phys. Rev. B: Condens. Matter Mater. Phys*. **2011**, 83, 235437.

38. Costamagna, S.; Neek-Amal, M.; Los, J. H.; Peeters, F. M. Thermal rippling behavior of graphane. *Phys. Rev. B: Condens. Matter Mater. Phys*. **2012**, 86, 041408.

39. Boukhavalov, D. W.; Katsnelson, M. I.; Lichtendtein, A. I. Hydrogen on graphene: Electronic structure, total energy, structural distortions and magnetism from first-principles calculations. *Phys. Rev. B: Condens. Matter Mater. Phys*. **2008**, 77, 035427.

40. Samarakoon, D. K.; Wang, X.-Q. Tunable Band Gap in Hydrogenated Bilayer Graphene. *ACS Nano* **2010**, 4, 4126.

41. Withers, F.; Russo, S.; Dubois, M.; Craciun, M. F. Tuning the electronic transport properties of graphene through functionalisation with fluorine. *Nanoscale Res. Lett.* **2011**, 6, 526.

42. Emtsev, K. V.; Bostwick, A.; Horn, K.; Jobst, J.; Kellogg, G. L.; Ley, L.; McChesney, J. L.; Ohta, T.; Reshanov, S. A.; Ro ¨hrl, J.; Rotenberg, E.; Schmid, A. K.; Waldmann, D.; Weber, H. B.; Seyller, T. Towards wafer-size graphene layers by atmospheric pressure graphitization of silicon carbide. *Nat. Mater.* **2009**, 8, 203.

43. Sivek, J.; Leenaerts, O.; Partoens, B.; Peeters, F. M. *J. Phys. Chem*. C **2012**, 116, 19240.

44. Zhang, H.; Bekyarova, E.; Huang, J.W.; Zhao, Z.; Bao, W.; Wang, F.; Haddon, R. C.; Lau, C. N. Aryl Functionalization as a Route to Band Gap Engineering in Single Layer Graphene Devices. *Nano Lett*. **2011**, 11, 4047.

45. Hong, J.; Bekyarova, E.; Liang, P.; de Heer, W. A.; Haddon, R. C.; Khizroev, S. Room-temperature Magnetic Ordering in Functionalized Graphene. *Sci. Rep*. **2012**, 2, 624.

46. Iijima S.; Helical Microtubules of Graphitic Carbon, *Nature* **1991**, 354, 56.

47. Iijima, S. Direct observation of the tetrahedral bonding in graphitized carbon black by high resolution electron microscopy. *Journal of Crystal Growth* **1980**, 50, 675.

48. Treacy, M. M. J.; Ebbesen, T. W.; Gibson, J. M. Exceptionally high Young's modulus observed for individual carbon nanotubes. *Nature* **1996**, 381, 678.

49. White, C. T.; Todorov, T. N. T. Carbon nanotubes as long ballistic conductors. *Nature* **1998**, 398, 240.

50. Ouyang, M.; Huang, J.-L.; Cheung, C. L.; Lieber, C. M. Energy Gaps in "Metallic"Single-Walled Carbon Nanotubes. *Science* **2001**, 292, 702.

51. Meyyappan, M. Carbon Nanotubes: Science and Applications, *CRC Press, New York* **2005**.

52. Kroto, H.; Heath, J.; O'Brien, S.; Curl, R.; Smalley, R. C_{60}: Buckminsterfullerene. *Nature* **1985**, 318, 162.

53. Szwacki, N. G.; Sadrzadeh, A.; Yakobson, B. I. B_{80} Fullerene: An Ab Initio Prediction of Geometry, Stability, and Electronic Structure. *Phys. Rev. Lett*. **2007**, 98, 166804.

54. Huang, W.; Sergeeva, A. P.; Zhai, H. J.; Averkiev, B. B.; Wang, L. S.; Boldyrev, A. I. A Concentric Planar Doubly π-Aromatic B−19 Cluster. *Nature Chem*. **2010**, 2, 202.

55. Tang, H.; Ismail-Beigi, S. Novel Precursors for Boron Nanotubes: The Competition of Two-Center and Three-Center Bonding in Boron Sheets. *Phys. Rev. Lett.* **2007**, 99, 115501.

56. Saxena, S.; Tyson, T. A. Insights on the Atomic and Electronic Structure of Boron Nanoribbons. *Phys. Rev. Lett.* **2010**, 104, 245502.

57. Kiran, B.; Bulusu, S.; Zhai, H.-J.; Yoo, S.; Zeng, X.-C.; Wang, L. S. Planar-to-Tubular Structural Transition in Boron Clusters: B20 as the Embryo of Single-Walled Boron Nanotubes. *Proc. Natl. Acad. Sci. U.S.A.* **2005**, 102, 961.

58. Zhai, H. J.; Kiran, B.; Li, J.; Wang, L. S. Hydrocarbon Analogues of Boron Clusters-Planarity, Aromaticity and Antiaromaticity. *Nat. Mater.* **2003**, 2, 827.

59. Li, J. L.; Yang, G. W. Ni@B_{80}: A Single Molecular Magnetic Switch. *Appl. Phys. Lett.* **2009**, 95, 133115.

60. Liu, A. Y.; Zope, R. R.; Pederson, M. R. Structural and Bonding Properties of bcc-Based B_{80} Solids. *Phys. Rev. B* **2008**, 78, 155422.

61. Yan, Q. B.; Zheng, Q. R.; Su, G. Face-Centered-Cubic K_3B_{80} and Mg_3B_{80} Metals: Covalent and Ionic Bondings. *Phys. Rev. B* **2009**, 80, 104111.

62. Zhao, Y. F.; Lusk, M. T.; Dillon, A. C.; Heben, M. J.; Zhang, S. B. Boron-Based Organometallic Nanostructures: Hydrogen Storage Properties and Structure Stability. *Nano Lett*. **2008**, 8, 157.

63. Yan, Q. B.; Sheng, X. L.; Zheng, Q. R.; Zhang, L. Z.; Su, G. Family of Boron Fullerenes: General Constructing Schemes, Electron Counting Rule, and Ab Initio Calculations. *Phys. Rev. B* **2008**, 78, 201401.

64. Zhao, J.; Wang, L.; Li, F.; Chen, Z. B_{80} and Other Medium-Sized Boron Clusters: Core-Shell Structures, Not Hollow Cages. *J. Phys. Chem. A* **2010**, 114, 9969.

65. Szwacki, N. G.; Tymczak, C. J. The Symmetry of the Boron Buckyball and a Related Boron Nanotube. *Chem. Phys. Lett*. **2010**, 494, 80.

66. Wang, X.-Q. Structural and Electronic Stability of a Volleyball-Shaped B80 Fullerene. *Phys. Rev. B* **2010**, 82, 153409.

67. Quandt, A.; Boustani, I. Boron Nanotubes. *Chem. Phys. Chem*. **2005**, 6, 2001.

68. Özdogan, C.; Mukhopadhyay, S.; Hayami, W.; Gu¨ venc, Z. B.; Pandey, R.; Boustani, I. The Unusually Stable B_{100} Fullerene, Structural Transitions in Boron Nanostructures, and a Comparative Study of γ- and α-Boron and Sheets. *J. Phys. Chem. C* **2010**, 114, 4362.

69. Zope, R. R.; Baruah, T.; Lau, K. C.; Liu, A. Y.; Pederson, M. R.; Dunlap, B. I. Boron Fullerenes: From B80 to Hole Doped Boron Sheets. *Phys. Rev. B* **2009**, 79, 161403.

70. Ding, X.; Guo, J.; Feng, X.; Honsho, Y.; Guo, J.; Seki, S.; Maitarad, P.; Saeki, A.; Nagase, S.; Jiang, D. Synthesis of Metallophthalocyanine Covalent Organic Frameworks that Exhibit High Carrier Mobility and Photoconductivity. *Angew. Chem., Int. Ed.* **2011**, 50, 1289.

71. Spitler, E. L.; Dichtel, W. R. Lewis Acid-Catalysed Formation of Two-Dimensional Phthalocyanine Covalent Organic Frameworks. *Nat. Chem.* **2010**, 2, 672.

72. DMol3: Accelrys Material Studio 5.5; Accelrys Software, Inc.: San Diego, CA, **2011**.

73. Granatier, J.; Pitonak, M.; Hobza, P. Accuracy of Several Wave Function and Density Functional Theory Methods for Description of Noncovalent Interaction of Saturated and Unsaturated Hydrocarbon Dimers. *J. Chem. Theory Comput.* **2012**, 8, 2282.

74. Granatier, J.; Lazar, P.; Otyepka, M.; Hobza, P. The Nature of the Binding of Au, Ag, and Pd to Benzene, Coronene, and Graphene: from Benchmark CCSD(T) Calculations to Plane-Wave DFT Calculations. *J. Chem. Theory Comput.* **2011**, 7, 3743.

75. William, M. D.; Samarakoon, D. K.; Hess, D. W.; Wang, X.-Q. Tunable Bands in Biased Multilayer Epitaxial Graphene. *Nanoscale* **2012**, 4, 2962.

76. Hargrove, J.; Shashikala, H. B. M.; Guerrido, L.; Ravi, N.; Wang, X.-Q. Band Gap Opening in Methane Intercalated Graphene. *Nanoscale* **2012**, 4, 4443.

77. Gunasinghe, R. N.; Kah, C. B; Quarles, K.; Wang, X.-Q. Dispersion Correction in the Boron Buckyball and Nanotubes. *Appl. Phys. Lett.* **2011**, 98, 261906.

78. Ci, L.; Xu, Z.; Wang, L.; Gao, W.; Ding, F.; Kelly, K. F.; Yakobson, B. I.; Ajayan, P. M. Controlled nanocutting of grapheme. *Nano Res.* **2008**, 1, 116.

79. Samarakoon, D. K.; Gunasinghe, R. N.; Wang, X.-Q. A trigonal planar network in hydrogenated epitaxial graphene: a ferromagnetic semiconductor. *J. Mater. Chem. C* **2013**, 1, 2696.

80. Craig, N. C.; Chen, A.; Suh, K. H.; Klee, S.; Mellau, G. C.; Winnewisser, B. P.; Winnewisser, M. *J. Am. Chem. Soc.* **1997**, *119*, 4789.

81. Perdew, J.; Burke, K.; Ernzerhof, M. Generalized Gradient Approximation Made Simple. *Phys. Rev. Lett.* **1996**, 77, 3865.

82. Tkatchenko, A.; Scheffler, M. Accurate Molecular Van Der Waals Interactions from Ground-State Electron Density and Free-Atom Reference Data. *Phys. Rev. Lett*. **2009**, 102, 073005.

83. Marini, A.; Hogan, C.; Gruning, M.; Varsano, D. yambo: An *ab*-initio tool for excited state calculations*Comput. Phys. Commun*. **2009**, 180, 1392.

84. O'Hagan, D. Understanding organofluorine chemistry. An introduction to the C–F bond. *Chem. Soc. Rev.* **2008**, 37, 308.

85. Goodman, L.; Guand, H.; Pophristic, V. he gauche effect in 1,2-difluoroethane. Hyperconjugation, bend bonds, steric repulsion. *J. Phys. Chem. A* **2005**, 109, 1223.

86. Wang, X.; Zhi, L.; Mullen, K. Transparent, conductive graphene electrodes for dye-sensitized solar cells. *Nano Lett.* **2008**, 8, 323.

87. Zhou, J.; Wang, Q.; Sun, Q.; Jena, P. Stability and electronic structure of bilayer graphone. *Appl. Phys. Lett.* **2011**, 98, 063108.

88. Zhou, J.; Wang, Q.; Sun, Q.; Chen, X. S.; Kawazoe, Y.; Jena, P. Ferromagnetism in Semihydrogenated Graphene Sheet. *Nano Lett.* **2009**, 9, 3867.

89. Leenaerts, O.; Partoens, B.; Peeters, F. M. Hydrogenation of bilayer graphene and the formation of bilayer graphane from first principles. *Phys. Rev. B: Condens. Matter Mater. Phys.* **2009**, 80, 245422.

90. Wen, X.-D.; Hand, L.; Labet, V.; Yang, T.; Hoffmann, R.; Ashcroft, N. W.; Oganov, A. R.; Lyakhov, A. O. Graphane sheets and crystals under pressure. *Proc. Natl. Acad. Sci. U. S. A.* **2011**, 108, 6833.

91. Pisani, L.; Montanari, B.; Harrison, N. M. A defective graphene phase predicted to be a room temperature ferromagnetic semiconductor. *New J. Phys.* **2008**, 10, 033002.

92. McMurry, *J. Organic Chemistry, 2nd edn* **1987**, ISBN 0-53407968-7.

93. Gunasinghe, R. N.; Reuven, D. G.; Suggs, K.; Wang, X.-Q. Filled and empty orbital interactions in a planar covalent organic framework on grapheme. *J. Phys. Chem. Lett.* **2012**, 3, 3048.

94. Alabugin, I. V.; Gilmore, K. M.; Peterson, P. W. Hyperconjugation. *Comput. Mol. Biosci.* **2011**, 1, 109.

95. Komatsu, N.; Wang, F. A. A Comprehensive Review on Separation Methods and Techniques for Single-Walled Carbon Nanotubes. *Materials* **2010**, 3, 3818.

96. Tu, X.; Manohar, S.; Jagota, A.; Zheng, M. DNA sequence motifs for structure-specific recognition and separation of carbon nanotubes. *Nature* **2009**, 460, 250.

97. Ghosh, S.; Bachilo, S. M.; Weisman, R. B. Advanced sorting of single-walled carbon nanotubes by nonlinear density-gradient ultracentrifugation. *Nat. Nanotechnol.* **2010**, 5, 443.

98. Green, A. A.; Duch, M. C.; Hersam, M. C. Isolation of single-walled carbon nanotube enantiomers by density differentiation. *Nano Res.* **2009**, 2, 69.

99. Liu, H.; Nishide, D.; Tanaka, T.; Kataura, H. Large-scale single-chirality separation of single-wall carbon nanotubes by simple gel chromatography. *Nat. Commun.* **2011**, 2, 309.

100. Pan, X.; Li, L.-J.; Chan-Park, M. B. Diameter- and Metallicity-Selective Enrichment of Single-Walled Carbon Nanotubes Using Polymethacrylates with Pendant Aromatic Functional Groups. *Small* **2010**, 6, 1311.

101. Chen, F.; Wang, B.; Chen, Y.; Li, L. Toward the extraction of single species of single-walled carbon nanotubes using fluorine based polymer. *J. Nano Lett.* **2007**, 7, 3013.

102. Ozawa, H.; Ide, N.; Fujigaya, T.; Niidome, Y.; Nakashima, N. One-pot separation of highly enriched (6,5)-single-walled carbon nanotubes using a fluorene-based copolymer. *Chem. Lett.* **2011**, 40, 239.

103. Antaris, A. L.; Seo, J. W.; Green, A. A.; Hersam, M. C. Electronic Type Using Nonionic, Biocompatible Block Copolymers. *ACS Nano* **2010**, 4, 4725.

104. Wei, L.; Wang, B.; Goh, T. H.; Li, L. J.; Yang, Y.; Chan-Park, M. B.; Chen, Y. Selective enrichment of (6,5) and (8,3) single-walled carbon nanotubes via co-surfactant extraction from narrow (n,m) distribution samples. *J. Phys. Chem. B* **2008**, 112, 2771.

105. Chen, Y.; Xu, Y.; Wang, Q.; Gunasinghe, R. N.; Wang, X.-Q.; Pang, Y. Highly Selective Dispersion of Carbon Nanotubes by Using Poly(phenyleneethynylene)-Guided Supermolecular Assembly. *Small* **2012**, 9, 870.

106. Ogunro, O. O.; Wang, X.-Q. Charge transfer in the non-covalent functionalization of carbon nanotubes. *New J. Chem*. **2010**, 34, 1084.

107. Ogunro, O. O.; Wang, X. Q. Quantum Electronic Stability in Selective Enrichment of Carbon Nanotubes. *Nano Lett*. **2009**, 9, 1034.

108. Ju, S. Y.; Doll, J.; Sharma, I.; Papadimitrakopoulos, F. Nat. Selection of carbon nanotubes with specific chiralities using helical assemblies of flavin mononucleotide. *Nanotechnol*. **2008**, 3, 356.

109. Lu, J.; Lai, L.; Luo, G.; Zhou, J.; Qin, R.; Wang, D.; Wang, L.; Mei, W. N.; Li, G.; Gao, Z.; Nagase, S.; Meada, Y.; Akasaka, T.; Yu, D. Why semiconducting single-walled carbon nanotubes are separated from their metallic counterparts. *Small* **2007**, 3, 1566.

110. Chen, Y.; Xu, Y.; Perry, K.; Sokolov, A. P.; More, K.; Pang, Y. Achieving Diameter-Selective Separation of Single-Walled Carbon Nanotubes by Using Polymer Conformation-Confined Helical Cavity*ACS Macro Lett.* **2012**, 1, 701.

111. Odom, T. W.; Huang, J. L.; Kim, P.; Lieber, C. M. Atomic structure and electronic properties of single-walled carbon nanotubes. *Nature* **1998**, 391, 62.

112. Dresselhaus, M. S.; Dresselhaus, G.; Avouris, P.; *Springer Berlin* **2001**.

113. Ajayan, *P. M.* Nanotubes from Carbon. *Chem. Rev.* **1999**, 99, 1787.

114. Papadimitrakopoulos, F.; Ju, S.-Y. Purity rolled up in a tube. *Nature* **2007**, 450, 486.

115. Kim, S. N.; Luo, Z.; Papadimitrakopoulos, F. Diameter and metallicity dependent redox influences on the separation of single-wall carbon nanotubes. *Nano Lett.* **2005**, 5, 2500.

116. Zheng, M.; Semke, E. D. Enrichment of Single Chirality Carbon Nanotubes. *J. Am. Chem. Soc*. **2007**, 129, 6084.

117. Zheng, M.; Jagota, A.; Semke, E. D.; DNA-assisted dispersion and separation of carbon nanotubes. *Nature Mater*. **2003**, 2, 338.

118. Kim, S. N.; Kuang, Z.; Grote, J. G.; Farmer, B. L.; Naik, R. R. Enrichment of (6,5) single wall carbon nanotubes using genomic DNA. *Nano Lett*. **2008**, 8, 4415.

119. Nish, A.; Hwang, J.-Y.; Doig, J.; Nicholas, R. J. Highly selective dispersion of single-walled carbon nanotubes using aromatic polymers. *Nat. Nanotechnol*. **2007**, 2, 640.

120. Yi, W.; Malkovskiy, A.; Chu, Q.; Sokolov, A. P.; Colon, M. L.; Meador, M.; Pang, Y. Wrapping of single-walled carbon nanotubes by a π-conjugated polymer: The role of polymer conformation-controlled size selectivity. *J. Phys. Chem. B* **2008**, 112, 12263.

121. Chen, Y.; Malkovskiy, A.; Wang, X.-Q.; Colon, M. L.; Sokolov, A. P.; Perry, K.; More, K.; Pang, Y. Achieving Diameterselective Separation of Single-walled Carbon Nanotubes by Using Polymer-Conformation-confined Helical Cavity. *ACS Macro Lett*. **2012**, 1, 246.

122. Keogh, S. M.; Hedderman, T. G.; Lynch, P.; Farrell G. F.; Byrne, H. J. Bundling and diameter selectivity in HiPco SWNTs poly(p-phenylene vinylene-co-2,5-dioctyloxy-m-phenylene vinylene) composites. *J. Phys. Chem. B* **2006**, 10, 19369.

123. Keogh, S. M.; Hedderman, T. G.; Farrell, G.; Byrne, H. J. *J. Phys. Chem. B* Spectroscopic Analysis of Single-Walled Carbon Nanotubes and Semiconjugated Polymer Composites. **2004**, 108, 6233.

124. Pang, Y.; Li, J.; Hu, B.; Karasz, F. E. *Macromolecules* **1999**, 32, 3496.

125. The rotational barrier around a carbon-carbon triple bond is calculated to be ~0 .64 kcal/mol. See Saebo, S.; Almolof, J.; Boggs, J. E.; Stark, J. G. *J. Mol. Struct. (THEOCHEM)* **1989**, 200, 361.

126. Chen, J.; Liu, H.; Weimer, W. A.; Halls, M. D.; Waldeck, D. H.; Walker, G. C. Noncovalent engineering of carbon nanotube surfaces by rigid, functional conjugated polymers. *J. Am. Chem. Soc.* **2002**, 124, 9034.

127. Bargen, C. D. V.; MacDermaid, C. M.; Lee, O.-S.; Deria, P.; Therien M. J.; Saven, J. G. *J. Phys. Chem. B* **2013**, 117, 12953.

128. Furmanchuk, A.; Leszczynski, J.; Tretiak, S.; Kilina, S. V. *J. Phys. Chem. C* **2012**, 116, 6831.

129. Bilalis, P.; Katsigiannopoulos, D.; Avgeropoulos, A.; Sakellariou, G. Non-covalent functionalization of carbon nanotubes with polymers. *RSC Adv*. **2014**, 4, 2911.

130. Ponnamma, D.; Sadasivuni, K. K.; Grohens, Y.; Guo, Q.; Thomas, S. Carbon nanotube based elastomer composites – an approach towards multifunctional materials. *J. Mater. Chem. C* **2014**, 2, 8446.

131. Soleyman, R.; Adeli, M. Impact of dendritic polymers on nanomaterials. *Polym. Chem*. **2015**, 6, 10.

132. Hohenberg, P.; Kohn, W. Inhomogeneous Electron Gas. *Phys. Rev*. **1964**, 136, 864.

133. Gaussian 03, Revision C.02, Frisch, M. J.; Trucks, G. W. et al. Gaussian, Inc., Wallingford CT, **2004**.

134. Kleis, J.; Hyldgaard, P.; Schröder, E. Comput. *Mater. Sci*. **2005**, 33, 192.

135. Kleis, J.; ESchröder, E. van der Waals interaction of simple, parallel polymers. *J.Chem. Phys*. **2005**, 122, 164902.

136. Becke, A. D. Density-functional thermochemistry. III. The role of exact exchange. *J. Chem. Phys.* **1993**, 98, 5648.

137. Lee, C.; Yang, W.; Parr, R.G. Development of the Colle-Salvetti Correlation Energy Formula into a Functional of the Electron Density. *Phys. Rev. B* **1988**, 37, 785.

138. Møller, C.; Plesset, M. S. Note on an Approximation Treatment for Many-Electron Systems. *Phys. Rev*. **1943**, 46, 618.

139. Payne, M. C.; Teter, M. P.; Allan, D. C.; Arias, T.A.; Joannopoulos, T. D. Iterative minimization techniques for ab initio total-energy calculations: molecular dynamics and conjugate gradients. *Rev. Mod. Phys*. **1992**, 64, 1045.

140. Derosa, P. A. Accelerating molecular dynamic simulation on graphics processing units. *J. Comput. Chem*. **2009**, 30, 1220.

141. Denis, P. A.; Yanney, M. Porphyrins bearing corannulene pincers: outstanding fullerene receptors. *New J. Chem*. **2016**, 40, 202.

142. Tersof, J. New empirical approach for the structure and energy of covalent systems. *Phys. Rev. B* **1988**, 37, 6991.

143. Headen, T. F.; Howard, C. A.; Skipper, N. T.; Wilkinson, M. A.; Bowron, D. T.; Soper, A. K. Structure of pi-pi interactions in aromatic liquids. *J. Am. Chem. Soc*. **2010**, 132, 5735.

144. Grimme, S. Do special noncovalent pi-pi stacking interactions really exist? *Angew. Chem. Int. Ed*. **2008**, 47, 3430.

145. Sinnokrot, M. O.; Sherill, C. D. High-Accuracy Quantum Mechanical Studies of π-π Interactions in Benzene Dimers. *J. Phys. Chem. A* **2006**, 110, 10656.

146. Hobza, P.; Selzle, H. L.; Schlag, E. W. Potential energy surface of the benzene dimer: ab initio theoretical study. *J. Am. Chem. Soc.* **1994**, 116, 3500.

147. Tsuzuki, S.; Uchimaru, T.; Mikami, M.; Tanabe, K. Basis set effects on the calculated bonding energies of neutral benzene dimers: importance of diffuse polarization function. *Chem. Phys. Lett*. **1996**, 252, 206.

148. Jafe, R. L.; Smith, G. D. A quantum chemistry study of benzene dimer. *J. Chem. Phys*. **1996**, 105, 2780.

149. Chipot, C.; Jafe, R.; Maigret, B.; Pearlman, D. A.; Kollman, P. A. Benzene Dimer: A Good Model for π−π Interactions in Proteins? A Comparison between the Benzene and the Toluene Dimers in the Gas Phase and in an Aqueous Solution. *J. Am. Chem. Soc.* **1996**, 118, 11217.

150. Hobza, P.; Selzle, H. L.; Schlag, E. W. Potential energy surface for the benzene dimer. Results of ab initio CCSD(T) calculations show two nearly isoenergetic structures: T-shaped and parallel-displaced. *J. Phys. Chem*. **1996**, 100, 18790.

151. Bernstein, E. R.; Sun, S. J. Aromatic van der Waals Clusters: Structure and Nonrigidity. *J. Phys. Chem*. **1996**, 100, 13348.

152. Yi, W.; Malkovskiy, A.; Xu, Y.; Wang, X.; Sokolov, A. P.; Lebron-Colon, M.; Meador, M. A.; Pang, Y. Selection of Single-Walled Carbon Nanotube with Narrow Diameter Distribution by Using a PPE–PPV Copolymer. *Polymer* **2010**, 51, 475481.

153. Li, H.; Shao, N.; Shang, B.; Yuan, L.-F.; Yang, J. L.; Zeng, X. C. Icosahedral B_{12}-Containing Core-Shell Structures of B_{80}. *Chem. Commun*. **2010**, 46, 3878.

154. Ufimtsev, I. S.; Martinez, T. J. Quantum Chemistry on Graphical Processing Units. 3. Analytical Energy Gradients and First Principles Molecular Dynamics. *J. Chem. Theory Comput.* **2009,** 5, 2619.

155. Baruah, T.; Pederson, M. R.; Zope, R. R. Vibrational Stability and Electronic Structure of a B_{80} Fullerene. *Phys. Rev. B* **2008**, 78, 045408.

156. Zhang, B. L.; Wang, C. Z.; Ho, K. M.; Xu, C. H.; Chan, C. T. The Geometry of Large Fullerene Cages: C_{72} to C_{102}. *J. Chem. Phys*. **1993**, 98, 3095.

157. Sadrzadeh, A.; Pupysheva, O. V.; Singh, A. K.; Yakobson, B. I. The Boron Buckyball and Its Precursors: An Electronic Structure Study. *J. Phys. Chem. A* **2008**, 112, 13679.

158. Ceulemans, A.; Muya, J. T.; Gopakumar, G.; Nguyen, M. T. Chemical Bonding in the Boron Buckyball. *Chem. Phys. Lett*. **2008**, 461, 226.

159. Zope, R.R.; and Baruah, T. Snub boron nanostructures: Chiral fullerenes, nanotubes and planar sheet. *Chem. Phys. Lett*. **2011**, 501,193.

160. Pochet, P.; Genovese, L.; Caliste, D.; Rousseau, I.; Goedecker, S.; Deutsch, T. First-Principles Prediction of Stable SiC Cage Structures and Their Synthesis Pathways. *Phys. Rev. B* **2010**, 82, 035431.

161. Singh, A.K.; Sadrzadeh, A.; Yakobson, B.I. Probing Properties of Boron a-Tubes by *ab*-initio Calculations. *Nano Lett*. **2008**, 8, 1314.

162. Ciuparu, D.; Klie, R.F.; Zhu, Y.; Pfefferle, L. B Synthesis of Pure Boron Single-Wall Nanotubes. *J. Phys. Chem*. **2004**, 108, 3967.

163. Muya, J.T.; Gopakumar, G.; M. T. Nguyen, M.T.; Ceulemans, A. The Leapfrog Principle for Boron Fullerenes: A Theoretical Study of Structure and Stability of B_{112}. *Phys. Chem. Chem. Phys*. **2011**, 13, 7524.

164. De, S.; Willand, A.; Amsler, M.; Pochet, P.; Genovese, L.; Goedecker, S. Energy Landscape of Fullerene Materials: A Comparison of Boron to Boron Nitride and Carbon. *Phys. Rev. Lett*. **2011**, 106, 225502.

165. Szwacki,N.G.; Weber, V. and Tymczak, C.J. Aromatic Borozene. *Nanoscale Res. Lett.* **2009**, 4, 1085.

166. Quarles, K.; Gunasinghe, R.N.; Kah, C.B.; Musin, R.N.; Wang, X.-Q. Filled Pentagons and Electron Counting Rule for Boron Fullerenes. *J. Chem. Theory Comput.* **2011**, 7, 2017.

167. Tian, J.; Xu, Z.; Shen, C.; Liu, F.; Xu, N.; Gao, H.-J. One-Dimensional Boron Nanostructures: Prediction, Synthesis, Characterizations, and Applications. *Nanoscale* **2010**, 2, 1375.

168. Hsing, C.R.; Wei, C.M.; Drummond, N.D.; Needs, R.J. Quantum Monte Carlo Studies of Covalent and Metallic Clusters: Accuracy of Density Functional Approximations. *Phys. Rev. B* **2009**, 79, 245401.